Damage Tolerance of High-Performance Composites

Vom Promotionsausschuss der
Technischen Universität Hamburg

zur Erlangung des akademischen Grades

Doktor-Ingenieur (Dr.-Ing.)

genehmigte Dissertation

von
Johann Körbelin

aus Hamburg

2022

Vorsitzender des Prüfungsausschusses:	Prof. Dr.-Ing. habil. Stefan Heinrich (Technische Universität Hamburg)
Gutachter:	Prof. Dr.-Ing. habil. Bodo Fiedler (Technische Universität Hamburg) Prof. Dr.-Ing. Peter Horst (Technische Universität Braunschweig)
Tag der mündlichen Prüfung:	28.01.2022

Technisch-Wissenschaftliche Schriftenreihe

Herausgeber:
Prof. Dr.-Ing. habil. Bodo Fiedler

Anschrift:
Technische Universität Hamburg
Institut für Kunststoffe und Verbundwerkstoffe
Denickestraße 15
21073 Hamburg

Band 41:
Damage Tolerance of High-Performance Composites
DOI: https://doi.org/10.15480/882.4276

Johann Körbelin
https://orcid.org/0000-0003-3584-6471

1. Auflage
Hamburg 2022

ISSN 2625-6029

Bibliographische Information der Deutschen Nationalbibliothek: Die deutsche Nationalbibliothek verzeichnet diese Publikation in der Deutschen Nationalbibliothek; detaillierte Informationen sind im Internet über dnb.de abrufbar.

Acknowledgments

I would primarily like to thank Prof. Dr.-Ing. habil. Bodo Fiedler for his trust, the numerous discussions, advice and the working atmosphere, through which I was able to learn and develop a lot.

Sincere thanks go to Prof. Dr.-Ing. Peter Horst for acting as the second examiner in my doctoral thesis and to Prof. Dr.-Ing. habil. Stefan Heinrich for taking over the chairmanship of the examination board.

I would also like to thank my colleagues at the Institute of Polymer and Composites for their support, friendship and long, insightful discussions. My special thanks go to Benedikt Kötter, Hauke Voormann, Sergej Harder, Christina Buggisch, Dennis Gibhardt, Sven Drücker, Valea Wisniewski and Hubert Beisch. I would also like to thank Dr.-Ing. Hans Wittich and Inga Schmidt, who always had time for me. My thanks go to the students I supervised, whose work contributed to the research project's success.

I thank my parents, Birgit and Carsten, for their support and for being role models. Finally, I would especially like to thank Marie Liebetrau for always being there and supporting me.

Abstract

High-performance composite laminates are structural materials that combine low density with high stiffness and strength. However, damage tolerance considerations constrain the design space of load-bearing composites, as some level of damage must be assumed to exist in the composite structure. Stress concentrations and damage like delaminations reduce the residual strength of composites significantly [1–3]. This results in high safety factors to be taken into account.

The multi-scale nature of composites results in the occurrence of different failure modes and a complex failure behaviour where matrix failure at the micro-level affects the failure process at all higher observation levels. Consequently, the occurring matrix damage has a decisive influence on the damage tolerance. The research hypothesis of this thesis is therefore:

Understanding and adapting the matrix's damage behaviour is fundamental to improve the damage tolerance of high-performance composites.

Two different ways to adapt the matrix damage behaviour of carbon-fibre reinforced plastics (CFRPs) are investigated: the matrix modification with few-layer graphene (FLG) and the adaption of bio-inspired layups. To further understand the influence of the matrix damage behaviour on the composite, the influence of the ambient temperature on the damage tolerance is another focus of this thesis. To adapt the matrix's damage behaviour, CFRPs with a FLG modified matrix with ply thicknesses varying from ultra-thin-ply (28 µm, 30 g/m^2) to thick-ply (220 µm, 240 g/m^2) were investigated. The FLG modification introduces additional damage modes into the matrix and significantly increases the composite's mode I and mode II interlaminar energy release rates (ERR). The modification increases the damage initiation stress of the notched tensile specimen, the allowed design space and damage tolerance. For ultra-thin-ply laminates, the notched strength is increased due to crack blunting because the FLGs initiate

distributed damage on the micro-scale in highly stressed areas. The overall matrix damage resulting from low-velocity impact (LVI) decreases with the FLG modification for all ply thicknesses, but only the thick-ply laminate's residual compressive strength increases.

As a second approach to adapt the matrix damage, bio-inspired laminates with a helicoidal layup with a pitch angle of 2.07° were realised. Due to the small angle between the plies, the laminates suppress the formation of delamination damage and only exhibit subcritical matrix cracking before final failure. As a result, the compressive residual strength after LVI is significantly increased compared with 45°-quasi-isotropic (QI) layup, despite a lower proportion of 0° fibres in the load direction. Due to the low portion of load oriented fibres, the unnotched tensile strength is lower compared to the 45°-QI layups. However, the formation of helicoidal matrix damage leads to crack blunting and as a result, almost no notch sensitivity occurs, while similar notched strengths as 45°-QI layups are achieved, despite the low portion of load oriented fibres.

Additionally, this thesis investigated the influence of temperature on LVI and the residual strength to further understand the influencing factors of damage tolerance. Because the matrix's mechanical performance decreases with increasing environmental temperature, the composite's damage behaviour is temperature-sensitive. LVIs with impaction energies between 8 and 25 J and temperature ranging from −20 to 80 °C were investigated. A shift in temperature leads to a substantial change in damage behaviour. With increasing temperature, the delamination area decreases and fibre-failure occurs on the impacted side, which reduces the residual tensile strength considerably. The compressive residual strength was determined at 20 and 80 °C. The results point out that an elevated temperature during compressive loading has a more significant influence than the impact energy. To further understand the influence of temperature on the impact damage and the residual strength, temperature-dependent material properties were determined and implemented into a continuum damage model (CDM) to describe CFRPs' progressive failure under temperature influence. Simulations validated that the material model could both predict the damage resulting from LVI at different temperatures and impact energies and the residual compressive strength in consecutive CAI simulations at various temperatures. The simulation results show that the reduction in delamination size is caused by a change in intralaminar damage and overall structural behaviour due to the matrix's

decreasing properties with increasing temperature rather than an increase in interlaminar ERR.

The approaches used in the thesis to adapt the matrix damage have shown that they are suitable for increasing the damage tolerance of high-performance fibre composites. Together with a deeper understanding of the influence of the ambient temperature on the occurring matrix damage, the work contributes to the realisation of safer composites.

Contents

List of Abbreviations

AE	Acoustic emission
BVID	Barely visible impact damage
CAI	Compression after impact
CC	Compliance calibration
CDM	Continuum damage mechanics
CFRP	Carbon-fibre reinforced polymer
CNP	Carbon nanoparticle
CT	Computer tomography
DCB	Double cantilever beam
DGD	Deformation gradient decomposition
DIC	Digital image correlation
DMA	Dynamic mechanical analysis
ENF	End-notched flexure
ERR	Energy release rate
FAW	Fibre areal weight
FEM	Finite element method
FLG	Few-layer graphene
FML	Fibre metal laminate
FPF	First ply failure
FRP	Fibre-reinforced polymer
FVC	Fibre volume content
GFRP	Glass-fibre reinforced polymer
ILSS	Interlaminar shear strength
LVI	Low-velocity impact
MWCNT	Muli-wall-carbon nanotube
NTPT	North Thin Ply Technology
OHC	Open-hole compression
OHT	Open-hole tension
PTFE	Polytetrafluoroethylene
QI	Quasi-isotropic
RMSE	Root-mean-square error

SEM	Scanning electron microscope
SENB	Single-end-notch bending
SWCNT	Single-wall carbon nanotube
TAI	Tension after impact
UD	Unidirectional
UNT	Unnotched tension
VARTM	Vacuum assisted resin transfer molding

1. Introduction

High-performance fibre-reinforced composite laminates are structural materials that combine a low density with high stiffness and strength and find application in aerospace, industrial and civil structures and sports goods. High safety and reliability requirements for structural parts necessitate detailed knowledge about the damage tolerance to design safe, reliable and lightweight structures. Damage tolerance is the property of a structure or material to resist defects, cracks or other damage for a period of time sufficient to enable their detection [1, 4]. In a more general way, damage tolerance is the ability to predict the material's strength in the broadest sense under consideration of, e.g. effects of the environment, temperature, stress state and damage state [1, 5]. Figure 1.1 summarises factors influencing the damage tolerance of high-performance composites and divides them into internal factors that define the material properties and external factors containing external loads and structural design [6].

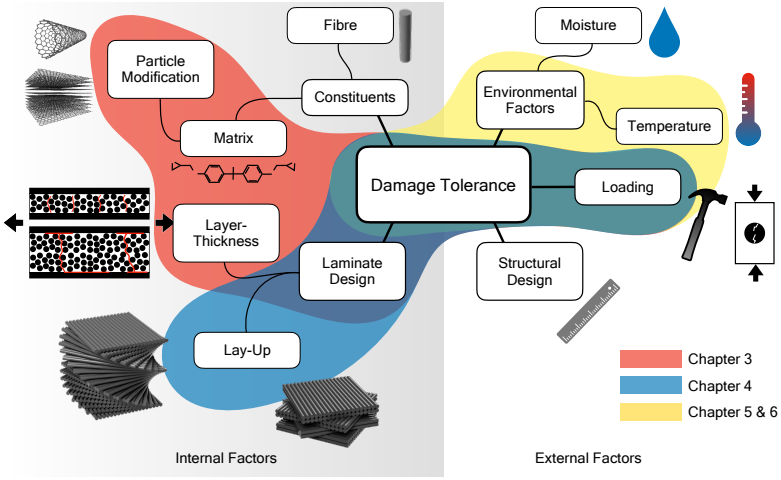

Figure 1.1.: Factors influencing the damage tolerance of high-performance composites

The consideration of damage tolerance is crucial for a safe operation of composite structures because unpredictable failures over the lifetime of structures outnumber the predictable failures by far [4].

The material considered in this thesis are carbon-fibre reinforced polymers (CFRPs). Thus, the load-bearing work in laminates is done by the carbon fibres with high stiffness and strength, while the epoxy matrix functions in keeping the fibres together and transferring the loads between the fibres. This thesis focuses on high-performance composites with unidirectional (UD) plies, i.e. the fibres are long and straight, and inside one composite ply, all fibres orient in the same direction. A laminate is made out of stacking these plies in different orientations. This description highlights the multi-scale nature of the material, resulting in a complex failure behaviour. Different failure modes occur, and matrix failure at the micro-level influences the failure process at all higher observation levels [7–11].

Figure 1.2 shows the mesoscale failure modes for a laminate with a circular hole under tension. Matrix failure can be described as matrix cracking or ply splitting when the crack runs through the ply's thickness or as delamination when it is located between the plies. Failure of fibres occurs as a fracture in tension or as kinking under compression. The occurring failure modes are not isolated but interact and influence each other. As numerous influencing factors determine the damage sequence and the occurring failure modes, no generally applicable failure sequence exists for an arbitrary composite [7–13]. A different ply thickness, specimen size or layup can lead to a different failure process and consequently, ultimate strength. In laminates with sufficiently thick plies, delamination is the predominant and critical failure mechanism. In tensile tests, matrix cracks initiate first. Subsequently, delamination is initiated by matrix cracks or at free edges and easily propagates through the interply interface. Delamination spreads to the neighbouring interfaces by transverse and off-axis matrix cracks, finally isolating the 0° plies, leading to complete gauge section delamination [7, 14, 15]. Stress concentrations at holes, manufacturing flaws, damage or design mistakes lead to premature initiation of damage [16]. As the investigated composites consist of brittle constituents, plastic yielding cannot blunt stress concentration. Only occurring damage can relieve stress concentrations. Therefore stress concentrations lead to a significant reduction of the ultimate strength in composites, leading to high-security factors needed in structural design. The stress concen-

trations can have a multitude of reasons, e.g. design features, manufacturing flaws or in service damage (see Figure 1.1).

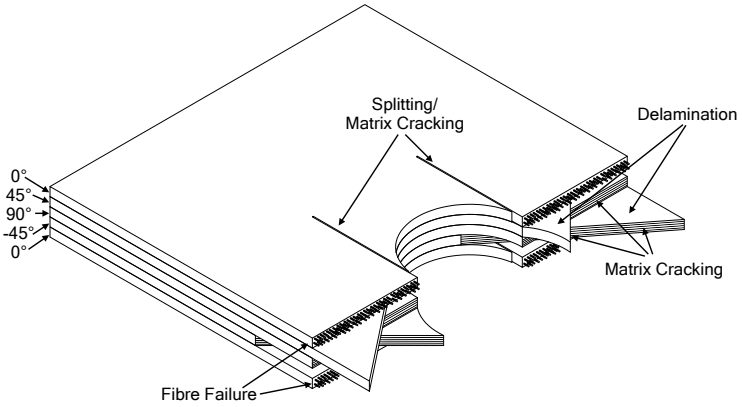

Figure 1.2.: Schematic representation of the damage modes occurring in a composite laminate with a circular hole under tensile load

The damages occurring in-service are significant for damage tolerance consideration, as composites are susceptible to damage caused by contact with foreign objects, like low-velocity impacts (LVI). Due to composites' layered structure and low out-of-plane strength, even supposedly low impact loads lead to local damage, which is hard to detect visually and is therefore referred to as barely visible impact damage (BVID). BVID usually leads to severe matrix cracking and delamination. These matrix damages reduce the residual strength considerably. Because of this damage behaviour, composite structures in safety-critical applications are subjected to high requirements on damage tolerance, as some level of damage must be assumed to exist in the composite structure [1–3].

As summarised in Figure 1.1, the determination of the damage tolerance is problematic, as it depends on many, partly unknown factors. The internal factors determine the material, which includes all the constituents and the laminate design. On the other side, the external factors are, e.g. the environmental factors, the loading and the structural design. However, the internal and external factors

are highly dependent on each other. The composite's complex failure behaviour, the possibility of existing flaws and the uncertainty of the occurring loads on the laminate lead to the fact that the damage tolerance's determination is complex as not all influencing factors can be known [4]. This results in the need for high safety factors and extensive testing on coupon and component level to determine or achieving the necessary damage tolerance [17].

1.1. Aims and Scope

Following the introduction, it becomes clear that a broad knowledge of the influencing factors and measures to increase the damage tolerance is crucial to utilise high-performance composite's lightweight potential while improving composite structures' safety. The occurring matrix damage governs the failure process to a large extent and the damage tolerance of composites. The general overarching research hypothesis on which the content of this thesis is based is as follows:

Understanding and adapting the matrix's damage behaviour is fundamental to improve the damage tolerance of high-performance composites.

The research hypothesis divides the thesis into two main segments. The first segment investigates how adapting the occurring matrix damage can improve the damage tolerance. Chapter "Nanoparticle Modified CFRPs" (Chapter 3) explores how the ply thickness and matrix modification with carbon nanoparticles influence the occurring matrix damage and potentially increases damage tolerance (see Figure 1.1 highlighted in red). Chapter "Bio-Inspired Helicoidal Laminates" (Chapter 4) utilises new layup designs to adapt to the occurring matrix damage to increase the damage tolerance (see Figure 1.1 highlighted in blue). The second segment's Chapters "Damage Tolerance under Temperature Influence" (Chapter 5) and "Simulation of Failure at Elevated Temperatures" (Chapter 6) investigate how temperature as an external factor influences the matrix behaviour and the composite's damage tolerance (see Figure 1.1 highlighted in yellow). The different approaches are introduced below and working hypotheses are derived for the different sections.

One approach to influence matrix damage is the reduction of ply thickness, investigated in Chapter 3. In recent years so-called "thin-ply" laminates have

gained interest, characterised by a ply thickness of less than 60 µm. UD tensile quasi-static tests on unnotched multi-directional thin-ply laminates revealed that matrix failure initiation is delayed nearly up to ultimate failure, increasing the strength considerably. As a result, the dominant failure mode in thin-ply laminates is fibre failure [13, 18]. However, the suppression of matrix damage leads to a significant reduction in notched laminates' strength as no crack blunting through matrix damage occurs. The suppression of matrix damage also influences the damage resulting from LVI, which results in large projected delamination areas due to the formation of a single or a few extensive delaminations instead of numerous smaller ones in laminates with thicker plies [18, 19]. However, the compression after impact (CAI) strength of thin-ply composites increases compared to thick-ply laminates, as the fewer larger delaminations divide the laminate into stronger sub-laminates.

Another promising approach to influence the damage behaviour of CFRPs is a matrix modification with carbon nanoparticles (CNPs). These nano fillers offer outstanding stiffness, strength and surface area [20, 21]. These properties lead to significant fracture toughness increments when added to epoxy due to additional damage modes at the nanoparticle [20, 21]. Some studies reveal that CNPs also increase composites' interlaminar fracture toughness. Thus, matrix modification with CNPs can significantly influence the CFRPs' failure behaviour by changing the matrix properties and potentially reducing some drawbacks of high-performance composites, namely large delamination areas and notch sensitivity in thick- and thin-ply composites, by offering stress-relieving damage mechanisms to highly stressed regions of thin-ply laminates or suppressing early matrix damage and subsequently delamination failure in thick-ply laminates. The derived research hypothesis for chapter 3 reads:

The addition of CNPs into the matrix introduces additional energy-consuming damage mechanisms into the composite and leads to crack blunting at stress concentrations due to the formation of dispersed local damage. The effect of the CNP modification depends on the ply thickness, as it controls the stress state in the laminate.

Chapter 4 "Bio-Inspired Helicoidal Laminates" investigates how new layup designs utilising the design space enabled by thin-ply composites can improve the damage tolerance. In biology, extreme damage-tolerant properties have been

identified for highly stressed body parts of some crustaceans animals [22]. Researchers showed that the damage tolerant body parts are made up of laminated chitin fibre composite structure with a minimal fibre difference or pitch angle between UD-plies, resulting in a helicoidal shaped layup. The structure can dissipate the impact energy by propagating helicoidal micro-cracks, thus preventing catastrophic failure despite high impact velocities [23]. The high number of degrees of freedom of thin-ply layups makes it possible to recreate these layered structures found in nature with CFRP composites. The low fibre angle between plies results in low stiffness differences between the individual plies and low interlaminar stresses, allowing helicoidal matrix cracking but preventing delamination. The research hypothesis derived for this chapter is:

The composite's layup controls the occurring matrix damage modes. Thin-ply, bio-inspired helicoidal layups enable delamination-free composites.

Chapter 5 and 6 deal with the second part of the research hypothesis to deepen the understanding of how matrix behaviour influences damage tolerance. A comprehensive understanding of the damage caused by LVI and the resulting residual strength is essential to design safe, lightweight and damage-tolerant structures. Consequently, LVI damage and the resulting residual strength has been a research focus for decades [24, 25]. Nevertheless, there are still open questions, especially concerning the impact of environmental factors. The epoxy's mechanical properties are temperature sensitive and decline with increasing temperature. As a result, most properties of the composite are also temperature-dependent [26, 27]. The temperature influences the elastic and damage behaviour of CFRPs [27–31]. Consequently, a straightforward answer on how temperature influences the damage process cannot be given since different effects like matrix softening, stress relaxation and the reduction of thermal stresses combine to influence the failure process. Impact loading subjects the composite to complex loads, e. g. crushing load of the impactor and compressive, tensile and strong interlaminar shear loads due to bending. As a result it is challenging to estimate how the failure behaviour is affected at various temperatures. Chapter 5 and 6 are investigating the influence of temperature on the damage tolerance. The derived hypothesis for these chapters is:

The matrix's mechanical performance decreases with increasing environmental temperature and negatively influences the damage tolerance.

Chapter 5 “Damage Tolerance under Temperature Influence” experimentally investigates the influence of temperature on the damage resulting from LVI and the resulting residual tensile and compressive strength. To fully exploit the potential of CFRPs, predicting the occurring failure mode and the resulting strengths is viable. As displayed in Figure 1.1, the number of influences on the damage tolerance are plentiful, even if the constituents and ply thickness are kept constant. The impact tolerance needs to be reevaluated when the surrounding conditions, layup or structural design change. This results in the need for expensive and time-consuming test campaigns not only on the coupon level and conservative assumptions for designing components and structures. Therefore, methods for reliable computational modelling of damage tolerance are needed to evaluate composite structures' damage tolerance. In Chapter 6 “Simulation of Failure at Elevated Temperatures” a continuum damage model (CDM), based on the material model CompDam [32], for the simulation of initiation and propagation of damage under temperature influence with the finite element method (FEM) is proposed. The model is then utilised in LVI and CAI simulations and compared to experimental results obtained in Chapter 5.

1.2. Thesis Outline

Chapter 2 introduces the experimental methods and manufacturing processes used throughout the thesis. Nevertheless, in some cases, additional methods are explained in the respective chapter.

As described above, three different working hypotheses are considered in this thesis, examining different damage tolerance aspects. This work's structure divides the three working hypotheses into four chapters. Chapters 3, 4, 5 and 6 have dedicated state of the art, materials, results and discussion and conclusion sections to increase the readability.

2. Manufacturing Processes and Experimental Methods

This chapter presents the experimental methods and manufacturing processes used. As different materials are used throughout the thesis, the materials are presented in the respective chapter to improve the orientation.

2.1. Manufacturing Methods

2.1.1. Epoxy Nanocomposites

CNP epoxy nanocomposites were manufactured to determine the impact of CNP type and filler content on epoxy fracture toughness. The resin plates were manufactured through a vacuum-assisted resin transfer moulding (VARTM) process. As the prepreg utilises hot-melt resin, which offers a high viscosity at room temperature, the VARTM process is conducted at 70 °C temperature in a UF55plus oven (Memmert, Germany). Following the infusion process, a pressure of 3 bar was applied, and the resin cured according to the manufacturer's temperature specifications.
For the CNP modified samples, as a first step, a 1 weight % (wt. %) CNP concentration master-batch was manufactured. The CNPs were incorporated into the curing agent through a seven-step three-roll milling process using an 80E Plus three-roll mill (EXAKT Advanced Technologies, Germany). A detailed description of the process can be found in [33]. The masterbatch was then mixed with the resin and additional hardener in a DAC 150.1 speed mixer (Synergy Devices Ltd, UK) to obtain the desired CNP concentration, followed by plate manufacturing using VARTM, similar to that of a neat resin. Samples were extracted from the resin plates using a Euromod 35 mill (isel Germany AG, Germany). The dimension of the specimens are given in the description of the respective test.

2.1.2. CFRP Specimen Preparation

Prior to the samples' lamination, a TL1625 CNC cutter (Aristo, Germany) cut the prepreg plies into the desired shape. During lamination, flat moulds with an alignment jig were used to ensure precise placement. A vacuum press debulked the laminate after every fourth layer. After finishing lamination, the laminate was cured in an autoclave (Scholz, Germany) according to the manufacturer's specifications. Every manufactured plate underwent quality control using ultrasonic C-scans and microscopy to detect manufacturing deviations. Table 2.2 and Table 2.3 summarise the tests and the specimen dimensions utilised in this thesis. If specified by the according test standard, glass-fibre reinforced polymer (GFRP) tabs to support the load introduction were bonded to the specimen. Depending on the test temperature, either Endfest 300 (UHU, Germany) for room temperature tests or DP760 (3M, USA) for elevated temperature tests were used. The specimens were cut into shape using a diamond-coated cutting wheel with a Brilliant 265 (ATM, Germany) or a F45 saw (Altendorf, Germany). Afterwards, the edges were polished up to 2500 grids. If the specimens required additional features like holes, they were milled using a Euromod 35 (isel Germany AG, Germany) mill. For the fabrication of the specimens used to evaluate the interlaminar behaviour, a 10 µm thick polytetrafluoroethylene (PTFE) film FP301100 (Goodfellow, USA) was placed in the mid-plane of the laminate during the lamination process. All specimens were dried and stored in a controlled climate before testing.

2.1.3. Quality Assurance and Damage Assesment

Ultrasonic C-Scan

Ultrasonic C-scans using a USPC 3040 DAC (Dr. Hillger NDT Germany) system to detect flaws and damage in the specimen were performed. The system has a resolution of 20 MHz and a maximum amplification of 106 dB in 0.5 dB steps. The tests utilised water as a coupling medium between the sample and a 6 MHz probe (Karl Deutsch, Germany). The ultrasound wave's speed in the specimen was calibrated by measuring the sample thickness and adjusting the velocity until the measured thicknesses matched.

To determine the projected delamination area from the C-scan, the back wall echo data was used. The image was converted into a binary picture using a

threshold, which was constant for all scans. The area was then calculated by inverting the binary picture and adding up the area's black pixels.

Micro-Sections

Micro-sections are a common way for evaluating the micro-structure of fractured and unfractured specimens. Preparation of the fractured specimen took an additional step before embedding the sample for polishing. In this step, the fractured specimen was vacuum-infused with coloured low viscosity RIMR 135/RIMH 134 (Hexion, Germany) epoxy resin and then cut at the desired position using a Brilliant 220 (ATM, Germany) circular saw with a diamond-coated blade. For polishing, the sample was embedded into KEM 15 compound (ATM, Germany). After that, the surface was polished with diamond suspension with a grain size as low as 1 μm using a Saphir 550 automatic polishing table (ATM, Germany). A microscope captured the polished micro-graph's image afterwards.

Light Microscopy

A BX51 microscope (Olympus, Japan) in bright-field mode was used to investigate the fracture surface of the epoxy nanocomposites. To investigate the micro-sections of CFRP, a VHX-6500 microscope (Keyence, Japan) was used. A G4 microscope (Bruker Alicona, Austria) was used for surface scans of the specimens' permanent deformations.

Fibre Volume Content

A wet chemical process, following DIN EN 2564 [34], determined the fibre mass content of the CFRP specimen. In this process sulphuric acid removes the epoxy matrix. Using the matrix's and fibres' densities, the fibre volume content (FVC) is determined. A three-point determination per tested specimen ensures a non-locally biased result. The Central Laboratory of Chemical Analysis of the Hamburg University of Technology (TUHH) carried out the analysis.

Digital Image Correlation

Digital image correlation (DIC) was used to determine the transient 3-dimensional deformation of a specimen surface during mechanical testing. An Aramis 4M

(GOM, Germany) system was used in a stereoscopic setup. A random, high-contrast speckle pattern was applied using spray paint to the specimen. The three-dimensional displacement field was derived from the stereo and transient correlation of the speckle pattern.

Acoustic Emission

An acoustic emission (AE) analysis system was performed during specific mechanical tests to determine the damage of CFRP specimens onset. The AE data was recorded using a micro-II multi-channel acquisition system (MISTRAS Group, Inc., USA) using two wideband differential sensors.

X-Ray Tomography

CRFPs have an excellent x-ray transmission rate, therefore they are ideally suited for defect and damage detection with x-ray tomography. In this thesis, two different processes were utilised. Radiographs of the fractured specimens were taken using a zinc iodide contrast medium with the x-ray faxitron 43885 (Rohde & Schwarz USA, Inc, USA). A transmitted light scanner digitised the analogue pictures.

Computed tomography (CT) measuremets were performed with a CT-Alpha (Procon X-Ray GmbH, Germany). All measurements were carried out in axial mode with a voxel resolution of 60 μm. Volume Graphics VGSTUDIO MAX 3.4 was used for the visualisation of the volume data. The Institute for Plastics and Circular Economy from the Leibniz University Hannover performed the CT analysis.

Scanning Electron Microscopy

A SEM Supra VP 55 (Zeiss, Germany) with an Everhart-Thornley secondary electron detector was used for a detailed analysis of the morphology. Smaller samples were cut from the full specimen to appropriate dimensions and placed on a stub with a carbon adhesive disc. As the epoxy resin has a low conductivity, the beam acceleration voltage was set to 1 kV to reduce sample charging.

Dynamic Mechanical Analysis

Dynamic mechanical analysis (DMA), performed with DMA Eplexor (Gabo, Germany), was used in this work to determine the glass transition temperature. For this, a transversely loaded UD specimen with 1 mm thickness and a 10 mm width was subjected to a 1 Hz cyclic load, while monitoring the force and displacement. During the test the temperature was constantly increased with a rate of 3 °C/min. From the resulting Storage Modulus E, the onset of the glass transition temperature T_g was determined, according to ASTM D 4065/D 7028 [35, 36].

2.1.4. Mechanical Testing

The following section presents the performed mechanical tests. Unless mentioned otherwise, the respective tests were carried out at 20 °C room temperature.

Fracture Toughness of Epoxy Nanocomposites

Single-End-Notched-Bending (SENB) tests were performed to determine the fracture toughness of the epoxy nanocomposites under mode I and mode II loadings. These tests were performed to determine the impact of particle modifications on the epoxy's mechanical properties while subjected to mode I and mode II loadings.

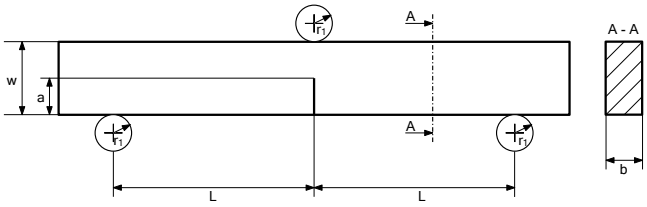

Figure 2.1.: Setup for the three-point bending SENB tests

Three-point SENB tests to determine the fracture toughness under mode I loading were performed, as specified in ASTM D5045 [37]. Figure 2.1 and Table

2.1 summarise the dimensions of the specimens and the bending setup. The following equation determines the fracture toughness K_{IC} from the test results.

$$K_{\mathrm{IC}} = \left(\frac{P}{bw^{0.5}}\right) f(a/w) \tag{2.1}$$

where P is the maximum load, b is the sample thickness, w is the width, a is the crack length and f(a/w) is the correction factor, which is dependent on the width and crack length of the sample [37].
The fracture toughness under mode II loading was obtained by using an off-centred four-point bending setup [38]. Figure 2.2 and Table 2.1 show the dimensions of the specimen and setup.

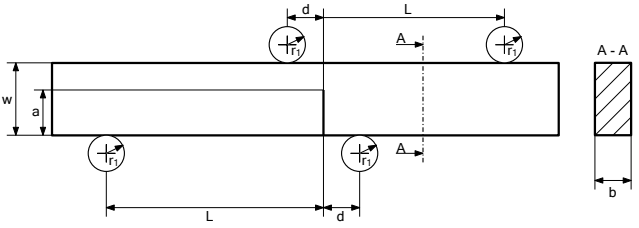

Figure 2.2.: Setup for the four-point bending SENB tests

The four-point bending setup leads to a mixed-mode loading of the crack tip. The fracture toughness values under mode I and mode II loadings, which are represented by K_{IC} and K_{IIC}, respectively, can be calculated from the four-point bending tests by using the following equation:

$$K_{\mathrm{IC}} = \frac{P}{wb} \cdot \left(1 - \frac{d}{L}\right) \sqrt{\pi a} F_I \quad \text{and} \quad K_{\mathrm{IIC}} = \frac{P}{wb} \cdot \left(1 - \frac{d}{L}\right) \sqrt{\pi a} F_{II} \tag{2.2}$$

where F_I and F_{II} are geometry-dependent correction functions obtained by FEM calculations performed by Fett [38]. P is the maximum load, L is the distance between the roller and the crack, and d is the asymmetry of the crack. The mode mixity obtained in the four-point bending tests was $> 98\,\%$ mode II.

Table 2.1.: Specimen dimensions for three- and four-point bending SENB tests

	L [mm]	w [mm]	b [mm]	d [mm]	a [mm]	r_1 [mm]
Three-Point Bending	16	8	4	-	4	3
Four-Point Bending	20	8	4	4	4.8	3

The pre-cut in the SENB specimen was cut with a 150 μm thick diamond coated blade on a Precision 220 circular saw (ATM, Germany). The final sharp crack was introduced by using a razor blade immediately before the start of the test. The bending tests were performed by using a Zwick 2.5 universal testing machine (ZwickRoell, Germany) with a cross-head speed of 1.5 mm/min. High-accuracy milled aluminium jigs were used for the sample geometry to align the sample accurately with the three- or four-point bending rig. The resulting crack-length was later measured with a microscope according to the measurement methods specified in ASTM D5045 [37].

Tensile Tests

The tensile tests were performed using a Z400 universal testing machine (Zwick-Roell, Germany) and mechanical, 100 kN pre-tensioned wedge grips for tests at 20 °C and 30 kN screw grips for tests at elevated temperature.

Table 2.2.: Specimen dimensions for tensile tests and applied standards [39–41]

	Tension Quasi-Isotropic	Tension Longitudinal UD	Tension Transverse UD	Tension In-Plane Shear	Tension Open-Hole
Standard	ASTM D3039	ASTM D3039	ASTM D3039	ASTM D3518	ASTM D5776
Length [mm]	250	250	175	280	300
Width [mm]	25	10	25	25	36
Gauge Section [mm]	150	200	125	180	200
Strain Transducer	multiXtens	multiXtens	multiXtens	DIC	DIC
Miscellaneous	GFRP Tabs	GFRP Tabs	-	-	Hole Diameter $d = 6$ mm

Tensile Properties

Quasi-isotropic (QI) and UD longitudinal and transverse tensile tests, according to ASTM D3039 [39] were performed. Table 2.2 summarises the test setup and specimen dimensions. The tensile stress σ_t is calculated with:

$$\sigma_\mathrm{t} = \frac{P}{w \cdot t} \tag{2.3}$$

where P is the tensile force, w the specimen width and t the thickness. A multiXtens (Zwick, Germany) contact extensometer measured the displacement during the test.

In-Plane Shear

Tensile tests with ±45° layup specimens determined the in-plane shear strength. The specimen dimensions (see Table 2.2) and procedures followed the guidelines in ASTM D3518 [40]. The shear strain γ_{12} is calculated with equation 2.4 from the DIC data using a virtual extensometer in the longitudinal x and transverse y directions with a measuring length L_0 of 20 mm.

$$\gamma_{12} = \varepsilon_x - \varepsilon_y \tag{2.4}$$

The following equation calculates the shear stress τ_{12}:

$$\tau_{12} = \frac{P}{2A} \tag{2.5}$$

P is the tensile force and A the crosssection of the specimen. The shear strength S_L is determined at the maximum of P below 5 % shear strain, or at 5 % if no maximum is reached at a lower strain.

Open-Hole Tension

Open-hole tension (OHT) tests were performed in accordance with the guidelines mentioned in ASTM D5766 [41]. Table 2.2 shows the dimensions of the OHT specimens. The far-field strength σ_t was calculated with Equation 2.3. The stress of the net section σ_net is determined by:

$$\sigma_\mathrm{net} = \frac{P}{(w - d) \cdot t} \tag{2.6}$$

where P is the force from the load cell, w is the width, d the hole diameter and t is the thickness of the specimen. The strength is evaluated at the maximum of P. The strain for the stress-strain curves was derived from the DIC data by

using a virtual extensometer in the longitudinal x and transverse y directions with a measuring length L_0 of 35 mm.

The notch sensitivity k_{F} of the tested material is determined with:

$$k_{\mathrm{F}} = \frac{\sigma_{t,\mathrm{OHT}}^{\max}}{\sigma_{t,\mathrm{UNT}}^{\max}} \tag{2.7}$$

where $\sigma_{t,\mathrm{OHT}}^{\max}$ is the far-field OHT strength and $\sigma_{t,\mathrm{UNT}}^{\max}$ the strengths from the unnotched tension (UNT) tests.

Compressive Strength

A hydraulic combined loading fixture (IMA Dresden, Germany), as specified by the guidelines mentioned in ASTM D 6641 M [42], was used to determine the compressive strength. Table 2.3 summarises the specimen dimensions. CEA-06-250UWA-350 (Micro-Measurements, USA) strain-gauges measured the strain during the compression tests. The compressive stress σ_{c} was calculated from the force data by using the following equation:

$$\sigma_{\mathrm{c}} = \frac{|P|}{w \cdot t} \tag{2.8}$$

$|P|$ is the absolute value of the compressive force, w is the width of the specimen and t is the thickness.

Table 2.3.: CFRP specimen dimensions and according standards [39, 41–44]

	Compression QI	Compression Longitudinal UD	Transverse Longitudinal UD	Impact & CAI	Impact & TAI
Standard	ASTM D6641	ASTM D6641	ASTM D6641	ASTM D7136 ASTM D7137	-
Length [mm]	140	140	140	150	250
Width [mm]	25	10	25	100	60
Gauge Section [mm]	150	200	-	10	150
Miscellaneous	GFRP Tabs	GFRP Tabs	GFRP Tabs	-	Edge-Support

Tests at Elevated Temperatures

Tensile and compressive tests under elevated temperature were performed with the Zwick 400 inside a temperature chamber. Thermocouples on the specimens and the test fixture continuously monitored the temperature. Before examining

a new temperature, the chamber was heated and soaked for at least 20 minutes before testing began. All specimens were stored inside the heated chamber before testing to enable fast specimen changes and ensure isothermal temperature distribution inside the specimens. After clamping, the specimen was held for another 5 minutes at the target temperature before starting the test.

Interlaminar Fracture Toughness

The mode I interlaminar energy release rate (ERR) was determined by using double cantilever bending (DCB) tests. The dimensions and setup were chosen according to the guidelines specified in ASTM D 5528 [45] (see Figure 2.3 and Table 2.4). The ERR G_{IC} was determined with the modified compliance calibration method, with the following equation:

$$G_{\mathrm{IC}} = \frac{3P^2C^{2/3}}{2Abh} \tag{2.9}$$

where P is the load, b is the specimen width, a is the delamination length, h is the specimen thickness, $C^{2/3}$ is the cube root of the compliance and A is the slope of the least square plot of the normalised delamination length a/h against the cube root of the compliance $C^{2/3}$.

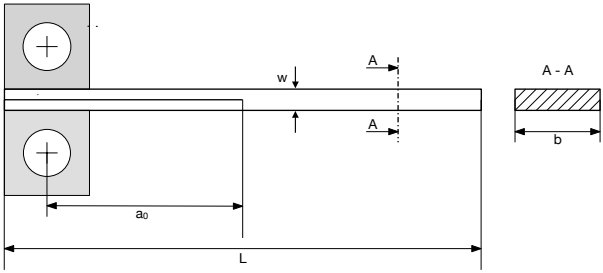

Figure 2.3.: Specimen and setup dimensions for the DCB test setup

The mode II ERR was determined with end notched flexure (ENF) test, as specified by ASTM D7905 [46]. The specimen dimensions and experimental setup are shown in Figure 2.4. The ERR was determined using the compliance calibration (CC) method:

$$G_{\mathrm{IIC}} = \frac{3mP_{Max}^2a_0^2}{2b} \tag{2.10}$$

where P_{Max} is the maximum force, a_0 is the crack length, b is the specimen width and m is the CC coefficient that is determined according to the guidelines mentioned in ASTM D7905.

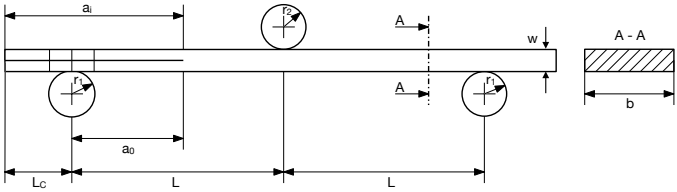

Figure 2.4.: Specimen and setup dimensions for the ENF test setup

Bending

Three-point bending tests, according to DIN EN ISO 180 [47], determined the flexural properties. The bending setup is similar to the ENF setup (see Figure 2.4), but without the pre-crack. Table 2.4 gives the according dimensions. The resulting bending stress σ_b is determined with:

$$\sigma_b = \frac{6PL}{2bw^2} \tag{2.11}$$

where P is the force, b is the specimen width, L half of the span-width and w the thickness.

Table 2.4.: Specimen dimensions for the bending, DCB and ENF tests

	L [mm]	L_C [mm]	a_0 [mm]	b [mm]	r_1 [mm]	r_2 [mm]
Double Cantilever Bending	125	-	53	25	-	-
End Notched Flexure	50	15	30	20	5	6
Flexural Properties	90	-	-	10	6	6

Impact Testing

The dimensions and setup of the impact specimens designated for the compression tests are according to the guidelines mentioned in ASTM D7136 M (see

Figure 2.5). The impact damage was introduced using an uninstrumented drop tower (Ceast, Italy), equipped with an anti-rebound device. The impactor nose had a semi-spherical tip with a diameter of 20 mm. Table 2.3 summarises the specimen dimensions. The specimens were placed on an aluminium frame equipped with metal pins as position aids. The specimens were held in position by rubber-tipped toggle clamps with a load capacity of 1100 N. The boundary condition of the specimen in this fixture is essentially simply supported. For impacts at an elevated temperature a heated chamber surrounding the clamping area was utilised. The procedure used is similar to the one explained in Section "Tests at Elevated Temperatures". For impacts below room temperature, the specimen was tempered in a CTC256 climate chamber (Memmert, Germany) and then impacted within 10 seconds after removal while continuously monitoring the temperature with thermocouples.

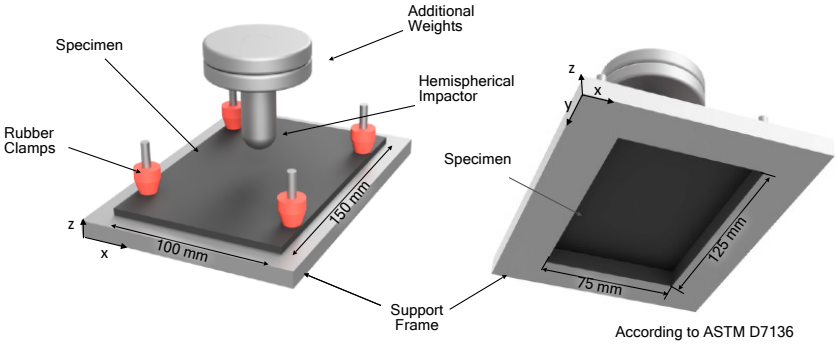

Figure 2.5.: Test setup and specimen dimensions for the impaction of the compressive specimen

To determine the residual tensile strength, the compressive specimen's size is not practical, as no available machine could apply the tensile force required to fracture the sample. Therefore, the specimen's width was scaled so that the force to reach the undamaged strength could be reached with the available 250 kN grips. This resulted in a specimen width of 60 mm and a length of 250 mm, which is a 40 % scaled-down version of the compression fixture, in order to achieve a similar loading setup with the smaller width samples. Figure 2.6 and Table 2.3 display the dimensions of the setup and the specimens. An unistrumented Primus 1700

Plus (Coesfeld Materialtest) drop tower equipped with an anti-rebound device and a semi-spherical impactor with a diameter of 12.5 mm was used for the impaction. For impacts at elevevated temperature specimens were heated to the desired temperature in a U10 oven (Memmert, Germany) and then impacted within 10 seconds after removal, while the temperature was continuously monitored with thermocouples.

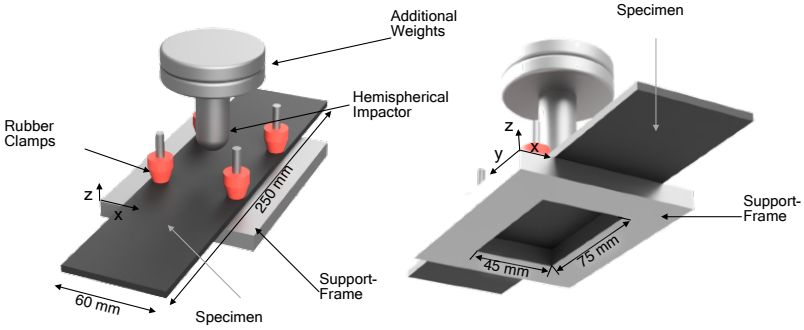

Figure 2.6.: Test setup and specimen dimensions for the impaction of the tensile specimens

Residual Strength

Residual compressive strength tests were performed using a Z400 universal testing machine (ZwickRoell, Germany). The residual strength was determined using a fixture specified in ASTM 7137 M [44] (see Figure 2.7). DIC measurements of the surface displacement field were used to make sure no undesired bending during the compression test occurred. The compressive stress was evaluated using Equation 2.8.

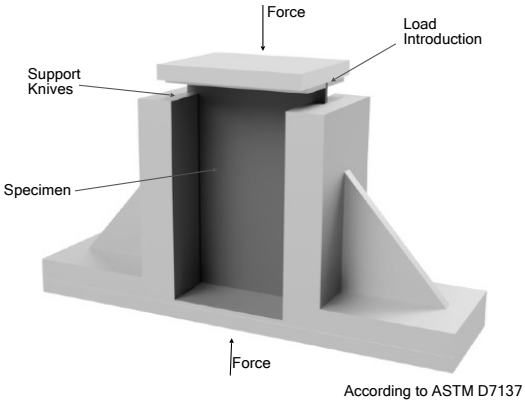

Figure 2.7.: Fixture for the determination of the compressive residual strength

The residual tensile strength measurement is not straight forward because the orthotropic ply behaviour leads to free edge stress and subsequent formation of delaminations, which is one of the dominant damage mechanisms for sufficiently thick plies on coupon level [48]. However, this does not resemble laminated panels where stress concentrations resulting from impact damage occur at a greater distance from the edge. In this case, the stress concentration and edge delamination do not influence each other significantly. A clamping device was developed, which counteracts the peel stresses at the specimens' free edges, suppressing edge delamination growth. The clamping supports the sample's edges on a width of 5 mm on each side (see Figure 2.8). An adhesive tape with a PTFE coating was attached to the clamping surface to minimise the friction between clamping and the specimen. A window with a width of 40 mm and a height of 60 mm in the middle of the clamping device enabled the usage of DIC during testing. No negative influence of the clamping on the tensile-strain-distribution could be observed and proposed clamping led to the result that the edge delamination damage does not mask the influence of the impact damage on the residual strength. An 8802 servo-hydraulic test system (Instron, USA) equipped with hydraulic grips and a 250 kN force transducer was utilised for the tensile tests. The tensile stress and strength was evaluated using Equation 2.3.

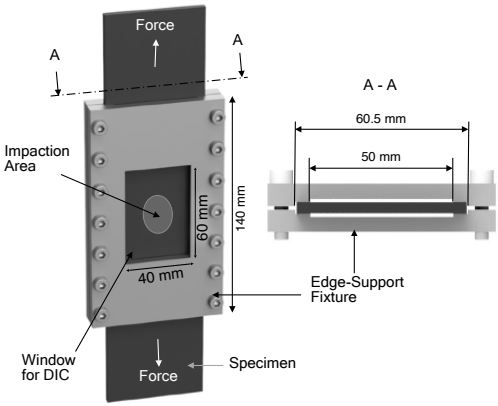

Figure 2.8.: Test setup for the determination of the residual tensile strength

3. Nanoparticle Modified CFRPs

As stated in the introduction, this chapter investigates the influence of matrix modification using CNPs on the damage tolerance of composites. The working hypothesis for this chapter is:

The addition of CNPs into the matrix introduces additional energy-consuming damage mechanisms into the composite and leads to crack blunting at stress concentrations due to the formation of dispersed local damage. The effect of the CNP modification depends on the ply thickness, as it controls the stress state in the laminate.

In the following, the state of the art concerning scaling effects in CFRP and nanoparticle modification of epoxy is described. Subsequently, the utilised materials and test procedures are displayed, followed by the presentation and discussion of the results.

3.1. State of the Art

Size and Scaling Effects in CFRP

The influence of the ply thickness has been studied in-depth for a long time [49]. The transverse strength of a constrained UD ply increases significantly with decreasing ply thickness [50–53]. The adjacent plies constrain the embedded ply and reduce the available elastic energy, thereby delaying the damage propagation in the matrix. This deterministic effect is called in-situ strength [18, 54, 55].

The 'thin-ply' laminates, which are characterised by a ply thickness less than 60 μm, have gained importance in the past few years. These ply thicknesses were developed with the advancement and industrialisation of the spread-tow process, as shown by Kawabe [56] and Sihn [13]. Quasi-static tests on unnotched multi-directional thin-ply laminates showed that the first-ply failure (FPF) was almost delayed until ultimate failure took place. This leads to considerably higher

strength and thus greater design space than the laminates with thick plies [13, 18, 19, 57]. Further, the initiation of delamination at matrix cracks or free edges is either delayed or suppressed [13, 18, 58, 59]. Delamination is the dominant failure mechanism in laminates with sufficiently thick plies. It is initiated at matrix cracks or free edges in tensile tests and easily propagates through the interply interface. The delamination then propagates into the adjacent interfaces through transverse and off-axis matrix cracks. It eventually reaches the interfaces with the 0° plies and isolates them, thereby leading to the complete gauge section delamination of the interfaces adjacent to the 0° plies. This results in early delamination failure [7, 14, 15]. In contrast, the dominant failure mode in thin-ply laminates is fibre failure [13, 18]. The static tensile strength of notched thin-ply composites is significantly lower than that of thick-ply laminates because the lack of stress relaxation through matrix damage leads to a higher stress concentration and premature failure in the former. Consequently, notched thin-ply laminates exhibit damage initiation at higher loads than thick-ply laminates; however, the ultimate notch strength of thin-ply laminates is significantly lower than that of thick-ply laminates. This creates a drawback in the application of thin-ply composites because it limits the design space that was enabled by the unnotched strength [13, 18, 60].

Damage tolerance considerations also constrain the design space of load-bearing composites because a certain amount of damage is assumed to exist in the composite structure [1–3]. Due to the layered structure of the composites and the resulting low out-of-plane strength, laminates are susceptible to the damage caused by contact with foreign objects, which can often be classified as LVI. LVI leads to the formation of local damage, which is commonly referred to as BVID, because it is difficult to detect visually. The damage caused by LVI is also dependent on the ply thickness. Thick-ply laminates exhibit extensive matrix cracking and delamination, whereas thin-ply composites suppress matrix cracking during LVI and exhibit large projected delamination areas due to the propagation of a single or a few extensive delaminations through the laminate [18, 19]. However, the CAI strength of thin-ply composites is improved because fewer larger delaminations divide the laminate into stiffer and stronger sub-laminates, unlike single plies in thick-ply laminates. As a result, thin-ply composites offer the possibility to improve composites' CAI strength, thereby unlocking additional lightweight construction potential for composite structures [61, 62].
However, the following question arises from the presented literature review: How

can the drawbacks of high-performance composites, namely large delamination areas and notch sensitivity in thick- and thin-ply composites, be addressed?

Carbon Nanoparticle Modified CFRPs

It is well established that incorporating a second phase of either soft or rigid fillers on a micro-scale can greatly enhance epoxy fracture toughness through different toughening mechanisms [63]. Generally, rigid fillers with good adhesion to the matrix interfere with crack growth via pinning, branching, bridging and deflection at the crack tip [64], which is resulting in a higher toughness and rougher fracture surface. Conversely, weakly bonded rigid particles debond easily to activate diffused matrix shear yielding or plastic void growth, thus dissipating more energy [65, 66]. Higher toughening levels can be achieved from soft rubbery particles by cavitation, promoting matrix shear yielding and further plastic deformation [67]. Since the advent of nanotechnology, nano fillers have been widely investigated as filler material for brittle polymers, as they promise a high impact on the mechanical properties with a comparably low filler content [68]. As a result several nano fillers have been investigated in the literature, such as silica nanoparticles [69], aluminium nanoparticles [70], nano clays [71, 72] and a wide range of CNPs. Besides the filler material itself, the size, morphology, volume fraction, and dispersion of the particles influence the nanocomposites' resulting properties [73, 74]. This thesis focuses on carbon nanotubes (CNTs) and few-layer graphene (FLG), both are allotropes of carbon and consist of a graphene based structure. Graphene is a honeycomb-like structure of a single sp^2-hybridised carbon atom layer (thickness = 0.35nm), with unique physical properties [75, 76].

Single-wall carbon nanotubes (SWCNTs) consist of a single graphene layer rolled up to a tube, whereas multi-wall carbon nanotubes (MWCNTs) consist of several layers. Due to the carbon backbone, CNTs offer outstanding stiffness and strength properties. Studies show that the modification of polymers with CNTs leads to a significant increment in the polymer's fracture toughness. Meeuw et al. [77] reported increments in fracture toughness up to 25 % for SWCNTs with a filler content of 0.1 wt. %. This increase in fracture toughness is caused by crack tip interaction and the formation of micro-damage at the nanoparticles. These micro-damage mechanisms are nanoparticle matrix debonding, CNT pull-out and nanotube breakage [78–81]. Pull-out can result in crack bridging [79, 81, 82]. SWCNTs offer, compared to MWCNTs, a higher geometrical efficiency

due to their higher density specific surface, resulting in higher fracture toughness increments and optimal filler levels at lower CNT concentrations [21, 77].

FLG is a derivative of graphene consisting of several graphene layers, stacked together with Van-der-Waals bonds between the layers. Graphene-based, layered particles exhibit a high potential for improving mechanical properties, due to their mechanically high effective surface [21]. The addition of small amounts of FLG or FLG-oxide increases the fracture toughness significantly. Meeuw et al. reported increments up to 90 % for the mode I fracture toughness with a concentration of 0.05 wt. % for FLG. Due to the layered structure FLG offers additional damage modes in comparison to SWCNTs [20], as layer separation and layer shearing lead to plastic yielding of the matrix and micro-voids formation [20, 83]. These mechanisms were already suggested for other layered particles such as silica [69]. Furthermore, crack pinning and bifurcation, crack deflection, and crack propagation at different heights at the graphene nanoparticles hinders crack propagation [20]. Detailed summaries on the toughening mechanisms for nanoparticles are given by Quaresimin et al. [74] and Marouf et al. [84].

Thus, the addition of CNPs as a third phase could significantly improve the performance of fibre-reinforced plastics (FRPs). Few studies observed increments in the mode I and mode II interlaminar fracture toughness due to interaction of the crack tip with the CNPs and the formation of additional damage modes at the CNPs [85–87]. It is noteworthy that interlaminar toughness is not the only property that is affected. Liu et al. [88] reported that the interfacial adhesion and mechanical properties of the matrix were significantly improved upon modification with silica nanoparticles in single fibre fragmentation tests. Although there was no significant impact on the fibre–matrix interfacial debonding stress in transverse fibre-bundle tests involving nano silica modified epoxy, a reduction was observed in the stress concentration caused due to the residual thermal stresses [89]. Tian et al. [90] performed micro-droplet, transverse fibre-bundle tension and short-beam shear tests and observed that silica nanoparticles improved the interfacial properties between the carbon fibre and epoxy. This is because the nanoparticles increased the energy dissipation, leading to efficient stress transfer during fracture [90]. Knoll et al. [91] achieved an increased fatigue lifetime in the tension-tension regime with FLG or MWCNTs modified CFRPs, as the CNPs added new stress-relieving mechanisms to the damage mechanism in the matrix. Leopold et al. [92] studied cross-ply CFRPs partially modified with FLG, wherein the 0° or the 90° ply was modified. They observed that

the 0° modification had a positive impact on the ultimate strength and delayed damage initiation, despite the fibre domination. A modification of the 90° ply resulted in a delay of matrix crack initiation. Positive effects of the CNP modification on the impact damage and the resulting residual compressive strength were observed by Kostopoulos et al. [93] and Mannov et al. [94].

However, the mechanical properties and damage mechanisms are highly dependent on ply thickness, as discussed above. The only study that has investigated the influence of nanoparticle modification on thin-ply laminates was performed by Moon et al. [95]. They observed that the MWCNT modification led to increments in the tensile strength and resistance against material degradation in a space environment.

This study highlights the impact of SWCNT and FLG modification and ply thickness on the resulting damage behaviour. The effects of different carbon particles and their concentrations are investigated by determining the fracture toughness of epoxy-resin nanocomposites under mode I and mode II loading. The most effective CNP is selected to manufacture industrial quality CFRP prepregs with ply thicknesses varying from thin-ply (28 μm) to thick-ply (220 μm). The effect of CNP toughening on the interlaminar ERR under mode I and mode II loadings is then determined. Consequently, the influence of the CNPs on the OHT strength of laminates with ply thicknesses varying from ultra-thin-plies to thick-plies is investigated. The last section deals with the influence of CNPs on the damage resulting from LVI and the following residual compressive strength on samples with different ply thicknesses.

3.2. Materials and Experimental Setup

3.2.1. Carbon Nanoparticles

Table 3.1 lists the different CNPs investigated to determine the most appropriate CNP-filler to modify the used resin. SWNCTs and FLGs with varying aspect ratios and properties were investigated for this purpose. These nano fillers can lead to significant increments in the fracture toughness with low filler content due to their outstanding stiffness, strength and surface area [20, 21]. The TUBALL 75 and TUBALL 90 SWCNTs (OCSiAl, Luxembourg) were investigated in this study. Although both SWCNTs show almost identical geometrical properties, TUBALL 90 is purified. As a result, TUBALL 90 has a higher CNT content and

lower percentages of amorphous carbon and impurities than TUBALL 75. Tuball 75 is a standard production particle, whereas TUBALL 90 is a non-commercial product. Four FLGs with different geometries, i.e. number of layers/thickness and diameters, were examined in this study. Avan2 (Avanzare, Spain), N006-P (Angstron, USA) and N002-PDR (Angstron, USA) are pristine FLG particles, and N002-PDE (Angstron, USA) is a graphene oxide.
The different FLGs were studied because different geometries also have a distinct influence on mechanical properties. For example, the surface area of FLG particles correlates with the number of graphene layers and the particle's diameter. Accordingly, the failure modes occurring, such as layer shearing, also depend on the number of layers. In fibre-reinforced plastic composites, the particles are located in the space between the fibres. The shape spaces determine how the FLGs are aligned, which is also determined by the geometric dimensions.

Table 3.1.: Shape, size and surface parameters of the used carbon nanoparticles [73, 96–100]

	Shape	Surface Area $[m^2/g]$	Layers	Aspect Ratio	Lateral Dimension $[\mu m]$	Composition $[wt.\,\%]$
Tuball 75	Cylindrical	605	-	3570	5	C (81.96) Fe (15.01) O (2.26)
Tuball 90	Cylindrical	598	-	3570	5	C (90.61) O (6.36)
Avan2	Planar	128	10 ± 2	6250	25	O (88.33) O (9.15)
N006-P	Planar	20-30	25	140-230	$10 - 20$	C (≥ 95) O (≤ 4)
N002-PDE	Planar	400-800	5	3000	$0.35 - 2$	C (70-90) O (10-30)
N002-PDR	Planar	400-800	4	3000	$0.35 - 2$	C (≥ 95) O (≤ 2)

3.2.2. Fracture Toughness of Epoxy Nanocomposites

The resin system NTPT 402 (North Thin Ply Technology (NTPT), Switzerland) [101] was used in this study because its viscosity profile is optimised for thin-ply material manufacturing. It is a hot-melt resin with high viscosity at room temperature.

3.2.3. Composites

Several UD prepregs (North Thin Ply Technology (NTPT), Switzerland) with different ply thicknesses were used to test the unmodified and modified composites. The unmodified material is referred to as "neat", and the material modified with FLG is referred to as "nano". The prepregs were manufactured using NTPT ThinPreg 402 epoxy resin (North Thin Ply Technology (NTPT), Switzerland) and Toray T700SC-12K-60E fibres (Toray Industries, Japan). The neat material was a standard production material, whereas the nanoparticle-modified material was a custom production run. The CNP dispersion process used in these tests is identical to the procedure used to modify the resin, as described in Section 2.1.1. A large masterbatch was manufactured and was further processed at NTPT to manufacture the prepreg. Neat prepreg with fibre-areal weights (FAW) of $30\,\mathrm{g/m^2}$, $120\,\mathrm{g/m^2}$ and $240\,\mathrm{g/m^2}$ was manufactured. The nano material was manufactured with FAWs of $30\,\mathrm{g/m^2}$ and $120\,\mathrm{g/m^2}$. The remaining FAWs were obtained through block-scaling. Table 3.2 displays the results of Kötter et al.[102], who have examined the tensile properties of QI neat specimens. The data is used throughout the study for comparative reasons.

Table 3.2.: Layup, dimensions and mechanical properties of the quasi-isotropic neat material obtained from [102]

Areal Weight $[g/m^2]$	240	120	60	30
Layup	$[45/-45/90/0]_s$	$[45/-45/90/0]_{2s}$	$[45/-45/90/0]_{4s}$	$[45/-45/90/0]_{8s}$
Thickness $[mm]$	1.71	1.70	1.83	1.81
Ply Thickness $[\mu m]$	214	106	57	28
Tensile Modulus [GPa]	47.42 ± 0.75	47.15 ± 0.24	50.23 ± 0.32	$48.57 \pm 0,38$
Tensile Strength [MPa]	736.86 ± 32.6	825.49 ± 24.56	963.66 ± 18.2	956.59 ± 31.81
No. Specimens	5	5	5	5

3.2.4. Interlaminar Fracture Toughness

Neat and nano material with a FAW of $120\,\mathrm{g/m^2}$ was used with a $[0_{16}/\mathrm{PTFE}/0_{16}]$ layup to determine the mode I and mode II interlaminar ERR. The mode I

interlaminar ERR was determined by using DCB tests. The mode II ERR was determined through the ENF test.

3.2.5. Open-Hole Specimens

The layup and resulting laminate thickness for each FAW are shown in Tables 3.3, 3.4, 3.5 and 3.6. The selective application of nano plies for the 0° plies was investigated as a third configuration, in addition to the neat and nano specimens. This configuration is referred to as 'tailored' because the selective modification permits a detailed observation of the impact of the FLG modification proposed by Leopold et al. [92]. The determination of the influence of CNP modification on the failure process is generally complex due to the multiscale character of the composite. The lengths of the fractured edges of the $30\,g/m^2$ and $60\,g/m^2$ laminates were measured to determine the impact of the nanoparticle modification. This provides information on the extent of the influence of the damage and the resulting surface area created.
A python script that utilised the OpenCV library was developed to determine the fractured edge length of the net section of the OHT specimen. The steps are sequentially shown in Figure 3.1. As a first step, images were checked and if necessary modified to ensure that the pixel resolutions of the micro-sections were consistent. The image is then thresholded using Otsu's thresholding after Gaussian filtering, followed by its conversion into a binary image. The enclosed white areas in front of the crack surface, which are formed due to loose fibres, are removed. The edge length is then calculated by the canny edge detector algorithm function.

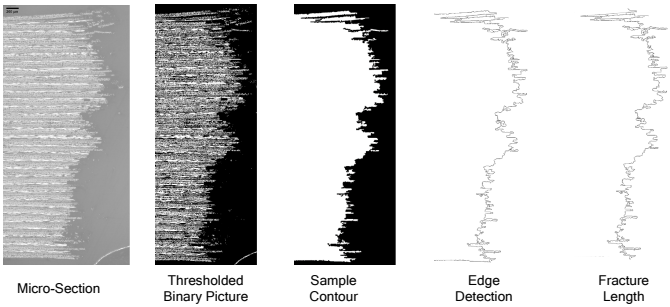

Figure 3.1.: Schematic of the image processing technique to determine the crack length of the microsections

Table 3.3.: Layup, materials and dimensions of the 240 g/m^2 specimen for OHT testing

	Neat	240 g/m^2 Tailored	Nano
Base Material	NTPT Neat 240 g/m^2	NTPT Neat 240 g/m^2 NTPT Nano 120 g/m^2	NTPT Nano 120 g/m^2
Layup	$[45/-45/90/0]_{2s}$	$[45/-45/90/0_2(\text{Nano})]_{2s}$	$[45/-45_2/90_2/0_2]_{2s}$
Thickness $[mm]$	3.79	3.77	3.96
Ply Thickness $[\mu m]$	237	236	248
No. Specimens	4	4	4

Table 3.4.: Layup, materials and dimensions for the 120 g/m^2 specimen for OHT testing

	Neat	120 g/m^2 Tailored	Nano
Base Material	NTPT Neat 120 g/m^2	NTPT Neat 120 g/m^2 NTPT Nano 120 g/m^2	NTPT Nano 120 g/m^2
Layup	$[45/-45/90/0]_{4s}$	$[45/-45/90/0(\text{Nano})]_{4s}$	$[45/-45/90/0]_{4s}$
Thickness $[mm]$	3.76	3.72	3.84
Ply Thickness $[\mu m]$	118	116	120
No. Specimens	5	4	4

Table 3.5.: Layup, materials and dimensions for the 60 g/m^2 specimen for OHT testing

	Neat	60 g/m^2 Tailored	Nano
Base Material	NTPT Neat 60 g/m^2	NTPT Neat 60 g/m^2 NTPT Nano 30 g/m^2	NTPT Nano 30 g/m^2
Layup	$[45/-45/90/0]_{8s}$	$[45/-45/90/0_2(\text{Nano})]_{8s}$	$[45_2/-45_2/90_2/0_2]_{8s}$
Thickness $[mm]$	4.03	3.75	4.03
Ply Thickness $[\mu m]$	59	59	63
No. Specimens	4	4	4

Table 3.6.: Layup, materials and dimensions for the $30\,g/m^2$ specimen for OHT testing

	Neat	$30\,g/m^2$ Tailored	Nano
Base Material	NTPT Neat $30\,g/m^2$	NTPT Neat $30\,g/m^2$ NTPT Nano $30\,g/m^2$	NTPT Nano $30\,g/m^2$
Layup	$[45/-45/90/0]_{16s}$	$[45/-45/90/0(\text{Nano})]_{16s}$	$[45/-45/90/0]_{16s}$
Thickness $[mm]$	3.65	3.76	3.95
Ply Thickness $[\mu m]$	29	29	31
No. Specimens	5	4	4

3.2.6. Impact and Compression After Impact Testing

The impact and CAI tests were performed on the neat and nano specimens. The layup $[45_m/0_m/-45_m/90_m]_{ns}$ was chosen according to the guidelines mentioned in ASTM D7136 M [43]. The exact layup, laminate and ply thickness values for all configurations are shown in Tables 3.7 and 3.8. The impact parameters, such as mass and velocity, were chosen such that they correspond to the characteristics of the LVI impacts described by Richardson et al. [24] and Sjoblom et al. [103]. The impact energy utilised was determined during preliminary tests to ensure that the delamination growth does not reach the specimen's edge because that would affect the damage sequence and the damage modes formed during the impact and consequently the residual compressive strength. The final weight and drop height of the impactor were 4.43 kg and 0.345 m, respectively, which resulted in an impact energy of 15 J.

Additionally, micro-sections were acquired from one sample for each configuration. The specimens were then cut through the middle along the short side of the specimen. They were subsequently polished and inspected by utilising a microscope.

Table 3.7.: Layup, materials and dimensions of the $240\,g/m^2$ and $120\,g/m^2$ samples for the impact and CAI tests

	$240\,g/m^2$		$120\,g/m^2$	
	Neat	Nano	Neat	Nano
Layup	$[45/90/-45/0]_{3s}$	$[45_2/90_2/-45_2/0_2]_{3s}$	$[45/90/-45/0]_{6s}$	$[45/90/-45/0]_{6s}$
Thickness $[mm]$	5.55	5.86	5.58	5.83
Ply Thickness $[\mu m]$	231	244	116	121
No. Specimens Impact / CAI	6/5	6/5	6/5	6/5

Table 3.8.: Layup, materials and dimensions of the $60\,g/m^2$ and $30\,g/m^2$ samples for the impact and CAI tests

	$60\,g/m^2$		$30\,g/m^2$	
	Neat	Nano	Neat	Nano
Layup	$[45_2/90_2/-45_2/0_2]_{11s}$	$[45_2/90_2/-45_2/0_2]_{11s}$	$[45/90/-45/0]_{22s}$	$[45/90/-45/0]_{22s}$
Thickness $[mm]$	5.15	5.25	5.14	5.30
Ply Thickness $[\mu m]$	58.52	59.66	29.20	30.01
No. Specimens Impact / CAI	6/5	6/5	6/5	6/5

3.3. Results and Discussion

In the following section, the results are presented and discussed using figures for better understanding (the quantitative data can be found in the Appendix A).

Figure 3.2 summarises the experimental campaign to determine the CNP influence on the fracture toughness of the epoxy and the interlaminar ERR of the composite.

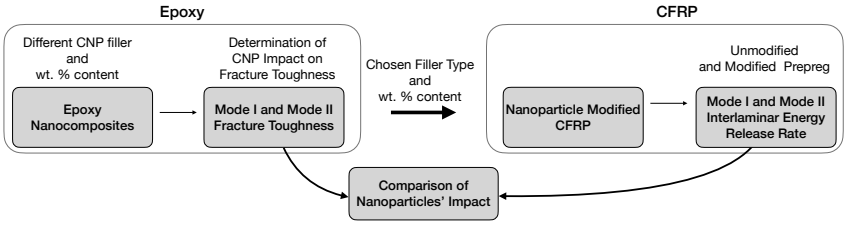

Figure 3.2.: Experimental procedure for determining and comparing nanoparticles' effects on the fracture toughness in epoxy and CFRPs

In Section 3.3.1, different nanofillers' impact on the epoxy fracture toughness is investigated to chose a filler and its concentration. With this filler, CNP modified prepreg is manufactured. The folowing Section 3.3.2, determines interlaminar energy release rates under mode I and mode II with neat and nanoparticle modified CFRP. The results from nanocomposite and CFRP testing are subsequently compared.

3.3.1. Fracture Toughness of Epoxy Nanocomposites

The impact of CNP on the epoxy's fracture toughness K_{IC} under mode I loading is shown in Figure 3.3. The fracture toughness can be significantly increased with the incorporation of CNPs, as shown in previous studies [20, 74, 104]. However, the effect of the CNPs and the occuring modes change with varying filler geometry and concentration. SWCNTs can be classified as one-dimensional fillers due to their aspect ratio, as shown in Table 3.1 [105]. They mainly exhibit crack pinning and the consequent pullout as their main interaction mode [21, 81, 106].

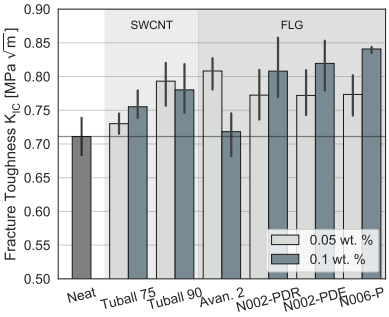

Figure 3.3.: Determination of the fracture toughness under mode I loading through the three-point bending SENB tests

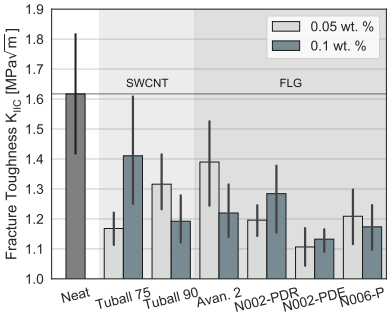

Figure 3.4.: Determination of the fracture toughness under mode II loading through the four-point bending off-axis SENB tests

The fracture toughness increase of the SWCNT modified nanocomposites ranges from 3 to 12 %, compared to neat epoxy, a trend that has been observed in other studies as well [20, 77]. The value of K_{IC}, at a filler concentration of 0.1 wt. %, increases for Tuball 75 and is reduced for Tuball 90. This demonstrates that the high purity, which results in a higher quantity of SWCNTs, is mechanically effective because the optimal filler level is reached at a lower CNP concentration. It is noteworthy that the fracture toughness of Tuball 75 with 0.1 wt. % filler content is lesser than that of Tuball 90 with 0.05 wt. % filler content despite the greater amount of pure SWCNTs by weight in Tuball 75 than that in Tuball 90 (0.075 wt. % in comparison to 0.045 wt. %). This is because the non-carbon components, such as the catalytic particles, can act as crack initiators and counteract the positive effect of the SWCNTs, as observed by Leopold et al. [107]. It is important to not only account for the quantity of CNTs but also consider the purity, type and size of the residues while selecting the nanoparticles. According to the obtained results, it can be observed that the optimum filling levels for Tuball 75 and Tuball 90 are < 0.05 wt. % and > 0.05 wt. %, respectively.

FLG can be classified as a two-dimensional filler [105], as shown in Table 3.1. FLG offers more crack interaction modes between the crack and FLG on a micro level than SWCNTs. These modes include crack bifurcation/pinning, crack deflection, separation of FLG layers, crack penetration within layers [20, 108] and greater geometric efficiency [21].

The increase in fracture toughness K_{IC} for the FLG modified nanocomposites ranges from 7 % to 19 %, compared to neat epoxy. This range is similar to the ones observed in previous studies [20, 77]. The maximum rise in fracture toughness was obtained by using N002-PDR, which is an FLG particle with a high purity and aspect ratio. The lateral dimension of the particles is relatively small. They only consist of 4 layers, as shown in Table 3.1. This provides a large surface area of the particles, thereby resulting in a high probability of interaction with the crack tip. The N002-PDE particles have almost identical dimensions; however, their oxidised nature could lead to the presence of more functional groups on the particle than those of the N002-PDR particle, thereby improving the former's compatibility with epoxy resin [109], which is not the case. The N006-P particles produced a similar performance with a smaller aspect ratio, thereby resulting in a larger number of layers and a higher lateral extension than the N002-PDR FLG. The Ångstron particles have their optimum CNP content at > 0.05 wt. %. The Avan2 particles have the highest aspect ratio and behaved differently from the Ångstrom particles. The optimal filler content concerning the mechanical performance for the Avan2 particles is below 0.1 wt. % and hence, they are the most efficient particles.

The measurement of K_{IIC} has been controversially debated because the obtained value is highly dependent on the shape and loading condition of the specimen [110]. It has been proven that the cracks formed under mode II loading originate from the crack tip in the direction of the inserted pre-crack and follow a curved path that eventually converges with the direction of mode I loading, which is about 70° [111]. Therefore, it is questionable if the pure mode II toughness is measured. However it is still a valuable parameter to evaluate the influence of CNPs on the mechanical behaviour, as mode II loading does occur in the interply of CFRPs [112]. It was observed that the matrix fails under mode I and mixed-mode loadings, resulting in the formation of typical hackles.

The mode II fracture toughness is shown in Figure 3.4. The crack is initiated under mode II loading, which is followed by its propagation under mixed-mode loading. This also explains the similarities between the fracture toughness trends observed under mode I and mode II loadings because the CNP modification contributes to the mode I fracture toughness. The relatively high scatter is attributed to the large amount of stored energy because the process zone obtained under mode II is significantly larger than that obtained under mode I. The particles reduce the fracture toughness under mode II loading significantly. This is because the crack propagation in particle-filled polymers can be initiated in the

mode I direction due to craze formation at defects or impurities [33, 113, 114]. From the result it can be concluded, that FLGs with a small lateral dimension offer a higher mode I increment in fracture toughness, but a greater reduction under mode II loading. A reason could be, that the number of FLGs per weight unit is much higher for particles with a small lateral dimension. Therefore they offer more "defects" for failure initiation under mode II loading.

Avan2 was chosen as the nanofiller for the fibre composite modification process in accordance with the results mentioned above. The reasons behind this selection is given below.

- The application of these particles led to the maximum weight specific toughening efficiency. This helps avoid filtering effects during the prepreg production process because the number of particles is significantly lower.
- Because FLG offers more damage modes than SWCNTs, the FLG could provide more damage modes inside the composite than those offered by CNTs.
- The reduction in the mode II fracture toughness is minimal.

3.3.2. Interlaminar Fracture Toughness

The interlaminar fracture toughness is determined through the DCB and ENF tests, as discussed in Section 3.2.4. Figure 3.5 shows the mode I ERR for the neat and nano specimen's crack growth. The ERR of the nano specimen at the point of crack initiation is 35 % higher than that of the neat specimen. The ERR trends for neat and nano specimens converge as the crack propagates.

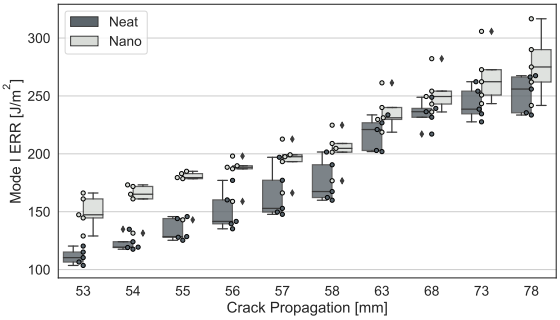

Figure 3.5.: Energy release rates of the mode I specimen for different crack lengths

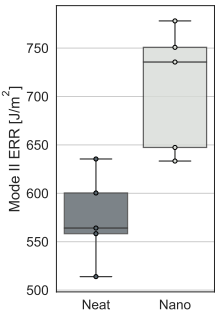

Figure 3.6.: Mode II energy release rate

Figure 3.7 shows SEM images of representative fracture surfaces of both configurations at crack lengths ranging from approximately 55 mm to 56 mm. The differences between the fractured surfaces of the two materials are clearly visible. In the neat specimen, the crack propagation mainly occurs in the fibre–matrix interface, resulting in a primarily smooth fracture surface. Resin-rich areas cause occasional cohesive fractures. The fracture pattern of the nano specimen is clearly different because the crack plane varies frequently, with a substantial part of the crack propagating cohesively through the matrix. Chu et al. also incorporated FLGs with similar dimensions into CFRPs, also manufactured by NTPT. They utilised Raman spectroscopy to prove that the FLG particles were oriented tangentially to the fibre through filtering effects and spatial restrictions [115].

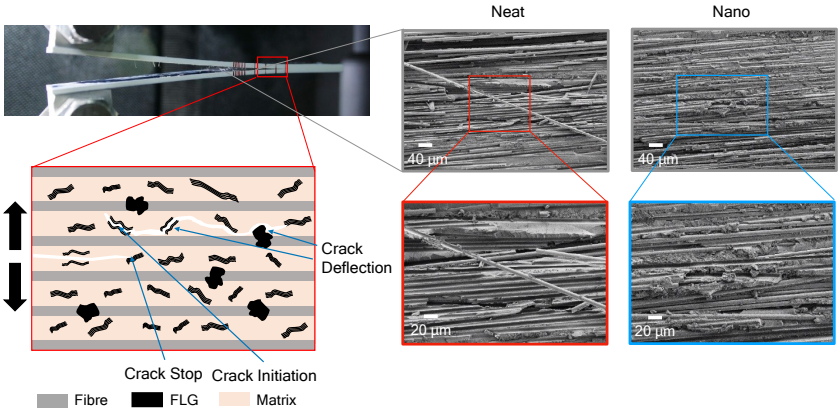

Figure 3.7.: Comparison between the fractured surfaces of the neat and FLG-modified DCB specimens, and a schematic representation of the occurring failure modes

The higher amount of cohesive matrix failure is caused by crack deflection through the separation of FLG layers, which was also observed by Ning et al. [86]. The increased surface roughness can be related to the crack pinning of the FLG particles and the in-plane deflection, which forces the crack to switch to mixed-mode loading. Because crack propagation under mixed-mode conditions leads to higher energy absorption than under mode I loading, it leads to a rise in the fracture toughness of the material. Ning et al. [86], Kostagiannakopoulou et al. [85] and Ahmadi-Moghadam [87] also reported the existence of these failure modes. They investigated resin interfaces doped with different FLG particles. In addition, FLG layer openings lead to the formation of micro-cracks in other planes. This results in the early initiation of fibre bridging, which is observed during macroscopic testing. Schematics of the occurrence of these effects and the crack interaction modes are shown in Figure 3.7. The convergence of the ERR trends with increasing crack propagation is attributed to the formation of fibre bridging in the neat specimens.

Kostagiannakopoulou et al. [85] also investigated the influence of FLG with a 0.5 wt. % concentration in the matrix, on mode I ERR. They observed increments of 3 % for initiation and 61 % during propagation in the mode I fracture toughness. The difference between the results presented in this study and the one

discussed above could be attributed to differences in manufacturing. The specimens in the other study were manufactured by hand layup, which could lead to a variation in the interply thickness or fibre volume content (FVC), which influences the FLG orientation and therefore the crack interaction behaviour. Ahmadi-Moghadam et al. [116] investigated the influence of different FLG particles having a concentration of 0.5 wt. % on the interlaminar ERR of a GFRP. They observed that the increment in the mode I fracture toughness varied from 11 % to 39 %.

In the presented tests, the addition of FLG increases the mode II ERR by 31 %, as shown in Figure 3.6. This result is at first a surprising outcome given the results of the SENB tests, as shown in Figure 3.4. However, mode II failure at the interface is dominated by the mode I and mixed-mode fractures in the polymer [112], as described above. Therefore, it is unclear if the mode II fracture toughness can be classified as a 'real' material property [117]. Figure 3.8 shows the SEM pictures of the fracture surface of an ENF specimen. The effect of FLG modification is clearly visible. A substantial proportion of cohesive failure can be observed for the FLG-modified specimen, which is similar to the observations made for the mode I fracture surfaces. Matrix damage initiates at the FLG particles under mode II loading, which leads to extensive hackle formation. This increases energy consumption and leads to a higher fracture toughness. The hackles or matrix cracks interact with the FLG and increase the ERR as well. Ahmadi-Moghadam et al. [116] investigated the mode II ERR of a GFRP modified with FLG and observed an increment of 12 % in the fracture toughness. This value is substantially lower than the values obtained in the current study. This is attributed to the lower uniformity in the micro-structure due to the utilised materials and the higher FVC in [116].

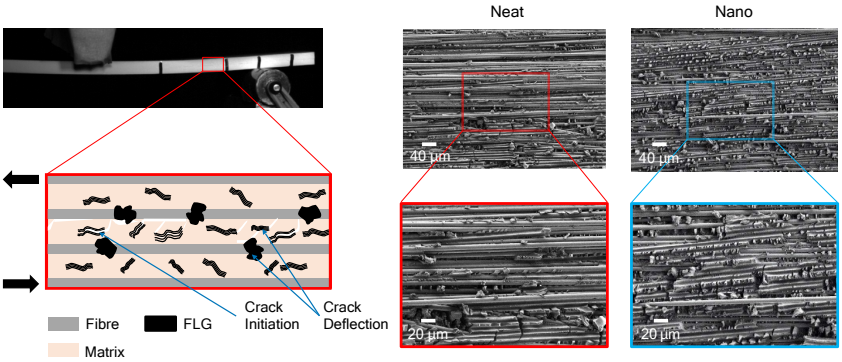

Figure 3.8.: Comparison between the fractured surfaces of the neat and FLG-modified ENF specimens, and a schematic representation of the occurring failure modes

Figure 3.9 summarises the differences between the ERR values obtained under mode I and mode II loading in the epoxy-resin and the fibre-composite. In addition, it demonstrates the efficiency of the FLG matrix modification as the low CNP content leads to a high increase in toughness. An increment of 31 % was observed in the epoxy-resin in the mode I ERR, whereas the fibre-composite reported an enhancement of 23 %. The trends oppose each other under mode II loading. The fracture ERR increased by 35 % in the fibre-composite, whereas it is reduced by −17 % in the modified epoxy-resin. Yet, as stated before, the mode II fracture toughness in the epoxy-resin must be judged with caution. Still, it is an indicator that new failure modes are occurring due to the FLG modification. No other studies have been conducted on the impact of CNP modification of CFRPs on the interlaminar fracture toughness with industrial-grade material. Nevertheless, other approaches have been investigated to improve the performance of thin-ply composites. Pascoe et al. [118] manufactured interlocking thin-ply reinforcements. They reported a rise of 75 % in the mode I fracture toughness during crack propagation. However, they did not observe any increment in the fracture toughness under mode II loading. Cugnoni et al. [60] added a thermoplastic interleaf to the interface or used a toughened matrix and obtained similar G_{IIC} values to those reported in the present study.

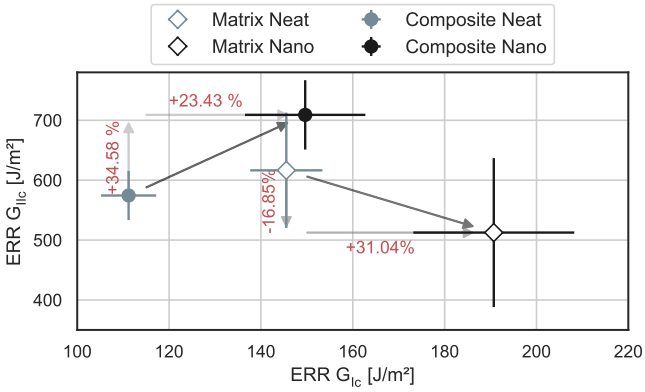

Figure 3.9.: Comparison between influence of FLG modification on the mode I and mode II ERRs of epoxy-resin and the fibre-composites

3.3.3. Fibre Volume Content

The incorporation of CNPs into the resin increases the resulting resin's viscosity [33]. This affects the manufacturing process of the prepreg and resin flow during the curing process in the autoclave, resulting in varying resin contents. As a result, the FVC varies with the ply thickness and/or resin modification. Generally, this problem arises while comparing different resins [119] or different ply thicknesses [18]. Samples of two OHT specimens were taken from two plates of every configuration to obtain an average value of the FVC. The manufacturer's data on the density of the matrix (1.21 g/m^2 [101]) and fibres (1.8 g/m^2 [120]) were used to calculate the FVC from the fibre weight content. The results are shown in Table 3.9. The FVC decreases with increasing ply thickness. In addition, the fibre content of the neat specimen is greater than that of the modified one. This behaviour is attributed to the relatively high viscosity of the modified resin, resulting in less resin being pushed out of the laminate during the autoclave process. The following results are normalised to the FVC of the 240 g/m^2 material, which is 55.6 %.

Table 3.9.: Fibre volume content for different ply thicknesses, layups and materials

Areal Weight $[g/m^2]$	Fibre Volume Content [%]			
	30	60	120	240
Neat	57.80 ± 0.51	58.01 ± 0.07	56.07 ± 0.57	55.57 ± 0.92
Tailored	57.69 ± 0.69	57.95 ± 0.21	55.96 ± 1.3	54.80 ± 0.21
Nano	55.04 ± 0.72	56.32 ± 0.61	54.68 ± 0.26	53.01 ± 0.26

3.3.4. Open-Hole Tensile Strength

The following section presents the results of the OHT experiments. Figure 3.10 summarises the different methods used to investigate the behaviour of the material.

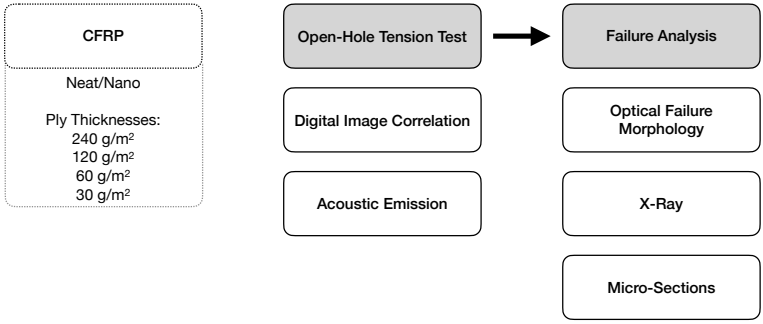

Figure 3.10.: Schematic of the procedure and methods used for the OHT tests and the subsequent examination of the fractured samples

The OHT far-field strengths of the tested configurations are shown in Figure 3.11. The thin-ply effect is evident for the neat material because its strength decreases with decreasing ply thickness. Thus, the thin-ply laminates cannot fully utilise the strength advantage they possessed in unnotched laminates, as shown in Table 3.2. This effect is more pronounced if the FVC is taken into account, as shown in Figure 3.11 b). The impact of the FLG modification on strength is not uniform for all thicknesses. Thus, the following results will be discussed according to ply thicknesses, from high to low. Nevertheless, the illustrations' design is chosen so that the effect of all ply thicknesses and modifications are shown together.

This decision was made on purpose so that the impact of the ply thickness and particle modification on the damage behaviour is comparable.

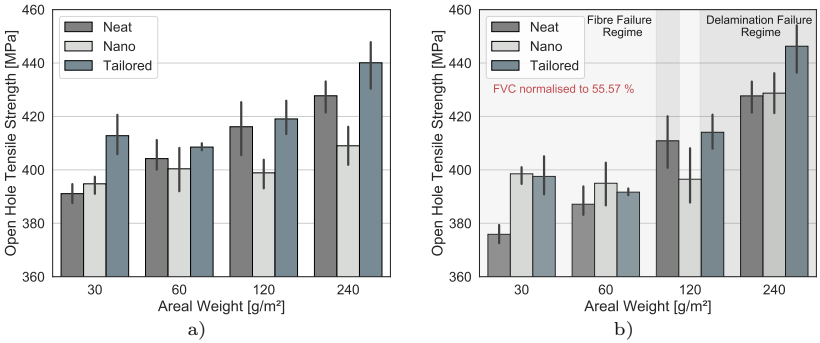

Figure 3.11.: a) Resulting OHT strength of the tested specimen and b) normalised with respect to an FVC of 55.6 %

Ply Thickness: 240 g/m^2

Figure 3.11 presents the resulting OHT strengths. The variation in the OHT strength for the different configurations is significant. With reference to the neat material, the strength of the tailored layup increases and decreases for the FLG-modified material. However, the relatively low FVC, as shown in Table 3.9, causes a reduction of the nano specimen's strength. All following results are discussed with results normalised to the same FVC. The change in the failure behaviour of the modified material is nonetheless visible. Figure 3.12 and Figure 3.13 show the engineering strain ε_x and ε_y distributions, derived from DIC, before final failure. The strain distribution of the neat specimen indicates that several matrix cracks were formed at the hole across the two upper $\pm 45°$ plies, which already interfere with each other. It further points to excessive deformation at the edges, indicating severe edge delamination of the 45° plies. The tailored approach reduces these strain concentrations. The increased interlaminar ERR between the 0°/90° and 0°/45° plies leads to less visible damage before the final failure, in comparison to that of the neat specimen. A fully modified specimen can further improve the damage suppression. In the current case, only a minimal amount of damage growth can be detected in the 45° direction. In addition, the delamination is limited in ε_y direction.

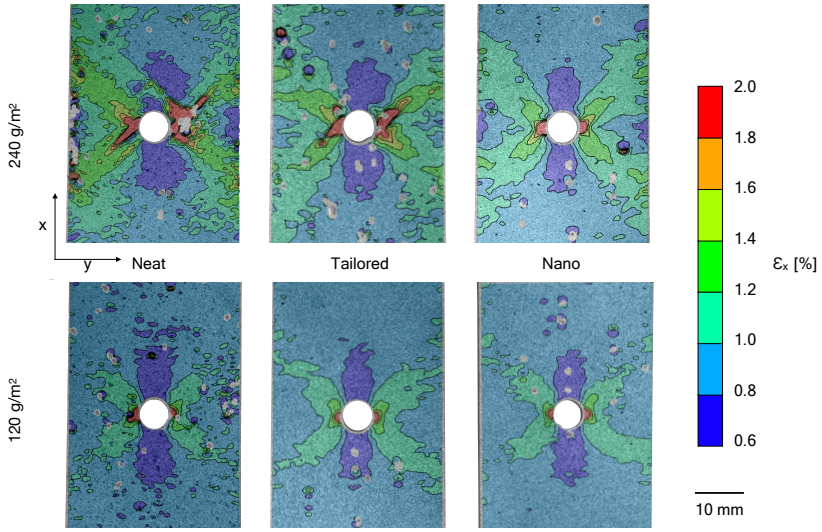

Figure 3.12.: Tensile engineering strain ε_x distribution for neat, tailored and nano specimens with ply thicknesses of 240 g/m^2 and 120 g/m^2 before fracture

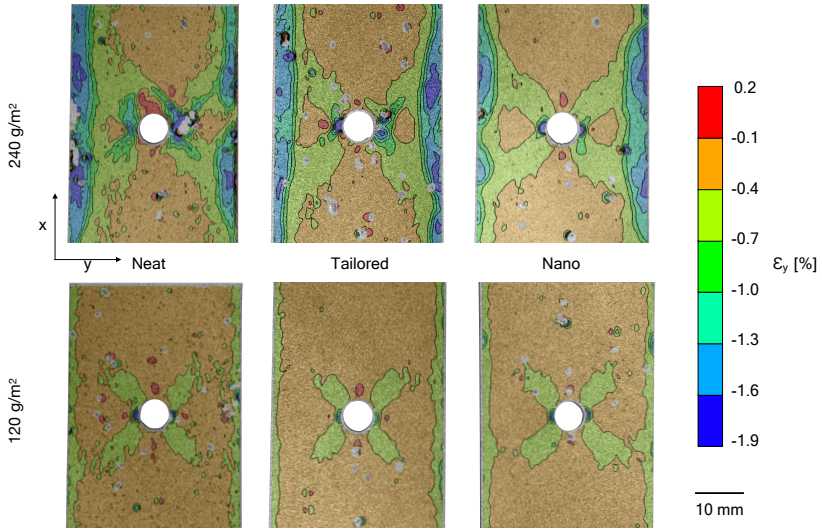

Figure 3.13.: Lateral engineering strain ε_y distribution for neat, tailored and nano specimens with ply thicknesses of 240 g/m^2 and 120 g/m^2 before fracture

Figure 3.14 shows the representative stress–strain curves for every configuration of the OHT specimens. There is a reduction visible in the nonlinear region of the nano specimens. The micro-sections, as shown in Figure 3.16, provide additional insights on the impact of FLG modification on the failure. The 0° degree plies of the neat specimen are heavily delaminated, and the delamination of the middle plies has propagated throughout the sample. Because all 0° plies failed at a height that was equal to that of the hole, it is evident that only the 0° plies contributed to the ultimate strength.

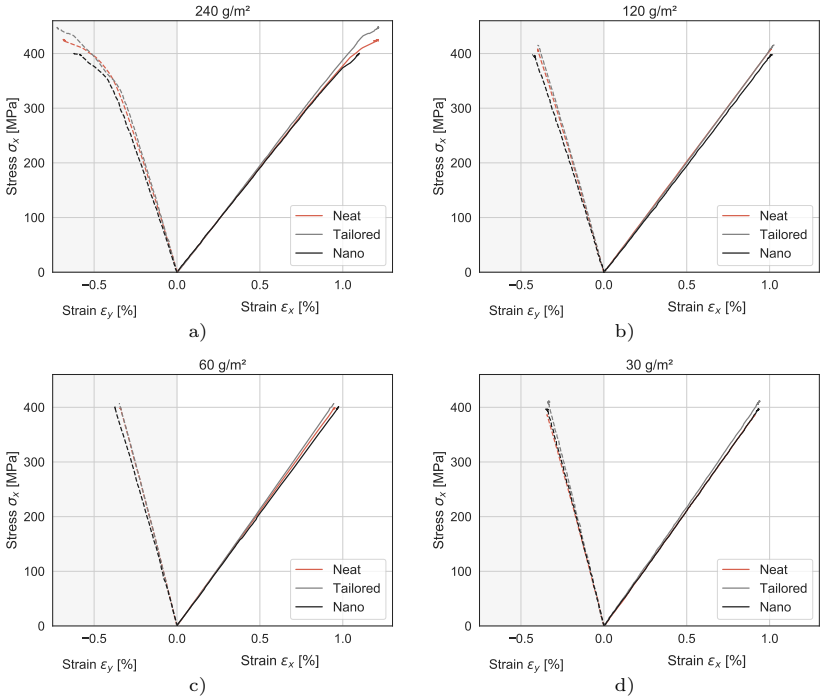

Figure 3.14.: Variation of the tensile far-field stress σ_x with the tensile ε_x and lateral ε_y strain of the OHT specimens for ply thicknesses of (a) 240 g/m^2, (b) 120 g/m^2, (c) 60 g/m^2, and (d) 30 g/m^2

The tailored approach alters the failure behaviour, as visible in the failure images in Figure 3.15 and the micro-sections in Figure 3.16. Although the 0° plies are also delaminated from the remaining laminate, this approach reduces the delamination length significantly. Further, the 0° plies do not fail at the same

point accross the thickness of the specimen. This indicates that the 45° plies significantly influence the ultimate strength. Thus, the matrix modification shifts the delamination of the 0° plies from the rest of the laminate to a relatively high strain value, as shown in Figure 3.14.

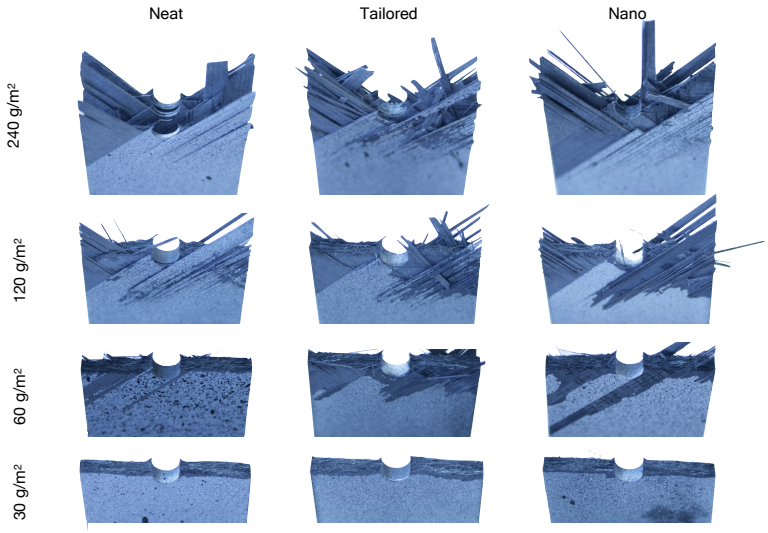

Figure 3.15.: Fracture patterns for all configurations of the OHT specimens

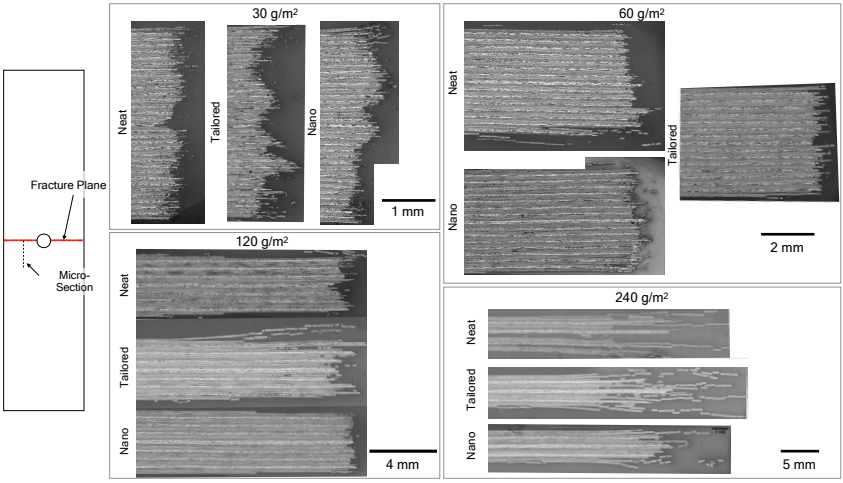

Figure 3.16.: Micrographs of the tested configurations depicting the fractured sections next to the holes

The reduced delamination size is evident in the radiographs, as shown in Figure 3.17. The nano specimen exhibited a more brittle failure than the neat and tailored specimen, as shown in Figure 3.16. Limited delamination was observed, and the resulting fracture area was very brittle. However, the failure of the 0° fibres is much less distributed. The increased ERR reduces the propagation of delamination and thus reduces the stress concentration. This results in the overlapping of the two effects, namely the increased contribution of the 45° plies to the strength and the lower reduction of the stress concentration through delamination. Consequently, the strength of the laminate is unaffected.

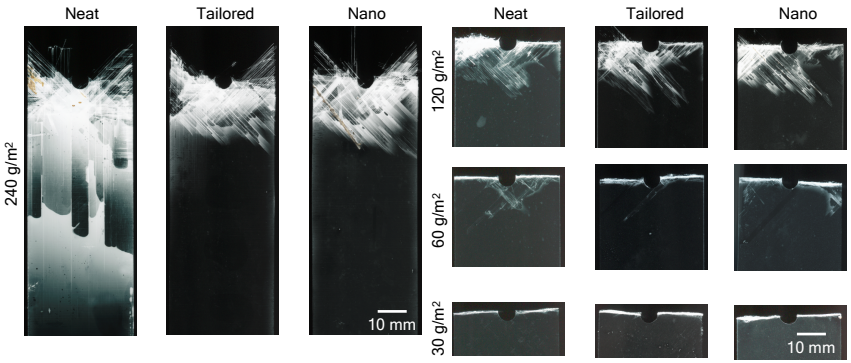

Figure 3.17.: X-ray images of all configurations of the fractured OHT specimens

Figure 3.18 shows the damage initiation with respect to the ultimate strength. The complete modification of the laminate increases the damage initiation stress significantly, thereby providing a larger design space than the non-modified laminate.

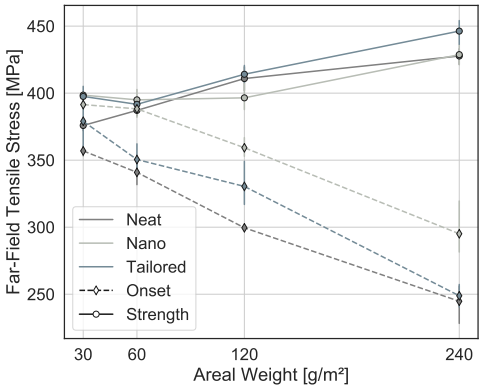

Figure 3.18.: Damage initiation and ultimate strength of the OHT specimens of the neat, nano and tailored configurations for different ply thicknesses

Ply Thickness: $120\,\mathrm{g/m^2}$

The reduction of the ply thickness from $240\,\mathrm{g/m^2}$ to $120\,\mathrm{g/m^2}$ induces significant changes in the overall damage behaviour. The decreasing ply thicknesses lead to

different effects that influence the effectiveness of the higher interlaminar ERR. Both external mechanical loads and thermal loads resulting from autoclave cause the formation of interlaminar shear stresses. A reduction in the ply thickness leads to a decrease in the ply stiffness, which induces lower interlaminar shear stresses. Consequently, the apparent interlaminar fracture toughness increases with reducing ply thickness. This implies that the external loads required by thin-ply laminates are greater than those required by thick-ply laminates to achieve identical stress states between the plies.

The different strain distributions of the investigated ply thicknesses, before final failure, are shown in Figure 3.12 and Figure 3.13. The strain field ε_x of the $120\,\mathrm{g/m^2}$ laminates generally exhibits a more localised distribution of strain around the hole than that of the $240\,\mathrm{g/m^2}$ laminates. The extent of the edge delamination is limited for the $120\,\mathrm{g/m^2}$ laminates. The suppression of damage is also visible in the stress–strain diagram because non-linearities are not observed before failure.
The differences among the strain distributions of the $120\,\mathrm{g/m^2}$ neat, tailored and nano samples are minimal. A marginal reduction in strain concentration is observed in the vicinity of the hole, with modification, which hints at a reduced matrix damage occurrence. Further, several significant differences can be observed in the fracture patterns, as shown in Figure 3.15. The fracture shows less delamination and more fibre failure. This effect is evident in the microsection shown in Figure 3.16. Although the neat and tailored samples exhibit delamination failure, the nano samples show almost no evidence of delamination. However, the distribution of delamination failure in the neat and tailored samples varies slightly. The delamination is mainly present between the $\pm 45°$ plies. The fracture patterns of the $0°$ plies of the neat and tailored specimens indicate that the failure was influenced by the $45°$ plies. This trend can be observed in the relatively high strength values of the neat and tailored samples. However, the nano specimen was found to be more brittle than the neat and tailored specimens. Therefore, it can be concluded that the full FLG-modification leads to fibre failure dominated fracture. This also explains the relatively low ultimate strength of the nano specimen. However, the higher interlaminar strength of the nano specimen is not solely responsible for fibre failure being more dominant than delamination failure. Figure 3.18 shows the damage initiation stress, wherein an additional effect can be observed. The damage was initiated at a significantly higher stress than that of the neat and tailored specimen. This

increases the usable design range of the stress, thereby confirming that the FLG modification increases the transverse ply strength and resistance against shear matrix cracking.

Ply Thickness: $60\,\mathrm{g/m^2}$

The DIC images indicate no significant variation of stress distributions of specimens with $60\,\mathrm{g/m^2}$ and $30\,\mathrm{g/m^2}$ ply thickness, because the progressive damage is not visible on the mesoscale due to the inability of the 120 Hz frame rate in resolving the failure process, as a result they are not included in the comparison. In addition, the small scale of the fracture zone makes it difficult to evaluate the influence of FLG modification on the failure process of a sample having a ply thickness of $60\,\mathrm{g/m^2}$. Thus, the failure behaviours of the different configurations of these specimens are studied by using the micro-sections, as shown in Figure 3.16. The $60\,\mathrm{g/m^2}$ neat sample demonstrates a relatively smooth fracture edge with limited delamination. Apparent differences are visible between the damage morphologies of the tailored and neat specimens. The 90° ply of the tailored specimen is mostly attached to the 0° ply after the fracture. Severe delamination of the 45° ply is visible in the tailored specimen, unlike the neat specimen. This can be accounted to the higher ERR between the 0° adjacent plies, which leads to the formation of delaminations between the 45° plies. Further, the nano specimens exhibit an irregular fracture pattern. The micro-sections were analysed based on the image processing method presented in section 3.2.5, to examine the crack length, as shown in Figure 3.1. Figure 3.19 and Figure 3.20 depict the resulting crack representations and derived edge lengths, respectively. Figure 3.11 shows that the trend of the resulting fracture length is correlating with the strength. However, the increase in strength is limited, as shown in Figure 3.11. Nevertheless, the nano specimen was found to exhibit a significantly delayed damage initiation, which is similar to the behaviour of thick-ply laminates.

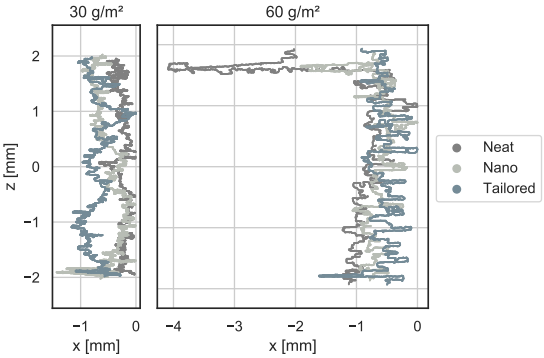

Figure 3.19.: Fracture paths determined from the microsections of the $30\,g/m^2$ and $60\,g/m^2$ samples

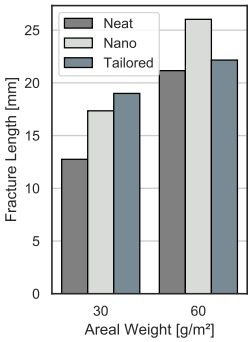

Figure 3.20.: Fracture paths lengths of the $30\,g/m^2$ and $60\,g/m^2$ samples

Ply Thickness: $30\,g/m^2$

The resulting ultimate strength of the neat $30\,g/m^2$ specimen is the lowest ultimate strength obtained (see Figure 3.11). However, the strength is increased for both FLG-modified configurations in this case. The variations in the damage morphology of the fractured edge are shown in the micro-sections in Figure 3.28 and in the derived fracture path in Figure 3.19. The matrix damage in specimens having a ply thickness of $30\,g/m^2$ is almost suppressed completely by the in-situ strength. This is indicated by the straight fracture edge of the neat specimen, as shown in the fracture path (Figure 3.20), the damage initiation stress (Figure 3.18) and the micro-section Figure (3.28). The neat $30\,g/m^2$ specimen's behaviour can explain the effect of the FLG modification in the $30\,g/m^2$ nano specimen. Due to the suppression of matrix damage by the in-situ effect, the neat specimen's final failure is fully localised, resulting in no damage progression before final failure. Because the stress concentration at the hole cannot be blunted by matrix damage, the failure is locally confined. In the nano specimen, local matrix damage forms at the FLG particles in the highly stressed region in the hole's vicinity, which consumes energy and relieves stress concentrations locally. Because the FLG particles are distributed throughout the laminate, they form distributed damage on a micro-scale around the stress concentration, as visible in Figure 3.19. This results in progressive damage growth on a small-scale before

ultimate failure, leading to an increment in ultimate strength. Consequently, the irregularity and length of the fracture edge increases, as shown in Figure 3.19 and Figure 3.20 leads to the assumption that the distributed localised matrix failure induced by the FLG can reduce the stress concentration and thus crack blunting.

Figure 3.21 summarises the effect of the FLG matrix modification on the ultimate OHT strength. For 240 g/m^2 only a modification of the 0° plies is beneficial. At 120 g/m^2 a modification of all plies leads to a reduction in ultimate strength because the dominant failure is changed from delamination to fibre-failure, as highlighted in Figure 3.21. For 30 g/m^2 the modification of the laminate is beneficially and increases the ultimate strength by 6 %.

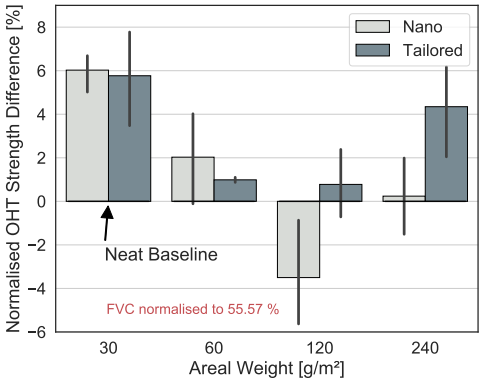

Figure 3.21.: Changes in the OHT strength of the tailored and nano specimens compared with those of the neat specimens

3.3.5. Compressive Strength

Few studies have investigated the impact of ply thickness on the compressive strength of quasi-isotropic layups. Yokozeki et al. [121] reported that the reduction of FAW from 145 g/m^2 to 75 g/m^2 led to an increment of 16 % in the strength. Amacher et al. observed that the increasing homogeneity of the microstructure with decreasing ply thickness led to a rise in the UD compressive strength [18].

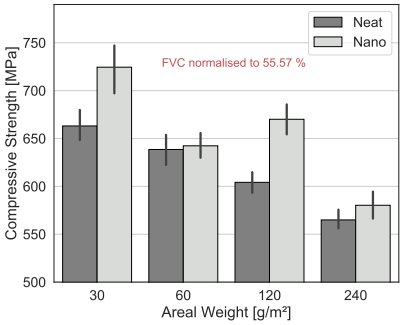

Figure 3.22.: Compressive strength of neat and nano specimen with different ply thicknesses

Figure 3.22 shows the compressive strength values for specimens with different ply thicknesses. Generally, the compressive strength increases for neat specimen with decreasing ply thickness. Figure 3.23 shows the variation of the compressive strength with respect to the $240\,\mathrm{g/m^2}$ specimen. A maximum increment of 17 % for the neat specimen is observed. The increasing trend of the compressive strength of QI-thin-ply laminates is attributed to several reasons. For instance, a reduction in the ply thickness leads to an increase in the bending stiffness of the laminate. An increasing number of fibres oriented in 0° are arranged at a larger distance from the mid-plane of the laminate. The higher bending stiffness consequently increases the global and local stability of the laminate. This effect counteracts the bending deformation and consequently, uneven loading, thereby minimising the probability of premature failure. Also, the thinner plies contribute to a higher layup uniformity due to the dispersion of layup-angle-deviations across several plies.

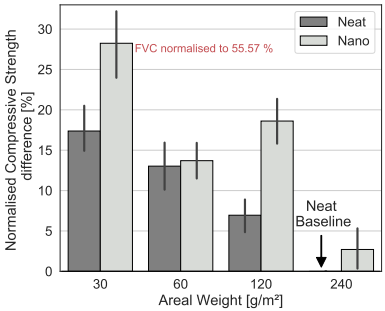

Figure 3.23.: Normalised change of the compressive strength with respect to the 240 g/m^2 neat specimen

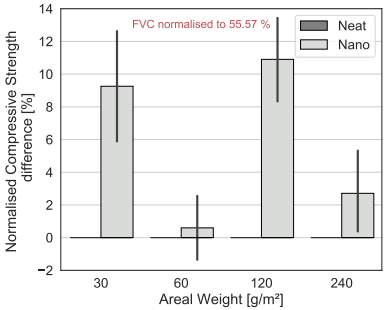

Figure 3.24.: Normalised change of the compressive strength with respect to the neat specimens having different ply thicknesses

The addition of FLG particles further improves the compressive strength, as shown in Figure 3.23. The strength values of the 30 g/m^2 nano specimens are 28 % higher than those of the 240 g/m^2 neat specimens. Similarly, the strength values of the 30 g/m^2 nano specimens are 9 % higher than those of the according neat specimens. Cho et al. [122] investigated the impact of FLG on the compressive strength of UD-CFRPs and reported strength increments of 10 % and 16 % for FLG matrix modifications of 3 wt. % and 5 wt. %, respectively. The rise in the compressive strength is caused by an enhancement of the in-plane shear properties due to the nanoparticles. Udin et al. [123] investigated the compressive strength of UD-GFRPs modified with 15 wt. % nano silica particles and reported an increment of 33 % of the compressive strength in the 5° off-axis compression tests. Using this, they calculated the 0° compressive strength which revealed a rise of 62 %. Chu et al. [115] demonstrated that the FLG particles are aligned tangentially to the fibres and provide better mechanical reinforcement than the FLG particles in conventional polymer-based nanocomposites due to the constrained environment between the fibres. Therefore, it can be concluded that the fibre support increases due to a rise in the local stiffness of a region consisting of FLG particles that are located next to a fibre.

However, the strength of the 60 g/m^2 nano samples was not greater than that of the neat specimens, as shown in Figure 3.25. Nevertheless, inhomogeneities are formed because the 60 g/m^2 nano samples are manufactured by ply blocking two 30 g/m^2 plies. There are several resin rich regions throughout the lami-

nate. These regions exist in the interfaces between the plies produced by ply blocking. The random superimposition of the deviations of the thickness of individual plies leads to the formation of local undulations. Although these two effects counteract FLG modification, they also highlight the positive impact of CNPs, as, despite the defects, the strength is only slightly affected.

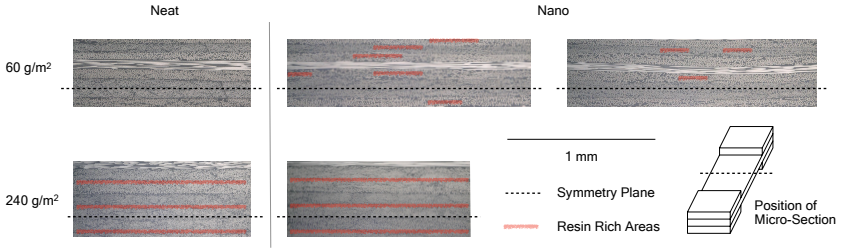

Figure 3.25.: Micro-sections of ply-level scaled compressive specimens with highlighted resin-rich regions

3.3.6. Impact Damage and Compressive Residual Strength

The damage resulting from an LVI depends, among others, on the layup, ply thickness and resin properties. The resulting residual strength depends mainly on the damage modes, damage size and position.

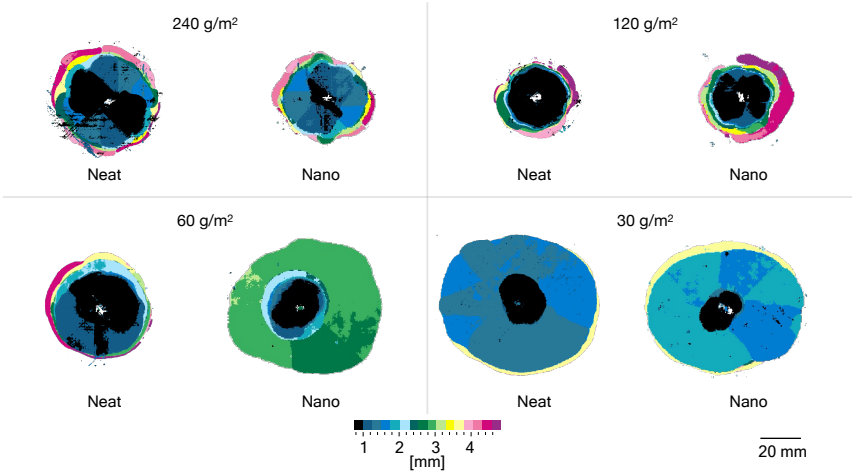

Figure 3.26.: Ultrasonic C-scans of the impact damage on to neat and nano specimens with ply thicknesses of 240 g/m^2, 120 g/m^2, 60 g/m^2 and 30 g/m^2

Figure 3.26 shows the representative ultrasonic C-scans of the depth of the defects for different ply thicknesses and modifications. The overall delamination of the 240 g/m^2 nano specimen is lesser than that of the neat specimen. The extent of delamination for the 120 g/m^2 specimens is generally lesser than that of the 240 g/m^2 specimens. However, the delamination distribution between the laminates of the neat and nano specimens is variable. The extent of the delamination of the nano specimen above the mid-plane is smaller while the delaminations in the lower interfaces increase in size. This effect is enhanced in 60 g/m^2 specimens, wherein extensive delamination is observed immediately below the mid-plane. This kind of delamination is recognisable for both configurations in 30 g/m^2 specimens.

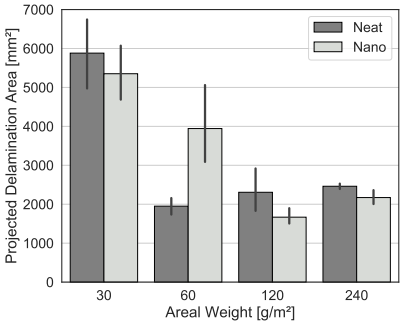

Figure 3.27.: Projected delamination area obtained by the ultrasonic C-scans

The projected delamination area, derived from the C-scans, is shown in Figure 3.27. The projected delamination area of the neat specimen decreases with reducing ply thickness, until the latter attains a value of $60\,\mathrm{g/m^2}$. The ultra-thin-ply thickness of the $30\,\mathrm{g/m^2}$ specimen causes its projected delamination size to almost triple. The nano specimens show relatively small projected delamination sizes for the $240\,\mathrm{g/m^2}$ and $120\,\mathrm{g/m^2}$ specimens as the interlaminar ERR of the nano specimen was considerably higher than that of the other specimens, thereby resulting in a reduction of the delamination size for the $240\,\mathrm{g/m^2}$ and $120\,\mathrm{g/m^2}$ specimens. This trend has been observed in other studies based on standard-ply thicknesses [119]. However, the projected delamination size of the $60\,\mathrm{g/m^2}$ specimen increases significantly, which was at first a surprising result, but can be explained by the changed damage behaviour due to the FLG particle modification.

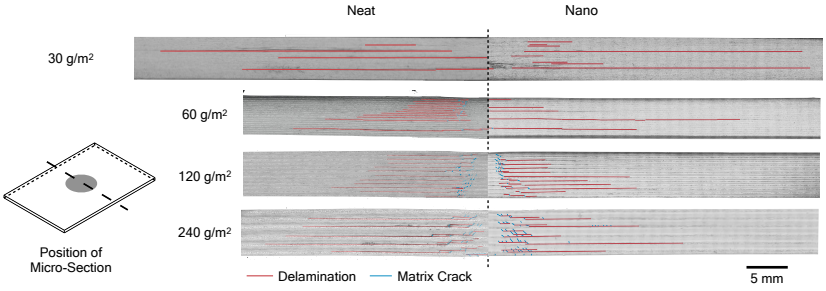

Figure 3.28.: Delamination damage and matrix cracks depicted in the micro-sections of the neat and nano specimens for different ply thicknesses

Micro-sections of the specimens were prepared to evaluate the delamination distribution across the thickness of the plies of the laminates. The micro-sections depicting the matrix cracks and delamination regions for specimens with different ply thicknesses and configurations are shown in Figure 3.28. The changes in the delamination distribution of the specimen with a ply thickness of $240\,g/m^2$ is visible in the C-scan. The higher mode II ERR of the nano specimen reduces the size of the delamination uniformly. Additionally, the significantly lower crack opening indicates a reduction in matrix damage due to the FLG modification. The $120\,g/m^2$ samples have more delaminations than the $240\,g/m^2$ because the former has more interfaces than the latter. The nano specimens displayed a reduction in delamination size in the upper half of the laminate. A change in the ply thickness from $120\,g/m^2$ to $60\,g/m^2$ entirely changes the damage morphology. The neat specimen shows delaminations initiated by matrix damage originating from the high shear loads during the impact (see Figure 3.28), in every QI-sub-laminate in the upper half of the laminate. However, in the lower half, matrix damage formation through tensile loads is suppressed by the higher transverse strength due to the in-situ effect. Therefore, no delaminations can be initiated at the matrix cracks. In this case, the delamination is initiated by exceeding the interlaminar shear strength. The FLG modification suppresses the formation of matrix damage in the whole nano specimen, thereby reducing the number of delaminations. The nano modification causes the damage morphology of the $60\,g/m^2$ specimen to be similar to that of the $30\,g/m^2$ specimen. This explains the surprising result obtained previously from the C-scans. The in-situ effect also suppresses the matrix cracks in the $30\,g/m^2$ neat specimen. Thus, the differences between the damage morphologies of the neat and nano specimens are minimal, which is responsible for the minimal reduction of the projected delamination area (see Figure 3.27). The delamination area is also calculated by using the microsections. These calculations are made on the assumption that the delaminations are circular. Although this assumption is especially valid for thin plies, it provides a useful reference for relatively thicker plies because the comparison takes place in the same cutting plane. Figure 3.29 displays the calculated results.

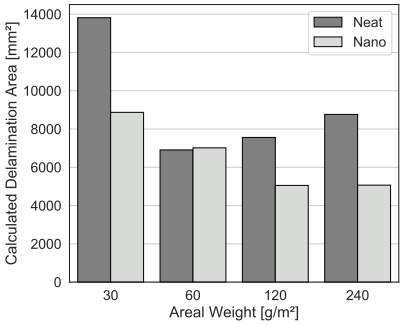

Figure 3.29.: Delamination area calculated from the microsections

The results highlight, that the effect of the FLG modification on the resulting delamination area is greater than visible from the projected delamination areas (compare 3.27). FLG modification reduces the delamination area significantly for all ply thicknesses except for $60\,g/m^2$, here the suppression of the matrix damage leads to a complete delamination-dominated damage. The permanent deformation measurements confirm the findings of the micro-sections. Figure 3.30 displays the permanent indentation depth and bulge on the impacted and non-impacted sides, respectively. The permanent indentation depths are below the visibility limit, which is often set at 0.5 mm [124]. The FLG-modified configurations displayed reduced permanent deformations due to a reduction in matrix damage, fewer delamination interfaces and reduced crack opening.

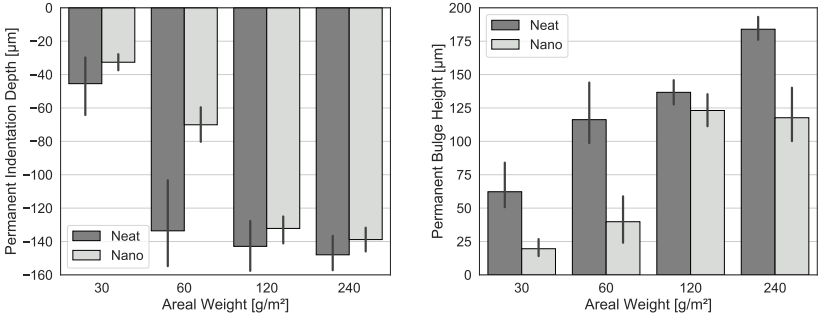

a) b)

Figure 3.30.: a) Permanent indentation depth on the impacted side and b) permanent bulge on the non-impacted side

The values of the compressive residual strength shown in Figure 3.31 are inconclusive because there is no clear trend in the influence of the ply thickness or matrix modification on the residual strength.

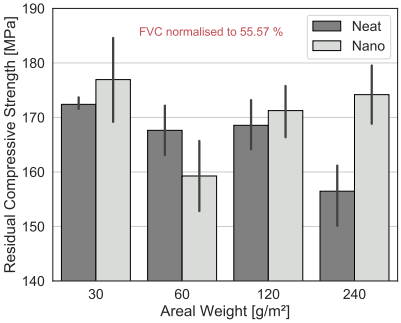

Figure 3.31.: Residual compressive strength after impact of neat and nano specimens with different ply thicknesses

The CAI strength of the neat configurations increases with decreasing ply thickness. The lower delamination area for specimens with ply thicknesses $>30\,\mathrm{g/m^2}$, both measured and projected, provides a relatively high local buckling stability and residual strength. The delamination area for the $30\,\mathrm{g/m^2}$ specimens is larger than those of the other configurations. However, the CAI strength of these specimens is the highest, despite the substantial delamination size. This behaviour can be attributed to two effects. The compressive strength increases with decreasing ply thickness, as shown in Figure 3.22. In addition, the delaminations of the $30\,\mathrm{g/m^2}$ laminate have sub-laminates with a relatively large number of plies between the delaminations. This increases the sub-laminate bending stiffness, thereby resulting in increased resistance against buckling. Secondly, the length of the delamination increases, whilst lowering the resistance against buckling. The projected delamination area is usually one of the main assessment factors in determining the severity of the damage in comparison to the residual compressive strength. However, this correlation cannot be defined without accounting for the ply thickness. Figure 3.32 shows the retention factors affecting the undamaged compressive strength.

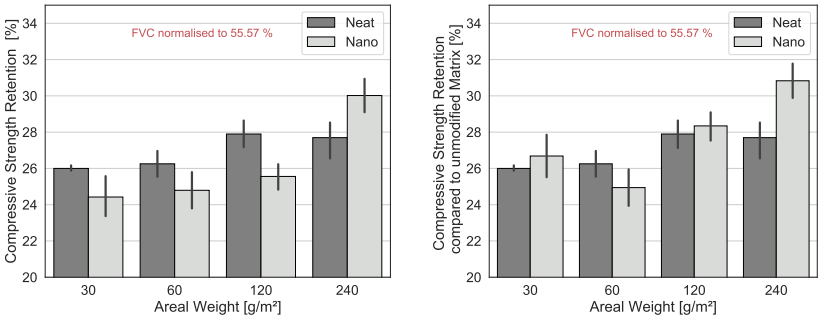

a) b)

Figure 3.32.: a) Strength retention after impact and b) normalised with respect to the neat compressive strength

The thin-ply laminates have lower retention than thick-ply laminates due to the former's relatively high non-damaged compressive strength. The advantage of a relatively high residual strength is evident from Figure 3.33, which shows the retention of the specimen in comparison to the $240\,\mathrm{g/m^2}$ configuration. The analysis of the nano specimen is straightforward as with the neat specimen because the occurring damage is substantially modified. The decreased matrix damage and delamination extent of a specimen with a thickness of $240\,\mathrm{g/m^2}$ result in a substantial rise in the residual compressive strength. Thus, the CAI performance of the $240\,\mathrm{g/m^2}$ specimen is comparable to that of a specimen with a laminate thickness of $30\,\mathrm{g/m^2}$.

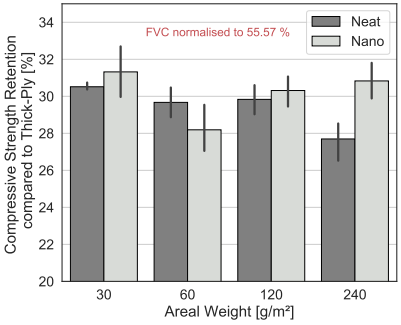

Figure 3.33.: Strength retention in comparison to the compressive strength of the $240\,\mathrm{g/m^2}$ neat specimen

This rise in the CAI strength due to nanoparticle modification is consistent with the results obtained from other studies. Kostopoulos et al. [93] reported an increment of approximately 16 % in the CAI strength of a composite with 160 g/m^2 with the addition of 0.5 wt. % FLG into the matrix. Mannov et al. [94] analysed the impact of the addition of 0.3 wt. % FLGs to the matrix of CFRPs. The cross-ply laminates, with a ply thickness of 0.75 mm, displayed a rise of 19 % in the CAI strength. The influence of CNPs in conjunction with the ply thicknesses of laminates has not yet been studied. The rise in the residual strength of the 120 g/m^2 specimen is limited, despite the relatively low projected delamination area. This is because the critical delaminations in the mid-plane are nearly identical in size and thus, limit the rise in the strength [125, 126]. Nano particle modification has a negative effect in the 60 g/m^2 specimen, i.e., the residual strength of this specimen is lower than those of specimens with different ply thicknesses. This is attributed to the changes in the delamination distribution. However, the nano specimen has intact sub-laminates with several plies between the delaminations. This sub-laminate bending stiffness of the laminates made from thin plies is greater than that of the laminates made from thicker plies, thereby enhancing the resistance of the thin-ply laminates against buckling. However, the rise in the length of the delaminations lowers the laminate's resistance against buckling. Despite having a higher bending stiffness than laminates with relatively thicker plies, the specimens with thin plies cannot counteract the large delamination size. Therefore, the compressive residual strength is decreased. The difference between the delamination distribution and size of the neat and nano specimens at 30 g/m^2 is limited, as visible in the C-scans (see Figure 3.26 and Figure 3.27) and in the micro-sections (see figure Figure 3.28 and Figure 3.29). Therefore, both specimens have similar residual strengths.

An analytical mechanical model is developed to verify that the changes in the residual compressive strength of the 60 g/m^2 specimens are caused by changes in the delamination distribution and size. Several studies have evaluated the influence of delaminations on the residual compressive strength by introducing artificial delaminations [127, 128]. Short et al. [129] reported the existence of two buckling modes, namely a local mode and a global one. In the local mode, the sub-laminate above the delamination buckled out-of-plane. The global mode described that both sub-laminates above and below the delamination in the global mode buckled out-of-plane. Therefore, delaminations are more critical when they are close to the laminate mid-plane. The relatively simple failure of thin-

ply composites due to an LVI, as shown in Figure 3.28, makes them suitable for buckling analysis. Figure 3.34 summarises the modelling approach. The delaminations in the laminate are assumed to be circular. This assumption seems to be reasonable, according to Figure 3.26. The reason behind the circular shape of the delamination is the practical isotropy of the delaminated sub-laminates. Subsequently, the delaminated sub-laminates are approximated with a circumferential square. A buckling analysis of the sub-laminate is performed based on this square. This analysis is performed for every critical delamination.

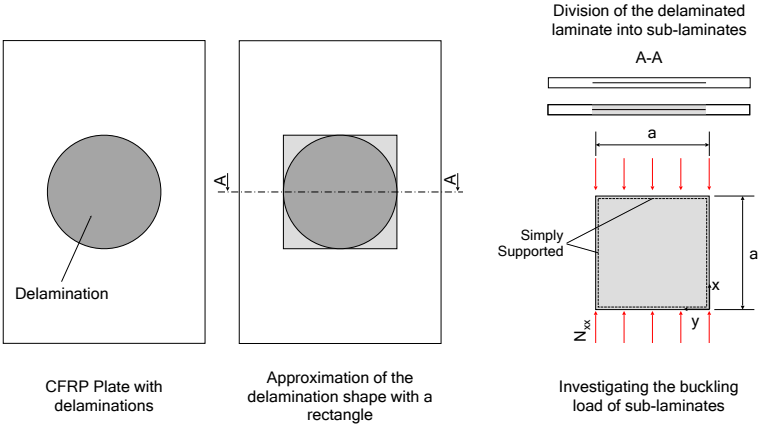

Figure 3.34.: Scheme of the buckling analysis to determine the critical buckling load of delaminated sub-laminates

The plate is subjected to uniaxial compression and simply supported on all edges. The minimal buckling load is calculated according to the following equation:

$$N_{xx} = \pi^2 \left[D_{11} \frac{m^2}{a^2} + \frac{2}{a^2}(D_{12} + 2D_{66}) + D_{22} \frac{1}{a^2 m^2} \right] \tag{3.1}$$

where N_{xx} is the buckling load, a is the edge length of the square, D_{12}, D_{22} and D_{66} are the entries obtained from the bending stiffness matrix of the classical laminate theory, and m is the unknown half-wave number that is calculated as shown below.

$$m = \sqrt[4]{\frac{D_{22}}{D_{11}}} \tag{3.2}$$

The results obtained from Equation 3.2 are rounded up and down to the nearest integers. Equation 3.1 is then evaluated for both values. The lower value refers to the critical load at which the sub-laminate undergoes buckling and potentially initiates global failure. Since delaminated sub-laminates are usually asymmetric, N_{xx} can lead to warping and twisting at the critical buckling load. However, other studies have demonstrated that the behaviour of asymmetrical laminates falls within the scope of a linear buckling analysis [130, 131]. The thickness of the sub-laminates t_{sub} is used to obtain the residual compressive strength of the laminate, as shown below.

$$\sigma_{\mathrm{res}} = \frac{N_{\mathrm{xx}}}{t_{\mathrm{sub}}} \tag{3.3}$$

The cross-section of the $60\,\mathrm{g/m^2}$ ply thickness is shown in Figure 3.35. The critical delaminations are chosen according to the criteria proposed by Short et al. [129]. They are represented by light and dark grey colours in the neat specimen and light grey in the nano specimen.

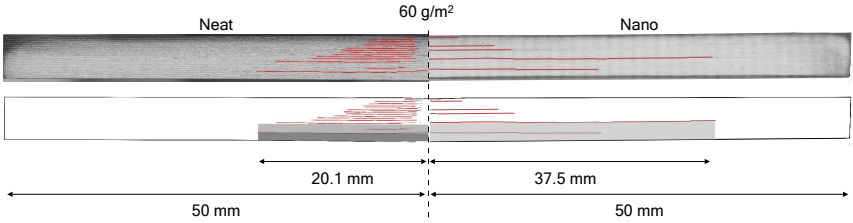

Figure 3.35.: Micro-section of the $60\,\mathrm{g/m^2}$ neat and nano specimens with marked delaminations (upper) and sub-laminates (lower)

The neat specimen has a delamination radius of $r = 20.1\,\mathrm{mm}$ and a ply thickness of $t_{\mathrm{ply}} = 0.0058\,mm$. The critical delaminated sub-laminate has a $[45/90/-45/0]_6$ layup, which results in a buckling stress of 172 MPa. The modified specimen has a delamination radius of $r = 37.5\,\mathrm{mm}$ and a ply thickness of $t_{\mathrm{ply}} = 0.0060\,mm$. The delaminated sub-laminate has a
$[[45/90/-45]_{10}/45/90/-45]$ layup, which results in a buckling stress of
159 MPa. These results show that the reduction in the residual strength is mainly due to the changes in the delamination size and distribution. A comparison between the results of the proposed analytical model and average test results indicates that the changes in both cases are very similar. The model reported a

strength reduction of 5.6 %, which is an excellent agreement with the reduction observed in the experimental tests of 5.3 %.

3.4. Conclusion

This chapter investigated the impact of a CNP modification on the CFRP's damage tolerance with varying ply thicknesses. Recalling the working hypothesis of this chapter:

The addition of CNPs into the matrix introduces additional energy-consuming damage mechanisms into the composite and leads to crack blunting at stress concentrations due to the formation of dispersed local damage. The effect of the CNP modification depends on the ply thickness, as it controls the stress state in the laminate.

The results from the interlaminar ERR satisfy the first part of the working hypothesis, because the addition of FLG 0.05 wt. % into the matrix introduces additional damage modes, resulting in a considerable improvement of the interlaminar ERR by 23 % under mode I and 35 % under mode II. FLGs, therefore, pose an efficient toughening modification for composites.

For laminates subjected to complex load cases, the picture is not comprehensive because the impact of the FLG modification on the composite must be judged together with the ply thickness. In notched laminates, the FLG modification increases the damage initiation stress for all ply thicknesses, hence increasing the design space and, therefore, the damage tolerance. The ultimate strength for ply thicknesses $\geq 120\,g/m^2$ is lower when all plies utilise modified prepreg because the modification suppresses the delamination formation. This suppression of delamination is achieved by the later initiation of matrix cracking and the higher ERR. However, overall the positive effect still overrules the reduced ultimate strength. The matrix modification prevents severe delamination of the sample and thus increases the structural integrity and the usable stress levels. Ultra-thin laminates confirm the research hypothesis that micro-cracks at the particles form before ultimate failure, which leads to local crack blunting and thereby reduces the stress concentration in resulting in a higher ultimate OHT strength. Tailored modification of the plies oriented in load direction highlights the effect of an FLG modification on the load oriented ply as it prevents premature delamination of the modified ply and shifts the occurring delaminations towards the 45° plies.

The strength for $240\,g/m^2$ increases as delamination suppression leads to a higher load share on the 45° plies, before ultimate failure.

Under LVI loading, both the reduction of ply thickness and the addition of FLG leads to a reduction in intralaminar matrix damage and reduces the number of delaminations as a result of FLG. For thick-ply laminates, these effects lead to a significant increase in residual compressive strength. However, when the matrix damage is almost entirely suppressed, delaminations are initiated by exceeding the interlaminar shear strength and not at the matrix cracks. As a result, only a few large delaminations form at or close to the laminate's mid-plane. Ultra-thin-ply laminate shows this behaviour just by the in-situ effect, and thus the FLG-modification does not significantly influence this behaviour. However, at $60\,g/m^2$, the FLG modification changes the behaviour from a combination of matrix damage and delamination to a delamination-dominated failure, reducing the residual compressive strength. At $30\,g/m^2$ and $120\,g/m^2$ the modification has a limited effect. However, at $60\,g/m^2$, the addition of FLG leads to reduced residual compressive strength resulting from the formation of a large mid-plane delamination.

Both the reduction of the ply thickness and the modification of the matrix increases the compressive strength significantly. The reduction of the ply thickness from $240\,g/m^2$ and $30\,g/m^2$ raises the compressive strength by 17 %, and with modification increases to 28 %.

This chapter has shown that modification of the matrix with CNP can significantly improve CFRPs' performance and consequently increase damage tolerance. Further investigations could improve the damage tolerance. A promising approach could investigate a tailored modification of impact loaded laminates using modified plies near the symmetry plane. This distribution of modified plies could adapt the delamination distribution to reach higher residual strengths. It could also be promising to investigate a tailored modification of impact loaded laminates using modified plies near the symmetry line to adapt the delamination behaviour, thus increasing residual compressive strength. Additional investigation concerning the optimal filler content and particle sizes in the composite may yield further improvements and should be considered.

4. Bio-Inspired Helicoidal Laminates

The interaction between the layup and ply thickness has a decisive influence on the failure behaviour [18, 60, 132, 133], as demonstrated in Chapter 3. A relatively new approach to control the damage behaviour of FRPs is the use of advanced layup designs inspired by nature. A promising attempt are helicoidal laminates structures found in impact-loaded body parts of some animals called Bouligand structures. Bouligand [22] described in the early 1970's twisted fibre structures in highly impact stressed body parts of insects, beetles or spiders. Figure 4.1 shows a laminate structure referred to as Bouligand structure. Bouligand structures are laminated structures with very small fibre difference angles or pitch angles that result in rotating fibre angles along the thickness direction and form a helicoidal shaped layup. A Bouligand unit denotes a substructure with a total rotation of 180°. A prominent user of Bouligand structures is the mantis shrimp, displayed in Figure 4.2.

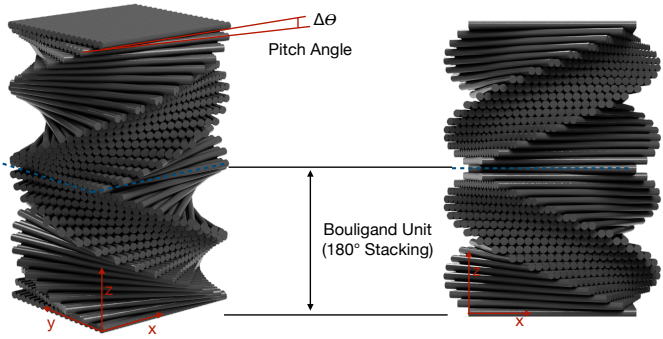

Figure 4.1.: Schematic representation of a symmetrical Bouligand layup consisting of two Bouligand units with a pitch angle θ of 10°

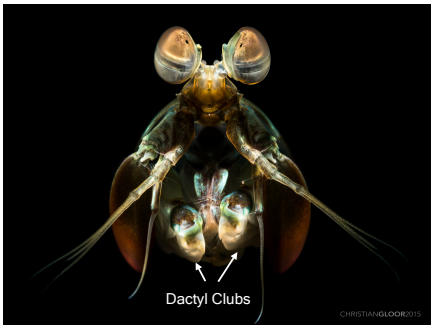

Figure 4.2.: Magnified view of mantis shrimp (The arrows denote the location of the dactyl club's impact surface) [134]

It has small dactyl clubs, which it uses as a biological hammer to smash marine organisms' shells or carapaces. Accelerations of approximately 10.400 g lead to velocities up to 23 m/s achieved from a stationary position [135]. The clubs exhibit an impressive set of characteristics adapted for surviving high-velocity impacts [136]. Despite the high loads, the dactyl clubs are extremely damage tolerant as they can withstand thousands of hits before being replaced during periodic moulting [23]. A cross-sectional analysis of the club by Weaver et al. [23] divides it in three distinct structural domains as shown in Figure 4.3.

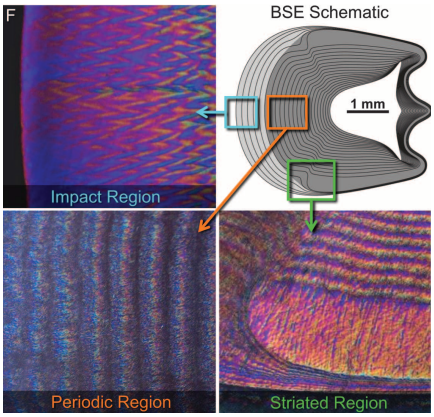

Figure 4.3.: Optical micrographs from Weaver et al. [23], revealing the buckled rotated plywood structural motif of the impact region, the Bouligand structure of the periodic region and the thickened circumferential band with parallel chitin fibres in the striated region

The so-called periodic region is similar to a Bouligand structure with several sequential Bouligand units. The pitch angle in the periodic region of the dactyl clubs varies and is approximated by Grunenfelder et al. [137] between the plies in the outer region with 1.6° and in the inner region with 6.2°. The impact energy is dissipated by twisting matrix cracks development, resulting in excellent damage tolerance properties of this structure. Small pitch angles significantly reduce the formation of critical failure mechanisms such as delaminations due to low interlaminar shear stresses [23]. The derived working hypothesis of this chapter is:

The composite's layup controls the occurring matrix damage modes. Thin-ply, bio-inspired helicoidal layups enable delamination-free composites.

This chapter aims to realise laminates with progressive sub-critical, thus delamination-free, matrix damage formation during in-plane and out-of-plane loading.

4.1. State of the Art

Figure 4.1 displays a symmetrical Bouligand laminate structure consisting of two Bouligand units. It is a UD-laminate structure which features a very small fibre angle difference or pitch angle and therefore a rotating helicoidal fibre angle in the thickness direction. The realisation of truly nature-like Bouligand structure is only possible since the development of "thin-ply" laminates.
Very promising results for out-of-plane loads have been realised in previous studies. Mencattelli et al. [133] observed in their parameter study on different ply pitch angles for linear Bouligand structures a continuous improvement of the compression after impact strength with decreasing pitch angle. Reducing the pitch angle from 45° to 2.5° leads to a reduction of 29 % in the projected damage area while retaining a similar CAI strength, despite a considerably reduced number of 0° plies. The main damage mechanism in Bouligand laminates are twisting matrix cracks. Small pitch angles significantly reduce the formation of critical failure mechanisms such as delaminations due to reduced interlaminar shear stresses. At the same time, crack growth in thickness direction is no longer limited by the surrounding plies. Matrix cracks propagate in the thickness direction, since the low interlaminar shear stress prevents crack deflection into the interlaminar boundary ply. By crack deflection and continuous change

of the fracture plane in thickness direction, the crack path is extended and the energy dissipation during crack growth is increased [133, 138, 139]. The result is diffused, sub-critical helicoidal matrix damage. This sub-critical impact damage leads [137, 138] to a significant increase in compressive residual strength of up to 8 % compared to 45° pitch angle laminates [140].

In this thesis, further investigations to understand the impact and residual strength characteristic of CFRP Bouligand structures are conducted. A CFRP Bouligand structures with a pitch angle of 2.07° is tested, which is the lowest realised pitch angle so far and thus closest to the one found in nature. The FLG-modified prepreg, introduced in Chapter 3, is also investigated, to determine the influence of the fracture toughness of the matrix on damage development, in order to determine whether a higher toughness has a beneficial impact on the damage behaviour. In addition to out-of-plane loading and the resulting residual strength, the in-plane tensile performance of CFRP Bouligand structures is investigated. In classical 45° pitch angle laminates with sufficiently thick plies delamination is the predominant failure mechanism. In thin-ply laminates, the dominant failure mode changes to fibre failure [13, 18]. As a result, the static tensile strength of notched thin-ply composites is decreased, because the lack of stress relaxation through damage leads to a higher stress concentration and premature failure compared to thick-ply laminates. In order to increase the notched strength and the failure properties of laminates, different studies investigated new layup designs with smaller angles than 45° and displayed their potential. Wu et al. [141] demonstrated pseudo-ductile tensile stress-strain behaviour in unnotched thin-ply $[\pm 25_2/0]s$ laminates, where the 0° plies are high-modulus fibres while the 25° plies are made up of intermediate modulus fibres. Central 0° ply fragmentation and dispersed delaminations have been identified as the main damage mechanisms. These damage mechanisms can also relieve the stress concentration in notched laminates, resulting in an enhanced notched strength and consequently reduced notch-sensitivity [141]. Bouligand laminates can potentially offer a similar damage mechanism. However, when the fracture strain of the 0° ply is reached the load is transferred onto the neighbouring plies. Due to the low fibre angle deviation and thin 0° ply the neighbouring plies are able to take this load. However, the ply strength in load direction is decreasing with increasing fibre angle, and thus a significantly lower fracture strength can be expected with a QI Bouligand layup compared to Wu's layup. Due to the low pitch angle and the resulting low interlaminar stresses, delaminations are un-

likely, and thus matrix fracture and fibre failure are potentially the only offered failure mechanisms. This and the additional load path due to multiple fibre angles make the approach interesting for notched laminates. Apichattrabrut et al. [142] performed tensile tests on unnotched thick-ply symmetrical helicoidal laminates with a pitch angle of 10°, resulting in laminates with a thickness of 6.35 mm. Starting from the edges, the twisting cracks are propagating in a double helicoidal formed fracture plane through the thickness of the laminate, while no delamination occurs. Fibre failure is widely dispersed. Additionally the bending properties of thin-ply helicoidal laminates are evaluated. Due to their low pitch angle, they display a significant anisotropy in bending stiffness and strength. Cheng et. al [143] investigated the bending performance of thick-ply glass-fibre-epoxy Bouligand structures with a pitch angle of 16.4° and found a similar flexible strength, but strongly increased residual strength after first damage initiation.

4.2. Materials and Experimental Setup

The laminates were manufactured from NTPT thin-ply prepreg with Toray S700SC-12K-60E fibres and NTPT Thinpreg 402 matrix with and without FLG modification. The material had an areal weight of $30\,\mathrm{g/m^2}$ which results in a cured ply thickness of approx. $29\,\mu$m (see Table 4.1). Figure 4.1 displays a representative mid-plane symmetric Bouligand structure as used in the present study, with a pitch angle of $\theta = 10°$ consisting of two Bouligand units. An odd number of plies was used to obtain a centre-symmetrical laminate with a constant ply thickness in the mid-plane. The pitch angle θ of an QI-layup can be calculated by:

$$\theta = \frac{360}{n-1} \tag{4.1}$$

where n is the total number of plies. The angle a_i of a certain ply i is determined by Equation 4.2 with the pitch angle θ and total number of plies n:

$$a_i = \begin{cases} \theta \cdot (i-1) & 0 \leq i < \frac{n+1}{2} \\ 360 - \theta \cdot (i-1) & \frac{n+1}{2} < i \leq n \end{cases} \tag{4.2}$$

The different layups used are summarised in Table 4.1. $\bar{a}_i$ denotes the ply in the symmetry plane which is therefore half the thickness in this representation.

Table 4.1.: Overview of the configurations considered, layup, resulting pitch angle and specimen thickness

Configuration	Layup	Pitch Angle θ	Number of CFRP Plies n	Nominal Thickness [mm]
UNT (Neat) OHT (Neat/Nano) Bending (Neat)	$[a_1/a_2/\ldots/\bar{a}_i]_S$ *with* $i = \frac{n+1}{2} = 64$	2.586	127	3.683
CAI/Comp (Neat/Nano)	$[a_1/a_2/\ldots/\bar{a}_i]_S$ *with* $i = \frac{n+1}{2} = 88$	2.069	175	5.075
Bending (Neat) Comparison	$[45°/90°/-45°/0°]_{22s}$	45	176	5.14

For the layup of the UNT/OHT specimens, the 0° fibre direction is chosen as an initial fibre angle to have the maximum amount of 0° in the load direction. The resulting layup is displayed in Table 4.1. Additionally to the neat matrix a FLG modified resin was also investigated. Specimens with the unmodified matrix are referred to as "neat" and with FLG-modified resin to as "nano" in the following. The three-point Bouligand bending specimens were manufactured using the same layup (see Table 4.1). The comparative 45°-QI specimen's layup is also shown in Table 4.1

For the compression specimen and the impact/compression after impact specimen neat and nano configurations were tested. The thickness was chosen comparable to thin-ply 45°-QI layup investigated in Chapter 3. Table 4.2 shows the tested number of specimens per configuration and test.

Table 4.2.: Number of tested specimens per configuration

	Tension	Open-Hole Tension	Impact / CAI	Compression	Bending
No. Specimens	Neat: 8	Neat: 6 Nano: 3	Neat: 4/3 Nano: 4/3	Neat: 3 Nano: 3	Neat: 4 45°-QI: 4

4.3. Results and Discussion

4.3.1. Unnotched Tension

Figure 4.4 displays a representative micro-section of a tensile specimen. Due to the low pitch angle of 2.59° it is difficult to distinguish between the different plies. Additionally, the laminate quality and consistency is visible.

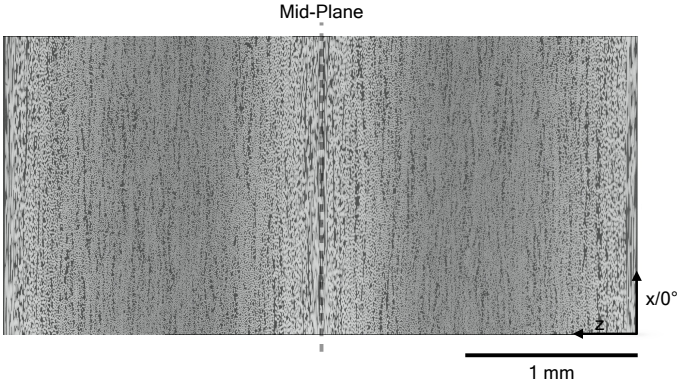

Figure 4.4.: Micro-section of a representative tensile specimen

Figure 4.5 displays the structural response of the UNT specimens and the respective mechanical properties are summarised in Table 4.3. The structural response is linear until a strain of 0.4 %. Figure 4.6 displays the stress strain curve of a representative tensile specimen in conjunction with the corresponding acoustic accumulated energy curve, derived from the AE measurements. With the beginning non-linearity the energy starts to increase significantly at a strain of 0.4 % with a flat parabolic characteristic until fracture, which results in a damage onset stress of 175.79 MPa. The damage onset stress in Table 4.3 is determined where the curve of accumulated energy begins to rise continuously.
The well known characteristic "knee" in the stress-strain behaviour of an FRP cross-ply laminate cannot be observed in the stress-strain behaviour. Hence, a seemingly continuous reduction in stiffness can be observed.

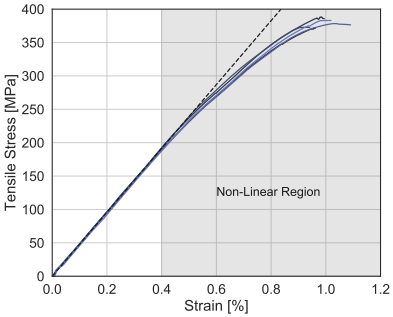

Figure 4.5.: Tensile stress-strain curves of the unnotched specimens (The grey area marks the non-linear response, which is defined by the AE damage initiation)

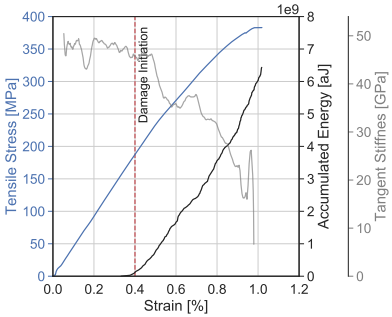

Figure 4.6.: Representative stress-strain curve of an unnotched specimen with the according accumulated energy from AE measurements

Table 4.3.: Tensile properties of the UNT specimens

	$\sigma_{\mathrm{UNT}}^{\mathrm{onset}}$ [MPa]	$\sigma_{\mathrm{UNT}}^{\mathrm{max}}$ [MPa]	E_{UNT} [GPa]
UNT Neat	175.79 ± 12.39	382.76 ± 7.39	47.84 ± 0.72

The radiographs at different load levels, displayed in Figure 4.7, show the crack development from the edges and continuous crack growth microscopically perpendicular to loading direction. This is causing the continuous stiffness reduction, observed in the stress-strain curve in Figure 4.5. The crack growth progresses in a micro-zig-zag pattern, which indicates crack growth in differently oriented plies. The crack density increases with higher loads. However, in contrast to cross-ply or 45°-QI thick-ply laminates [144, 145], the matrix cracks are not forming over the full width of the specimen. They form at the edge, grow into the laminate, but only up to a certain length. Cracks are initiated in the 90° ply and due to the occurring strain discontinuity damage is initiated at the same place in a different ply, but does not grow as the crack resistance of plies angled with smaller angles than 90° is too high. Only just before failure at 97.6 %, white areas occur on the X-ray which could be mistaken for delaminations, however

they mark opening helicoidal matrix cracks, which are also visible after failure, see Figure 4.9.

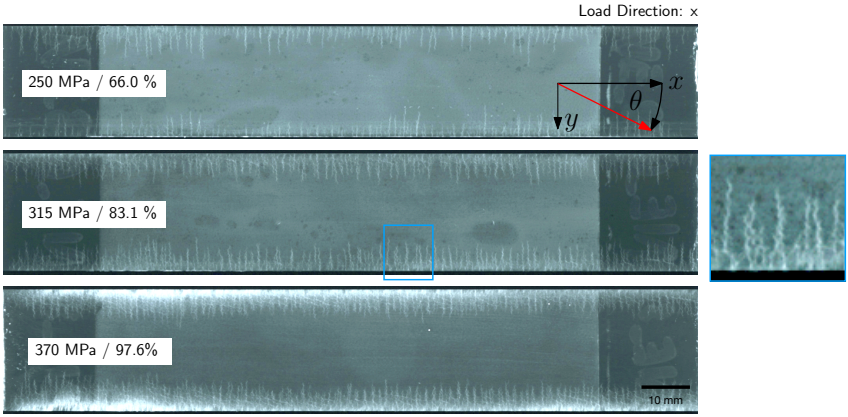

Figure 4.7.: Radiographs of an exemplary UNT specimen at increasing load levels

Damage is increasing continuously, as the AE measurements show (see Figure 4.6). The damage development does not occur suddenly, which is why there is a steady reduction in longitudinal stiffness and thus a flattening of the stress-strain curve. On closer inspection of the curve, it is noticeable that it is not decreasing with a consistent rate. Figure 4.6 shows a typical stress-strain curve and a tangent modulus in the strain range of 0.07 to 0.93 %. The tangent modulus is averaged over five data points and shows that the stiffness increases temporarily during the test, which can be accounted to fibre rotation. As matrix cracking occurs, fibres are able to slightly rotate into longitudinal direction and thus stiffening the structure. The observed zig-zag pattern on the X-ray images shows shear cracking due to fibre rotation, indicating fibre rotation at the edge region of the specimens. The shear crack angle fluctuation shows the participation of many plies in crack propagation over the thickness. Calculation of the updated fibre angle θ' as a result of fibre rotation can be done by Equation 4.3 according to [146]:

$$\theta' = arctan\left(\frac{tan(\theta + \varepsilon_y)}{1 + \varepsilon_x}\right) \tag{4.3}$$

This equation states a rotation of the fibre angle in load direction for longitudinal positive strains ε_x and negative transverse strains ε_y. Figure 4.8 shows that this is the case in regions at the edges of the specimen.

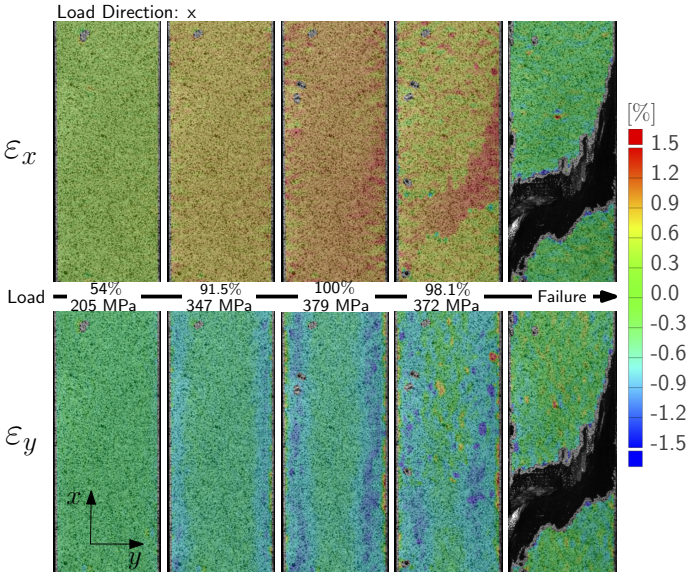

Figure 4.8.: Strain distribution in tensile ε_x and transverse ε_y direction at increasing load levels

The non-linear stress-strain response results consequently on the one hand from matrix cracking, which reduces the tangent modulus and on the other hand from fibre rotation, which is increasing the tangent modulus. These two effects interfere and thus lead to a non-monotonically declining tangent modulus.

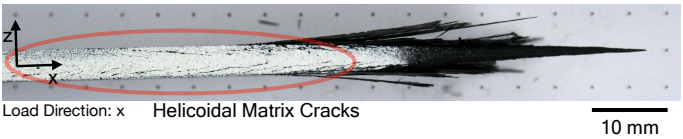

Figure 4.9.: Matrix cracks occurring in a rotating, helicoidal pattern at an even distance

The fractured specimen of a representative UNT Bouligand specimen is shown in Figure 4.10. The shape of matrix failure is helicoidal and is following the ply rotation.

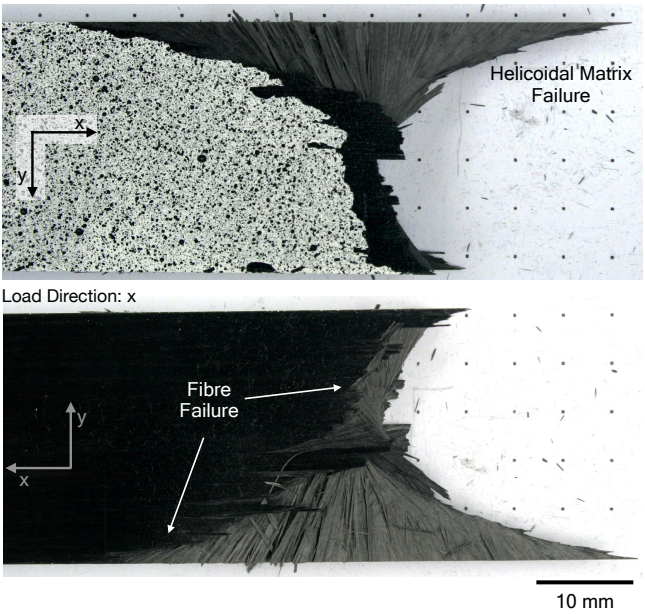

Figure 4.10.: Helicoidal shaped matrix failure and distributed fibre fracture of a UNT specimen

The fibre failure of the middle 0° and neighbouring plies is also exhibiting a helicoidal shape which is determined by the direction of fibre rotation. Fibre failure is initiated in the 0° ply and then propagates in the direction of the underlying fibre direction and thus turning with the pitch angle. The order of damage can be determined by the radiographs and DIC pictures, see Figure 4.7 and Figure 4.8, respectively. Matrix cracks begin to open, these cracks cause the bright shadow to appear on the radiographs. This leads to excessive stress in the middle plies and finally to fibre breakage of the 0° ply in the middle. Subsequently, the laminate shows brittle failure in the outer sections. The brittle fracture is marked in red in Figure 4.11. This failure sequence is also visible in the ε_x strain plot shown in Figure 4.8. The image taken after ultimate load shows a local strain increase in the fracture zone by mid-section failure shortly before failure of the outer laminate sections occurs. The failure progression is not fully comparable to the pseudo-plastic failure observed by Fuller et al. [146] and Wu [141], as global strain to failure is significantly lower. This was to be expected

due to the QI-laminate design. Nevertheless, some of the specimens exhibit a horizontal stress-strain curve before failure, see Figure 4.5, which indicates a similar effect to pseudo plasticity behaviour before failure. Figure 4.11 shows a localised failure region. However, a cascading effect is visible. The underlying fibre rotation causes that on one half of the specimen the fibre failure does not follow the matrix cracks. But fibre failure is not purely brittle, as the fibre presumably fails in the 0° ply first, then in the 2.58° ply and so on until final failure is reached. This results in non localised failure, which is also reflected in the low standard deviation of the strength (see Table 4.3).

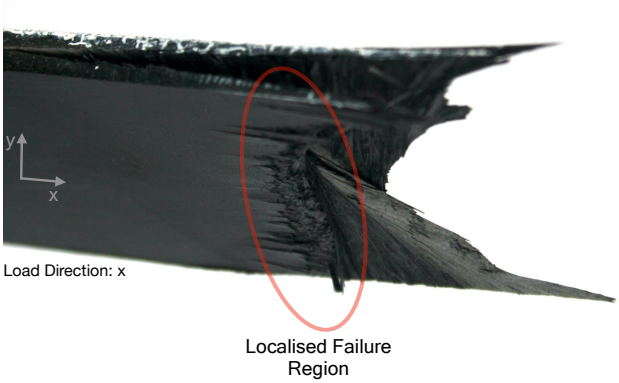

Figure 4.11.: Localised fibre fracture distribution of a UNT specimen

Figure 4.12 qualitatively summarises the occurring damage modes and sequence during tensile loading of QI-45° thick-ply, QI-45° thin-ply and Bouligand thin-ply composites (comparative data from Chapter 3). The general behaviour can be described as follows: For thick-ply composites, matrix cracking is the first occurring damage mode, however the damage characteristic is determined by delamination. For 45°-QI thin-ply laminates FPF is delayed nearly up to ultimate failure and thereby increasing the strength and design space considerably [13, 18, 19, 57]. Additionally, delamination initiation at matrix cracks or at free edges is delayed or even suppressed [13, 18, 58, 59]. The Bouligand layup suppresses all damage modes, except matrix cracking before fibre-failure. However, Table 4.3 reveals the low FPF strength of the Bouligand, which occurs between 44 and 47 % of the ultimate load, whereas 45° thin-ply layups achieve a significantly higher FPF at $\geq$ 90 % of the ultimate load.

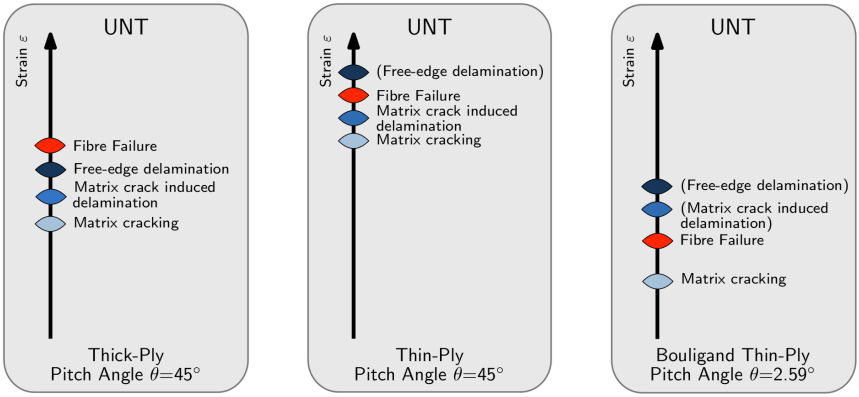

Figure 4.12.: Qualitatively visualised damage sequence of UNT 45°-QI thick-ply, 45°-QI thin-ply and Bouligand-thin-ply

4.3.2. Open-Hole Tension

Figure 4.13 displays the stress-strain responses of the OHT Bouligand specimens. Generally, the characteristics are similar to the UNT specimens (compare Figure 4.5).

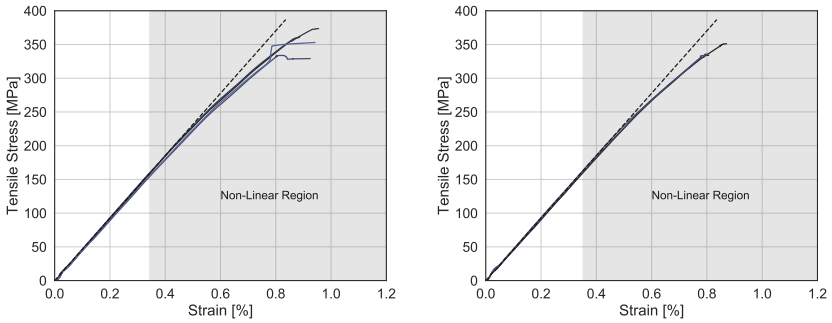

a) b)

Figure 4.13.: Stress strain curves of the neat OHT specimen (a) and nano OHT specimen (b)

The properties resulting from the tensile tests are summarised in Table 4.4. Figure 4.15 presents the damage development in a representative OHT neat specimen with increasing load. Similar to the UNT specimen, cracks grow from

the specimen edge into the specimen (compare Figure 4.7). The shape is also helicoidal (see Figure 4.14), as the matrix cracks follow the fibre rotation.

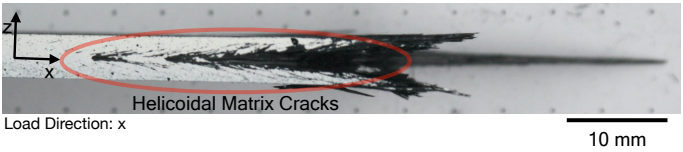

Figure 4.14.: Matrix cracks occurring in a rotating, helicoidal pattern

Additionally, cracks are initiated at the hole (see Figure 4.15). Due to the high shear loads in low angle plies, shear matrix cracking occurs and initiates transverse cracks in neighbouring plies. This leads to a spread of damage over a large area from the hole when the load is increased. However, compared to 45° thick-ply pitch angle laminates, the shear cracks in low angle oriented plies cannot easily propagate, due to increasing crack growth resistance with crack propagation, because the helicoidal layup twists. This effect limits the damage propagation significantly. When viewed from the centre of the hole in x-direction, the longitudinal shear crack is developing in longitudinal direction, but only on the right hand side with a deflection of propagation direction in pitch angle direction. Since the longitudinal cracks are only visible on the right hand side, they are only initiated in the outer 0° and adjacent plies.

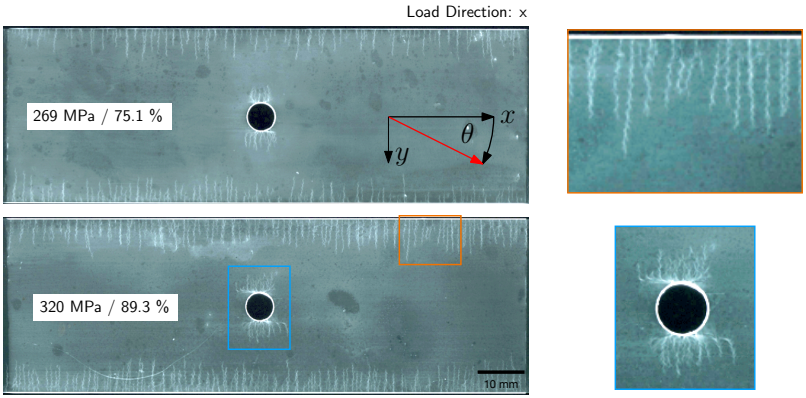

Figure 4.15.: Radiographs of an exemplary OHT specimen at increasing load levels

This effect can also be observed in contour strain plots derived from the DIC (see Figure 4.16). Damage initiates in the plies with angles close to 90°. With increasing load, shear-induced matrix cracking spreads the occurring matrix damage over a large portion of the specimen in the hole vicinity.

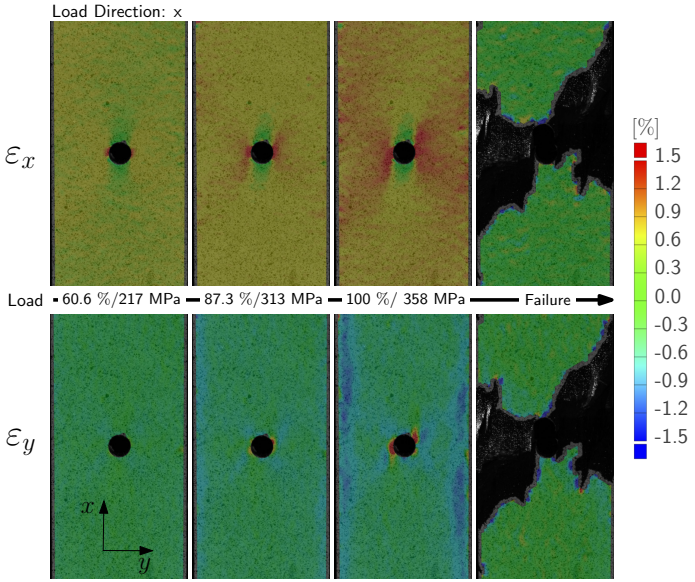

Figure 4.16.: Strain distribution in tensile ε_x and transverse ε_y direction in OHT specimens with increasing load

The load shadow resulting from the hole can be seen in Figure 4.16 in front and behind the hole in load direction. The shadow rotates to the right as the load increases and follows the direction of ply rotation. Accordingly, the strain distribution is point-symmetrical in the vicinity of the hole. At the edges, the strain distribution is similar to the unnotched case. Diffuse matrix cracking is also present at the hole, but subjected to the through-thickness anisotropy of the laminate, see the radiographs in Figure 4.15.

Table 4.4.: Tensile properties of UNT and OHT specimens

	$\sigma_{\mathrm{t}}^{onset}$ [MPa]	$\sigma_{\mathrm{t}}^{\max}$ [MPa]	$\sigma_{\mathrm{net}}^{\max}$ [MPa]	E_{t} [GPa]	k_{F}
OHT Neat	159.10 ± 16.10	360.02 ± 16.49	431.06 ± 19.76	46.37 ± 1.10	0.941
OHT Nano	163.01 ± 23.43	342.05 ± 9.41	414.42 ± 11.38	46.13 ± 0.19	0.894
UNT Neat	175.79 ± 12.39	382.76 ± 7.39	-	47.84 ± 0.72	-

Table 4.4 reveals that the notch sensitivity k_F is low, as the ratio of OHT far field strength to UNT strength is almost one. When comparing the X-ray images in Figure 4.7 and 4.15, the crack density in net-sections next to the hole is significantly higher compared to the unnotched specimens. The higher crack density leads to the reduction of stress concentrations and thus delays the fracture. This assumption is supported by comparing the strength values of neat and nano specimens, as the nano specimens display a lower OHT strength, see Table 4.4. Table 4.5 summarises the mean cumulative energy dissipation of the specimen configurations as determined by the AE measurement during the test until failure. The dissipated energy of the nano specimens is only 72 % of the neat specimens, which indicates lower damage until final failure. This behaviour can be accounted to the higher ERR of the nano material. The higher ERR delays crack development and progression, as a result fewer cracks are formed. Therefore, it can be derived, that the ERR is an important material property to consider when designing Bouligand structures. Consequently, appropriate ERR values need to be found in future research, which allow dispersed damage to form and thereby dissipate energy, while sustaining structural integrity. The optimal ERRs are thereby dependent on many influencing factors, like, e.g. fibre type, ply thickness, pitch angle and loading scenario.

Table 4.5.: Accumulated acoustic energy at failure by AE Measurement

Type	Total Accumulated Energy [pJ]
UNT Neat	6109.12 ± 264.66
OHT Neat	6729.67 ± 299.28
OHT Nano	4644.77 ± 236.12

The failure appearance of the OHT specimen is similar to the UNT specimen (see Figure 4.14 and Figure 4.18). The fibre fracture distribution depends on the direction of the fibre rotation of the ply structure. One half is strongly distributed while the other half is localised.

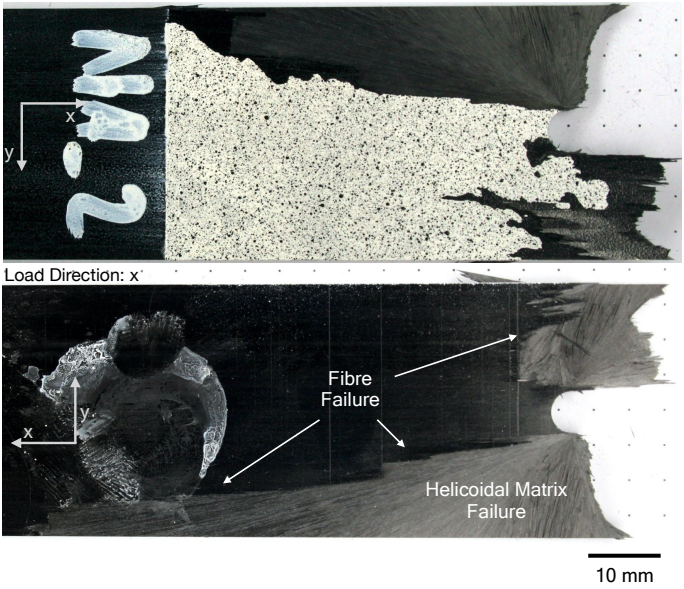

Figure 4.17.: Helicoidal shaped matrix failure and distributed fibre fracture of an OHT specimen

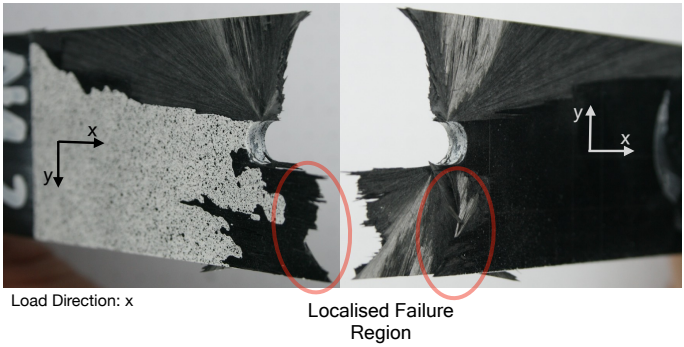

Figure 4.18.: Half of the OHT specimen displaying a localised fibre fracture distribution

Table 4.6 compares the data of the OHT Bouligand layups to 45°-QI neat specimens with areal weights of $30\,g/m^2$ and $120\,g/m^2$ made from the same constitutes. The data summarises the advantages and disadvantages of the Bouligand layup. Damage onset is considerably lower, as it is almost double for both 45°-QI layps with different ply thicknesses. Yet, the far field strength and the net-section strength are similar. This is remarkable, as the 0° fibre angle proportion is considerably lower. Also the low notch sensitivity factor is put into perspective, as the Bouligand neat specimens display a notch sensitivity factor of $k_F = 0.941$, the 45°-QI $120\,g/m^2$ $k_F = 0.941$. The notch sensitivity of the Bouligand layup is also significantly lower than the notch sensitivity $k_F = 0.76$ reached by Wu et al. [141] with the pseudo-plasticity approach, which highlights the potential of small angle layups.

Table 4.6.: Comparison of the tensile properties of Bouligand and 45°-QI layups

	σ_t^{onset} [MPa]	σ_t^{max} [MPa]	σ_{net}^{max} [MPa]	k_F
OHT Bouligand Neat	159.10 ± 16.10	360.02 ± 16.49	431.06 ± 19.76	0.941
OHT 45°-QI Neat $30\,g/m^2$	342.66 ± 5.05	391.10 ± 4.92	467.44 ± 5.98	0.42
OHT 45°-QI Neat $120\,g/m^2$	298.54 ± 25.04	416.15 ± 13.05	499.18 ± 15.58	

The failure behaviour of the different layups is also qualitatively summarised in Figure 4.19.

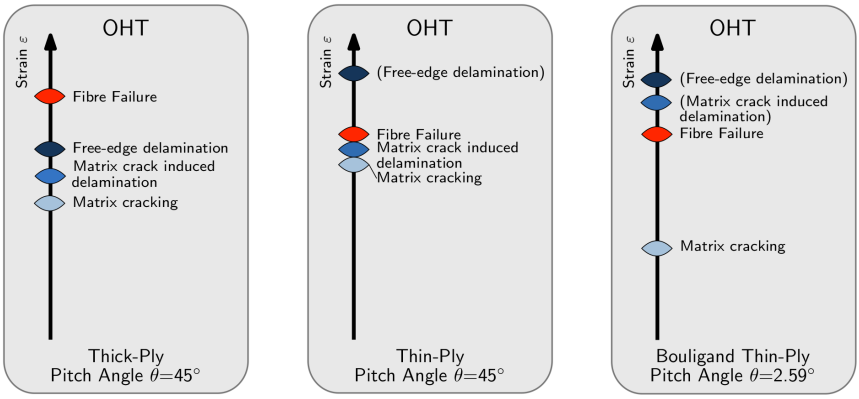

Figure 4.19.: Qualitatively displayed damage sequence of OHT 45°-QI thick-ply, QI-thin-ply and Bouligand thin-ply

4.3.3. Bending

Figure 4.20 displays the bending stress-strain curves of the Bouligand and 45°-QI pitch angle laminates.

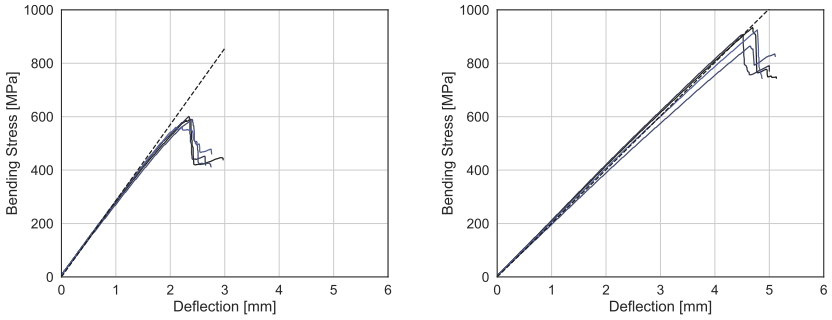

a) b)

Figure 4.20.: Three-point bending stress-strain curves of thin-ply Bouligand (a) and 45°-QI pitch angle (b) results

The derived mechanical results are summarised in Table 4.7. Due to the higher anisotropy of the Bouligand laminate in bending compared to the 45°-QI layup, the bending stiffness E_{B} in the tested laminate direction is significantly increased. The bending strength σ_{b} and consequently the failure strain ε_b^{max} however, is lower.

Table 4.7.: Bending properties of Bouligand compared to a 45°-QI layup

	$\sigma_{\mathrm{b}}^{\mathrm{max}}$ [MPa]	ε_b^{max} [%]	E_{b} [GPa]
45°-QI Layup	907.77 ± 30.52 MPa	2.48 ± 0.11 %	41.77 ± 5.12 GPa
Bouligand-QI	586.54 ± 16.84 MPa	1.86 ± 0.02 %	46.20 ± 2.83 GPa
	−37 %	−25 %	+11 %

Figure 4.21 is displaying failed bending specimens of the two configurations.

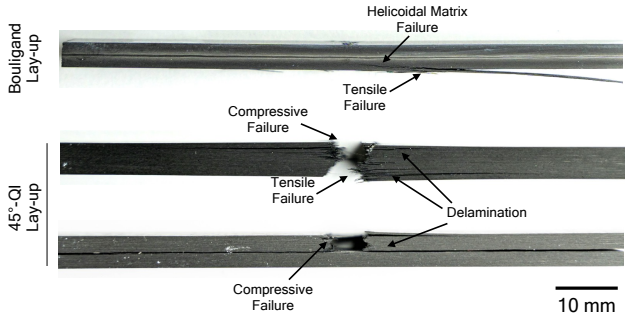

Figure 4.21.: Three-point bending failure of Bouligand and 45°-QI 30 g/m^2 layup

Matrix failure is initiated in or close to the 90° ply of the lower Bouligand unit and consequently steps trough the outer tensile loaded plies, subsequently reducing the bending stiffness, see Figure 4.20. The load drops suddenly, when the 0° fibres and fibres with angles close to 0° fail. Due to the underlaying helicoidal matrix damage, the tensile-fibre failure is non-localised, as in the tensile specimen (see Figure 4.17). The strength of the Bouligand laminates is 37 % lower than the 45°-QI layups. The 45°-QI layup displays different failure modes, see Figure 4.21. They either split and fail catastrophically or fail in a combination of compressive failure and delamination. However, after failure the load carrying capabilities are fully lost as the laminate has fully separated. The fracture behaviour of the Bouligand layup on the other hand is good-natured and does not show catastrophic failure. From a fail-safe point of view, the Bouligand structure is considered more favourable. There is no risk of ply delamination and a limited residual loading capability is retained. In addition to structures with a high probability of impact damage such behaviour is suited for crash elements.

4.3.4. Impact Resistance

The damage resulting from LVI for the Bouligand structures is characterised by the formation of subcritical matrix damage. With the chosen impact parameters no fibre failure is visible. The projected damage areas, obtained by the C-scans are summarised in Table 4.8. The projected damage area shows a significant

reduction compared to 30 g/m^2 45°-QI laminates. For all tested configurations the projected damage area is reduced at least to 55 %.

Table 4.8.: Projected damage area of impacted CAI specimens

Type	Projected Damage Area [mm^2]	Compared to 45°-QI [%]
45°-QI Neat 30 g/m^2	5881.35 ± 1323.66	-
Bouligand Neat	2746.56 ± 350.25	-53
Bouligand Nano	3258.17 ± 293.64	-45

Opposed to C-scans the CT measurements enable to 3-dimensionally image the damage pattern and thus distinguish damage features in different depths of the specimens. Figure 4.22 shows a CT scan of the occurring failure in neat specimen. Here, the helicoidal shape of damage is visible. In the y-z plane the helicoidal twisting of the matrix cracks is obvious. The cracks start in the top ply parallel to the x-axis and are then deflected with the twisting plies until the crack is stopped at a fibre angle close to 90°. However, in the x-z plane at a distance of 0 mm from the impact point, the same behaviour is visible only starting in the 90° ply. When the crack gets deflected due to the twisting plies the angle between the x-axis and the crack is converging 0°, not forming a delamination. The nano specimen shows a slightly different failure behaviour. The increase in ERR reduces the crack density significantly, which is particularly visible when comparing the cut through the impact point in the x-z plane. The neat specimen has a very high crack density especially in the lower half of the sample while the nano specimen only shows a reduced number of cracks. However, this lower number of cracks leads to a larger projected damage size, as the fewer cracks propagate further, as displayed in Table 4.8.

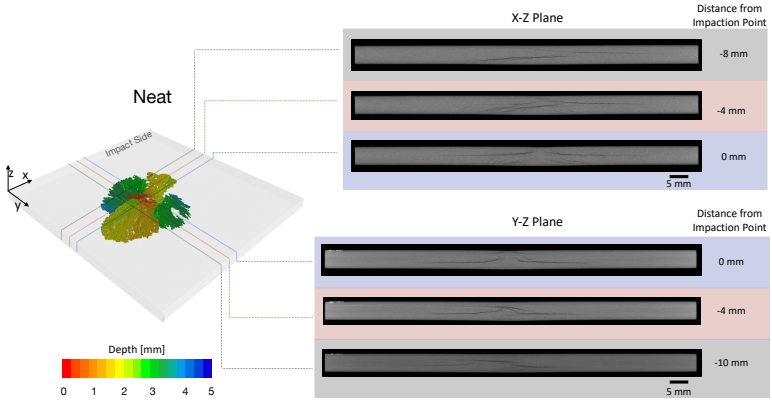

Figure 4.22.: CT image of the LVI damage in a neat specimen (Displayed on the left is an overview image, and on the right various cross-sectional presentations)

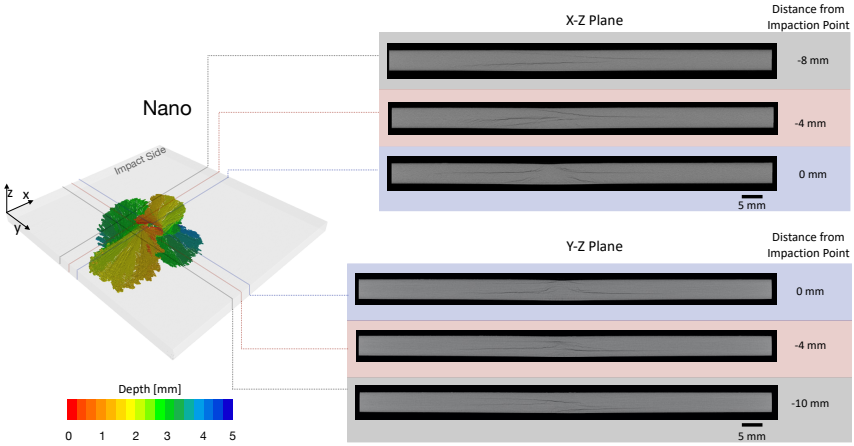

Figure 4.23.: CT image of the LVI damage in a nano specimen (Displayed on the left is an overview image, and on the right various cross-sectional presentations)

4.3.5. Compression After Impact

Table 4.9 summarises compression and residual compressive strength of the tested configurations. The compressive strengths are higher than the tensile strengths, due to early matrix damage initiation under tension. The residual compressive strength of the nano specimen and the neat specimen is similar, 193.81 and 194.63 MPa, respectively. The strength retention lies between 40 and 45 %. Despite the reduced amount of matrix cracks resulting from the LVI, the nano specimens show no increase in residual strength. This behaviour is caused by the main cracks that determine the failure behaviour, which are similar for the configurations (see Figure 4.22 and Figure 4.23).

Table 4.9.: Properties of compression and CAI specimens

	σ_c^{max} [MPa]	E_c [GPa]	Strength Retention [%]
Comp. Neat	492.33 ± 2.53	42.67 ± 2.5	-
Comp. Nano	428.56 ± 25.08	46.47 ± 1.96	-
CAI Neat	194.63 ± 7.49	44.62 ± 2.71	40
CAI Nano	193.81 ± 8.21	46.97 ± 0.06	45

Figure 4.24 shows representative stress-strain curves for the compressive behaviour after impact for the neat and nano Bouligand layups and 45°-QI layup 120 g/m^2 specimen. The Bouligand layups exhibit a significantly higher stiffness and strength, compared to the 45°-QI layup.

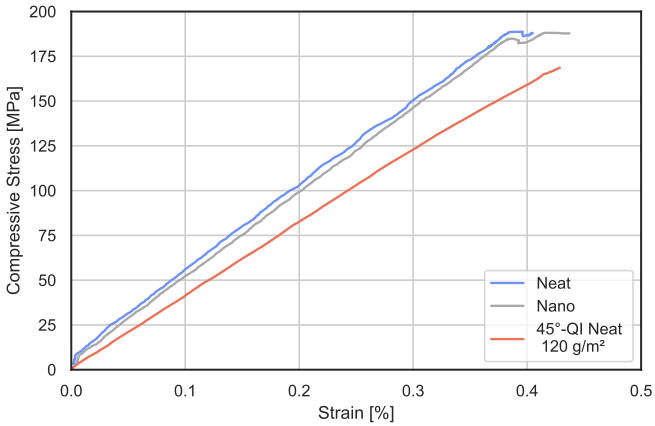

Figure 4.24.: Exemplary stress-strain curves of the Bouligand configurations and a 45°-QI neat 120 g/m^2 specimen

Figure 4.25 shows the failure of a representative neat specimen, the resulting failure of the nano specimen is very similar. The damage is characterised by helicoidal matrix damage and localised fibre failure. Failure initiates at the helicoidal matrix damage resulting from the impact, grows in loading direction and causes final fibre failure. The result is a highly distributed failure appearance. Distributed fibre failure in the fibre plies with an orientation close to the load direction governs the final failure.

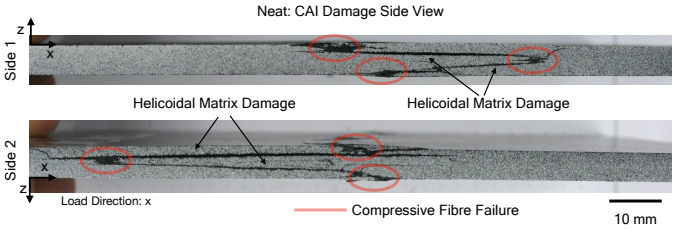

Figure 4.25.: Side view of the occurring damage modes of a neat Bouligand specimen

Table 4.10 compares the obtained data of the Bouligand layups with data from 45°-QI layups. The Bouligand layup displays a 15 % higher compressive residual

strength than the 45°-QI laminates, despite the considerably lower proportion of 0° fibres in the load direction. Therefore, the Bouligand layup uses the fibres' potential to a greater extent than QI-layups by suppressing delamination damage. The failure appearance explains the fully retained compressive modulus E_c, because no local buckling occured. This is in contrast to 45°-QI laminate constructions, which only retain approx. 60 % stiffness due to the delaminations causing local buckling. It states the maximum out-of-plane displacement during the test, derived from the DIC measurements. The QI-layups exhibit significantly higher displacements, which correlate with the delamination size (compare Figure 5.6). The z-displacement of the Bouligand specimens results from the wedge-like matrix failure after fibre compressive failure. This damage characteristic results in a further significant improvement in damage tolerance, as load redistribution in a structure only initiates when the residual strength is reached and not as soon as the impact damage occurs. This retention of the stiffness after impact allows larger structures to remain fully functional up to a specific load level, even with impact damage.

Table 4.10.: Comparison of the residual compressive properties with a 45°-QI 120 g/m^2 layup

Type	CAI Strength		Max. Z-Disp.	Modulus Retention
	σ_c^{max}	$\Delta\sigma_{c,\,ref}^{max}$		
	[MPa]	[%]	[mm]	[%]
Bouligand Neat	194.63 ± 7.49	15	0.729	≈ 100
Bouligand Nano	193.81 ± 8.21	14	0.749	≈ 100
45°-QI Neat 30 g/m^2	176.52 ± 1.70	4	4.47	58
45°-QI Nano 30 g/m^2	177.65 ± 9.17	5	5.105	61
45°-QI Neat 120 g/m^2	169.50 ± 6.64	–	1.08	58

4.4. Conclusion

The working hypothesis for this chapter established in the introduction reads:

The composite's layup controls the occurring matrix damage modes. Thin-ply, bio-inspired helicoidal layups enable delamination-free composites.

The results thoroughly validated the hypothesis, as the investigated small pitch angle laminates enable delamination-free composites. Especially the results from the LVIs reveal the potential of the investigated thin-ply Bouligand layups. Laminates with a pitch-angle of 2.07° have a 53 % lower projected damage area than classic 45°-QI laminates. Furthermore, only sub-critical matrix cracks occur. The absence of delaminations leads to full stiffness retention during CAI testing. As a result, the failure in CAI testing is not caused by local buckling, like classic 45°-QI laminates but by distributed failure in the fibre plies with an orientation close to the load direction. The result is a high residual compressive strength, which is 15 % higher than 45°-QI laminates with 120 g/m^2 ply thickness, despite the considerably lower proportion of 0° fibres in the load direction. Therefore, Bouligand layup uses the fibres' potential to a greater extent than QI-layups by suppressing the matrix damage.
The tensile properties are also noteworthy. The damage onset stress of Bouligand specimens a with 2.59° pitch angle is significantly reduced compared to 45°-QI specimens because matrix crack initiation is no longer constrained by neighbouring plies with high stiffness orthogonal to crack growth. However, only limited subcritical continuously increasing matrix damage develops before ultimate failure. The laminates exhibit a low tensile strength, caused by the limited amount of fibres in the load direction. Nevertheless, due to subcritical damage development, the tensile strength is barely affected by stress concentrations and thus almost shows no notch sensitivity. The tensile strength is only 6 % lower for OHT specimens than for UNT specimens, while the net-section strength increases due to a higher possible matrix crack density. The OHT specimens achieve nearly the same strength as 45°-QI ply structures, despite a significantly lower 0° proportion of fibres. Under bending loading Bouligand specimens achieve a higher bending stiffness and predictable good-natured failure, but lower strength than 45°-QI specimens.

The results shown demonstrate the potential that small-angle laminates have. Further investigation of non-linear pitch angles is a promising way to increase composites' performance further, e.g. the OHT Bouligand samples' strength could be increased while retaining the excellent notch sensitivity factor.

5. Damage Tolerance under Temperature Influence

As presented in the introduction the environment is, as one of the factors influencing the composites' behaviour, an essential parameter to consider when evaluating the damage tolerance of composites. The present chapter and Chapter 6 are dedicated to the working hypothesis:

The matrix's mechanical performance decreases with increasing environmental temperature and negatively influences the damage tolerance of the composite.

Impact damage and the resulting residual strength are critical design factors in the aerospace industry [17, 147]. However, the composite structure's impact resistance under temperature plays an essential role in high-performance composites, e.g. for space structures [31], personal safety equipment [148] and pressure vessels [3, 149]. Impact damage is potentially susceptible to temperature since the matrix's properties are particularly influential because the impact leads to out-of-plane loading of the layered composite structure. Consequently, it is essential to know how the environmental temperature influences the damage caused by LVIs and the resulting residual strength.

5.1. State of the Art

5.1.1. Operating Temperatures of Composite Structures

The ambient temperatures which composite structures experience in operation depend on their field of use. However, the matrix's mechanical properties are sensitive to temperature changes [26] and as a result also the composite. Consequently, the conditions of use must be known, or if they are unclear, a safety factor for the unknown conditions to guarantee the damage tolerance must be regarded [17]. To utilise composites' full light-weight design potential, and still

obtain safe structures, comprehensive knowledge about the influencing factors on the damage tolerance is necessary. The available data on temperatures that CFRP structures experience during operating is limited. However, for structures used in aviation, design rules exists, which need to be considered for the structural design [17]. These design rules state a minimum service temperature of −54 °C and a maximum temperature of 71 °C. Other temperature boundary conditions may apply if there are other heat sources in the composite component's vicinity. However, CFRP structures can reach even higher in-service temperatures. Petersen et al. [150] performed numerical simulations of a CFRP wing box heated up by sun radiation at a high altitude airport. They encountered that the wing's maximum surface temperatures are between 68 and 110 °C during ground operation, depending on the surface's colour. Cooling of the wing during taxi and take-off led to reduced maximum temperatures between 63 and 87 °C. Nevertheless, even at airports, where the radiation is not as intense, similar temperatures are likely to be reached, e.g. Kuwait International Airport has reported a maximum temperature of approx. 50 °C in June and July [151]. This data also shows that composites' operation temperature easily reaches high values, in which the mechanical performance is diminished [27, 30]. Therefore nearly all CFRP structures can be exposed to elevated temperatures if the conditions are not known in full detail, affecting the mechanical performance.

5.1.2. Influence of Temperature on the Mechanical Properties of Composites

The main reason for the composite's temperature-dependent behaviour is the change of the epoxy matrix's mechanical properties, which are significantly more sensitive to temperature than those of the fibres. With increasing temperature, the epoxy matrix exhibits a lower strength, modulus, yield point and a higher strain at breakage [26]. The change in mechanical properties thereby depends on the operation temperature compared to the glass transition temperature T_g [26]. As a result, nearly all mechanical properties of the composite are also changing with the temperature, even at temperatures well below T_g. With increasing temperature, the fibre parallel compressive modulus, strength and failure strain decrease [30]. The shear strength and modulus also decline with rising temperature, but the fracture strain increases [30, 152]. The transverse tensile strength decreases with temperature [153]. The interlaminar shear strength (ILSS) declines considerably [152]. However, the tensile properties in fibre direction are

nearly constant [27]. Investigations on the temperature dependence of the interlaminar ERRs resulted in inconclusive results. Kim et al. [29] and Zhao et al. [154] demonstrated that under mode I loading, the initiation fracture ERR is reduced slightly with increasing temperature, but the propagation ERR increases. Cowley [28] and Russel [155] found that under mode II the ERR is almost constant with increasing temperature.

The difference in thermal properties of fibre and matrix leads to orthotropic thermal expansion behaviour of a single ply. When the laminate is cooled from the curing temperature, internal stresses occur due to adjacent plies' constrained contraction. These internal thermal stresses decrease with increasing operating temperature up to a temperature close to the curing temperature [156, 157].

The previously mentioned influencing factors do not combine linearly but nonlinearly to influence the failure behaviour. Additionally, temperature dependence is also influenced by, e.g. the laminate design, the structural design (see Figure 1.1), just like the damage tolerance in general.

The impactor applies complex loads on the composite during the impact, and the out-of-plane load results in a complex stress state inside the laminate. Compressive, tensile and strong interlaminar shear loads occur and cause various damage modes. As a result, it is challenging to estimate how the failure behaviour is affected at different temperatures.

5.1.3. Temperature Influence on Low-Velocity Impact Damage

LVI damage and the resulting residual strength has been the subject of considerable research [24, 103]. However, the number of studies that have investigated the influence of ambient temperature is sparse. Gómez-del Río et al. [158] examined the damage in CFRP, caused by LVI at ambient temperatures between −150 and 20 °C. They investigated UD, QI, cross-ply and woven-ply laminates with thicknesses varying between 1.6 and 2.2 mm and impact energies between 1 and 13 J. A 60 mm diameter circular clamping was used during the impact. The results indicate that cooling the laminate has a similar effect on the failure behaviour as an increase of impact energy at room temperature. Gómez-del Río et al. reason that the larger extent of damage at lower temperatures results from lower specific fracture energy of the epoxy matrix combined with increasing interlaminar thermal stresses. Decreasing temperature leads to more severe matrix

cracking, delamination extension and deeper indentation on the impacted side and more severe fibre fracture on the opposite face [158]. This larger delamination area could lead to a lower residual compressive strength, as the residual bending strength of cross-ply or quasi-isotropic laminates in compression loading after impact is mainly dependent on delamination size and distribution in thickness direction inside the laminate [129]. Survana et al. [159] investigated the influence of temperatures between 30 and 90 °C on the damage resulting from LVI. The resin system had a 212 °C nominal T_g. Cross-ply $[0/90_2/0]_{2s}$ CFRP laminates were impacted with an energy of 4.3 J, using a 36 mm diameter circular clamping fixture. They observed that the size of the projected damage area reduces as the temperature increases, showing a contrasting effect compared to cooling the laminate. Survana et al. argue that interlaminar fracture toughness increases with temperature. Consequently, the largest delamination area results from impacts at the lowest temperature. The residual strength was determined using three-point bending tests at room temperature. The residual strength increases with the impact temperature due to the lower damage area at elevated temperatures. Im et al. [160] investigated the influence of temperatures ranging from −30 to 120 °C on high-velocity impact damage of CFRPs. Cross-ply laminates with layups of $[0_6/90_6]$ and $[0_4/90_4]$ and a T_g of 130 °C were used. Impact damage was introduced via a 0.5 g steel ball and a circular clamping with a 150 mm diameter. Impact velocities ranged between 50 and 105 m/s and the resulting energies between 0.625 and 2.7 J. They found that delamination formation needs more energy at higher temperatures. Thus the delamination area decreases with increasing temperature. As a result, the residual bending strength rises with the impact temperature.

The only studies which evaluate the influence of temperature during LVI on the resulting residual compressive strength of FRPs were performed by Aktaş et al. [161, 162]. In [161], they investigated the residual compressive strength after LVI of quasi-isotropic and cross-ply GFRP laminates with 3 mm thickness. The resin system had a 100 °C nominal T_g. The impact energy was varied between 20 and 70 J and the temperature between 20 and 100 °C. The compressive tests were performed in a fixture according to ASTM D 7137 [44] only at room temperature. The maximum reduction of the CAI strength was obtained with impacts at 100 °C while the minimum strength reduction was obtained at 20 °C throughout all impact energies. They found that the influence of temperature on damage size is more significant for cross-ply laminates than quasi-isotropic laminates

for the same energy level. However, they gave no details on the change of the occurring failure. Besides the residual compressive strength Aktaş et al. [162] also investigated the influence of temperature on the impact behaviour, with the same setup. Impacts were introduced at 20 °C, 60 °C and 100 °C and impact energies investigated were between 5 and 70 J. The results show that the fibre breaking limit increases with temperature and the specimen's energy-absorbing capability lessens with increasing temperature. Again, no detailed information on the laminate's damage morphology was given.

As the literature review reveals, the focus of studies investigating the temperature's influence on LVI damage of CFRP laminates was mostly on cross-ply laminates with a small laminate thickness. Systematic research investigating the effect of temperature and impact energy on residual compressive strength has not yet been published.

5.1.4. Temperature Influence on Residual Compressive Strength

Studies which focus on the effect of temperature on the residual strength are limited. Saez et al. [163] investigated the residual compressive strength after LVI of CFRP laminates at 20 °C, −60 °C and −150 °C. They found that for quasi-isotropic laminates, the compressive strength is not significantly changed when lowering the temperature. The residual compressive strength retention factor ranges from 30 to 36 %. However, they only tested thin samples of 1.6 mm, which probably has to lead to a low extent to delamination damage, resulting in a limited sensitivity to ambient temperature. Nettles [31] and Callus [152] did not investigate the strength after impact, but the open-hole compression (OHC) strength. They found that the strength and fracture strain decrease with increasing temperature. However, the damage resulting from impacts could be more temperature-sensitive in residual strength testing because, due to the delamination damage, it is mainly stability driven [25, 164]. Following the literature review, the most critical parameter set could be the impact at low temperature, leading to extensive delamination damage and afterwards compressive loading at elevated temperature.

5.1.5. Residual Tensile Strength

The influence of impact damage on the residual tensile strength has been of considerable research [24, 25, 164]. Generally, the residual tensile strength after LVI is reduced, caused by stress concentrations resulting from impact damage [25]. Studies that attribute individual failure modes to a change in residual tensile strength are scarce. Zhou et al. [165] investigated the influence of different layups, impactor diameters, impact angles and energies on the residual strength. They found that fibre damage occurs on the top side of the specimen around the impactor's contact area, regardless of impactor size. The severity of fibre failure increases with decreasing impactor diameter, which also reduces the residual tensile strength. However, the resulting delaminations from the impact were spanning across the sample's whole width for nearly all parameter sets [6]. As a result, the residual strength's sensitivity to different occurring damage modes could be reduced, highlighting that impact testing of small specimens and evaluating the residual strength is generally a challenge.

During LVI testing often no fibre failure occurs on either side of the specimen, as this requires high impact energies [24]. As a result, the change of failure modes at elevated temperatures seen in the compressive specimen from no fibre failure to extensive fibre failure on the impacted side could influence the residual strength considerably.

This chapter investigates the influence of temperature and impact energy on the resulting LVI damage in CFRPs. To determine the compressive and tensile residual strength after impact, CAI tests were conducted at room and elevated temperature, while tension after impact (TAI) tests were performed at room temperature.

5.2. Materials and Experimental Setup

5.2.1. Materials

Specimens were manufactured from Hexply M21/35%/268/T800S (Hexcel, USA) [166], which is a toughened high T_g prepreg used in aircraft's primary structures. The layup used is quasi-isotropic $[45/0/-45/90]_{2S}$ with a resulting laminate thickness of 4.25 mm, chosen according to ASTM D7136 M [43]. The prepreg was cured using a 180 °C curing cycle, according to the manufacturer's specification.

Figure 5.1 displays the results from DMA measurement, which reveal an onset T_g of 176 °C.

As this material is used in aviation structures, a material qualification sheet exists, stating the required mechanical properties and test conditions [147]. The qualification states, that the material should at least demonstrate a 150 °C dry onset T_g. The characterisation of the mechanical properties in a dry material state includes ambient temperatures between 55 and 110 °C and in a wet state temperatures between 23 and 110 °C. CAI test should be performed dry at 23 °C and in hot/wet conditions at 70 °C. The impact, however, only takes places at 23 °C [147].

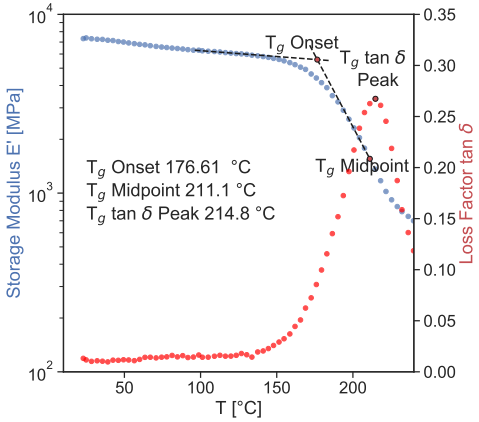

Figure 5.1.: Temperature-dependent storage modulus E' and loss factor $tan\,\delta$ of a transversely loaded laminate and the resulting T_g

5.2.2. Experimental Procedure

The experiments have been divided between specimens used to determine the compressive residual strength and the residual tensile strength, as explained in Chapter 2.

LVI and CAI

The ambient temperatures during LVI considered are −20 °C, 20 °C, 50 °C and 80 °C. 80 °C was selected as the maximum temperature, as this value is slightly

above the design temperature of aircraft structures and thus includes this design space (see Section 5.1.1). −20 °C was included to incorporate temperatures lower than room temperature.

Table 5.1 summarises all impact parameters used. All introduced impacts were LVIs, as classified in [24, 103]. The impactor weights and drop heights are adapted so that the impact velocity throughout the different energy is approximately constant. The maximum impact energy was chosen that no severe fibre fractures occur at 20 °C, as the resulting fibre damage could mask changes in the matrix damage behaviour.

Table 5.1.: Impact parameters for compressive specimens

Impact Energy [J]	Impactor Mass [kg]	Drop Height [mm]	Impact Velocity [m/s]	Impactor Diameter [mm]
8	2.4	300	2.54	20
15	4.45	340	2.60	20
18	4.95	370	2.69	20
21	5.47	390	2.77	20

LVI and TAI

For the tensile specimen the impact energy was chosen as 25 J, supported by a preliminary test campaign (see Appendix B, Figure B.1), so that the delamination growth does not reach the edge of the specimens. This would influence the damage sequence during and the resulting damage modes from LVI. Additionally, during residual tensile strength determination, the load distribution and progressive damage sequence would not be realistic because the extensive delamination would prevent load diversion in the laminate. It was also crucial that the temperature still influences the projected delamination area at the selected impact energy.

The chosen impact parameters are combined in Table 5.2. Five specimens for each parameter set were impacted. Temperatures were chosen according to the compressive specimen. The impact took place at 80 °C and at 20 °C.

Table 5.2.: Impact parameters for tensile specimens

Impact Energy [J]	Impactor Mass [kg]	Drop Height [mm]	Impact Velocity [m/s]	Impactor Diameter [mm]
25	5.34	477	3.06	12

5.3. Results and Discussion

5.3.1. LVI and Compressive Residual Strength

The following section presents the results for a better overview and comparability using graphs. The respective quantitative data is summarised in Appendix B, Section B.1. Figure 5.2 displays the used methods and the order in which the results are discussed.

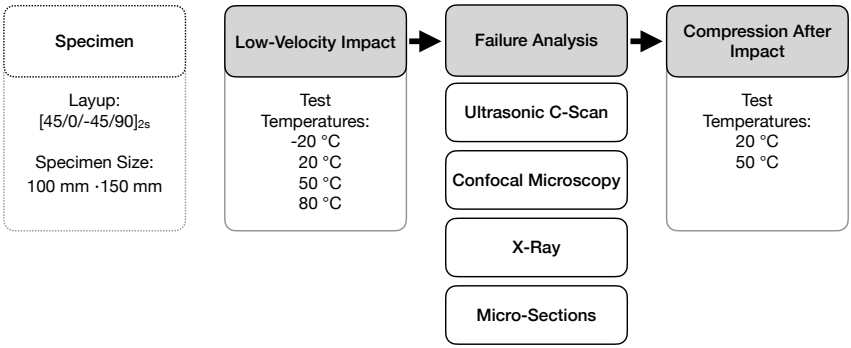

Figure 5.2.: Schematic representation of the test procedure and the analysis methods used to determine the damage after low-velocity impact and the residual compressive strength after impact

Figure 5.3 displays the force-time impact responses of tested parameters at room and elevated temperatures. No loss of contact is observable. Throughout the different impact energies, a temperature change has no significant effect on the specimens' behaviour in the initial phase of the impact, as the initial stiffnesses are similar. The contact time is increasing with impact energy, but no temperature dependency is apparent in this parameter. Contrary to expectation, the maximum contact force is not always increasing with the impact energy (see Figure 5.4), as this is only the case up to 18 J. A temperature dependency of the

maximum force is only identifiable at 15 J. At this impact energy, the highest maximum force occurs at room temperature, the second highest at 80 °C and the lowest at 50 °C. A direct influence of temperature is not visible in the contact force over time curves.

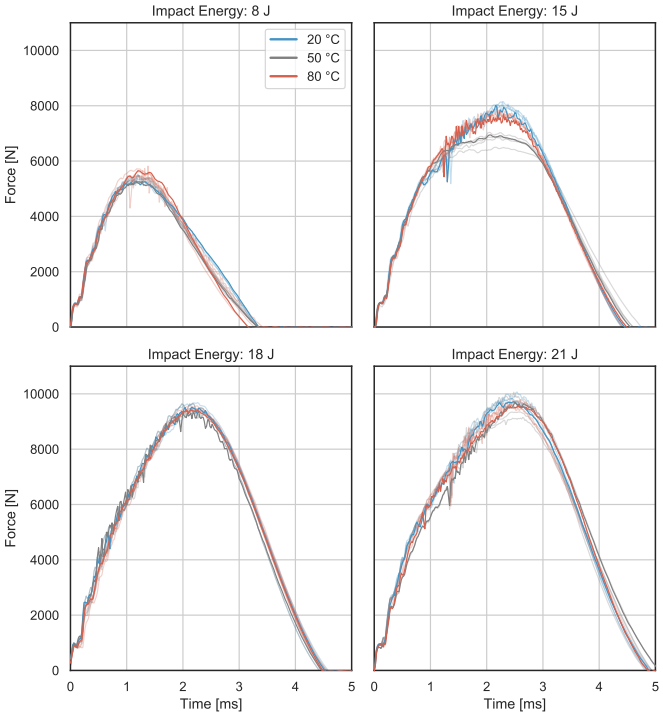

Figure 5.3.: Representative force over time curves for impacts with 8 J, 15 J, 18 J and 21 J impact energy

Figure 5.5 displays the absorbed energy in correlation with impact energy. The absorbed energy increases only slightly with the impact energy, which means that at higher impact energies, more energy is stored elastically during the impact. For impact energies < 21 J the absorbed energy is slightly increased for elevated temperatures.

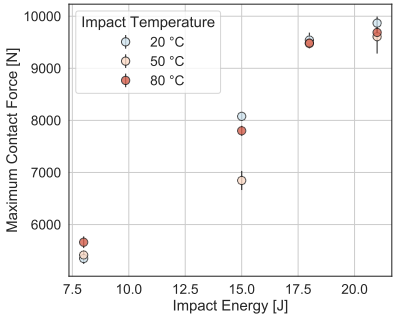

Figure 5.4.: Maximum contact force at different energies and temperatures

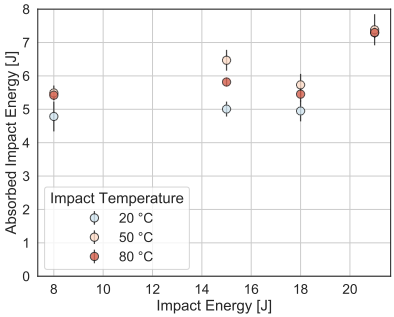

Figure 5.5.: Absorbed energy plotted against impact energy

Figure 5.6 displays the projected delamination area derived from the C-scans. Here the high sensitivity of the projected delamination area to the ambient temperature is visible. At the same impact energy and increasing temperature, the delamination area lessens but not with a constant rate. Thus, with a temperature rise from 20 to 50 °C the delamination area declines by 29 % at 8 J, by 40 % at 15 J, by 11 % at 18 J and by 25 % at 21 J. Cooling the laminates leads to an even greater effect, e.g. decreasing the temperature from 20 °C to −20 °C at 15 J impact energy, leads to an increase of the projected delamination area of 104 %. Figure 5.6 highlights, that with temperature as a variable, the relation between the delamination area and impact energy is no longer unique and different temperature and impact energy combinations can lead to approximately the same projected delamination area. This becomes evident when comparing the delamination areas resulting from impacts with 15 J at 20 °C, 18 J at 50 °C and 21 J at 50 °C. Therefore, the projected delamination area cannot be associated with impact energy without considering the temperature.

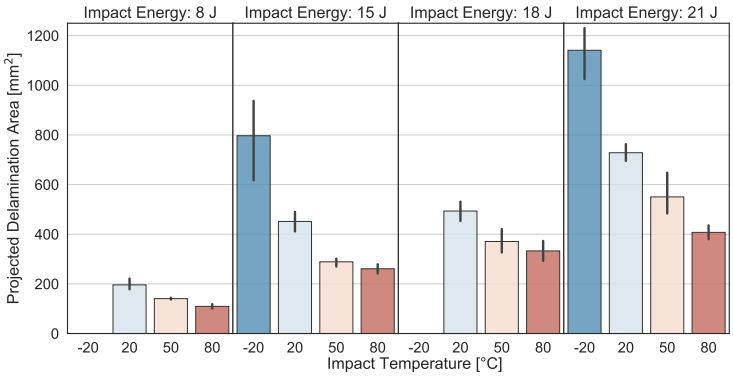

Figure 5.6.: Projected delamination area, determined from the ultrasonic C-scan

Figure 5.7 displays the visible surface damage on the impact side. The images show exemplary damage behaviours. Several representations are displayed when damage appearances within one parameter set are distinctly different. At 8 J impact energy and 20 °C no fibre failure is visible on any specimen's surface. At a temperature of 50 °C, one out of five specimens displays fibre fractures on top. At 80 °C three out of five samples show fibre failure in the top ply. At 15 J two out of five specimens show light fibre breakage at 20 °C, but at elevated temperature, all specimens exhibit fibre failure. The specimens with 18 J impact energy show similar behaviour, while with 21 J impact energy, all specimens exhibit fibre failure.

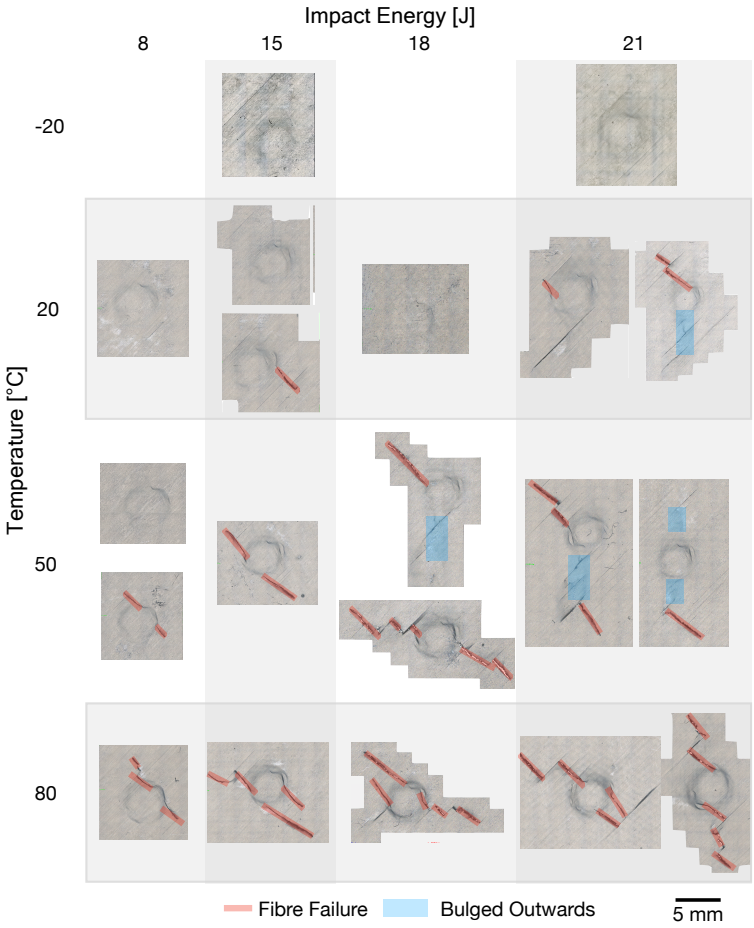

Figure 5.7.: Representative images of the surface damage of the impact parameters studied

In general, with increasing energy and temperature, the extent of fibre breakage advances, and the region over which fibre breakage occurs is much larger. Visually, the ambient temperature has a more substantial effect on the visible damage than the impact energy. Particularly at 80 °C ambient temperature, the extension of fibre failure over the impacted side becomes substantial. Damaged regions occur where the fibres bulge outwards at 80 °C, if no significant fibre fractures form. This failure behaviour means that instead of fibres failing under

compression, the top ply has detached in that region and bulges outwards (see the failure of the 21 J 50/80 °C and 15 J 50 °C). This change in failure modes with increasing impact temperature, meaning the occurrence of fibre failure, which becomes severe with increasing temperature, has not yet been identified to the author's knowledge.

Figure 5.8 displays the permanent deformation resulting from the LVI. The permanent indentation depth increases with the impact temperature and presents a qualitatively inverse relationship to the projected delamination area for all impact energies (compare Figure 5.6). Like the delamination area, there are several energy/temperature combinations with a similar indentation depth, and it is thus impossible to associate the impact energy with a specific permanent indentation. However, all the permanent indentation depths are well below the visible impact damage limit of 0.5 mm [124, 167].

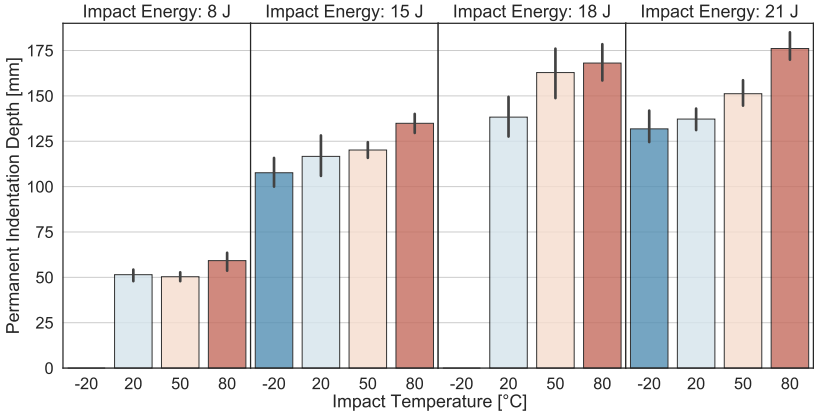

Figure 5.8.: Permanent indentation depth at different temperatures and impact energies

Figure 5.9 shows radiographs of all impact parameters. In the radiographs, both changes in failure modes are visible. At 20 °C and 8 J impact energy, the delamination area is reduced with increasing temperature. The delamination exhibits a round shape, but with increasing temperature, the delamination localises. At elevated temperature, delaminations only occur in the 45° direction close to the impact point. The length of matrix cracks, which span almost along the specimen's whole width on the non-impacted side, also declines with temperature.

When increasing the impact energy to 15 J, the general extent of damage is more widespread. At −20 and 20 °C extensive matrix cracks form in the 45° direction originating from the impact point. The extent lessens when the temperature decreases to 50 and 80 °C. However, starting from 50 °C, fibre failure develops and increases when the temperature rises to 80 °C. Impacts at 18 and 21 J display a similar behaviour, but with significantly larger damaged areas.

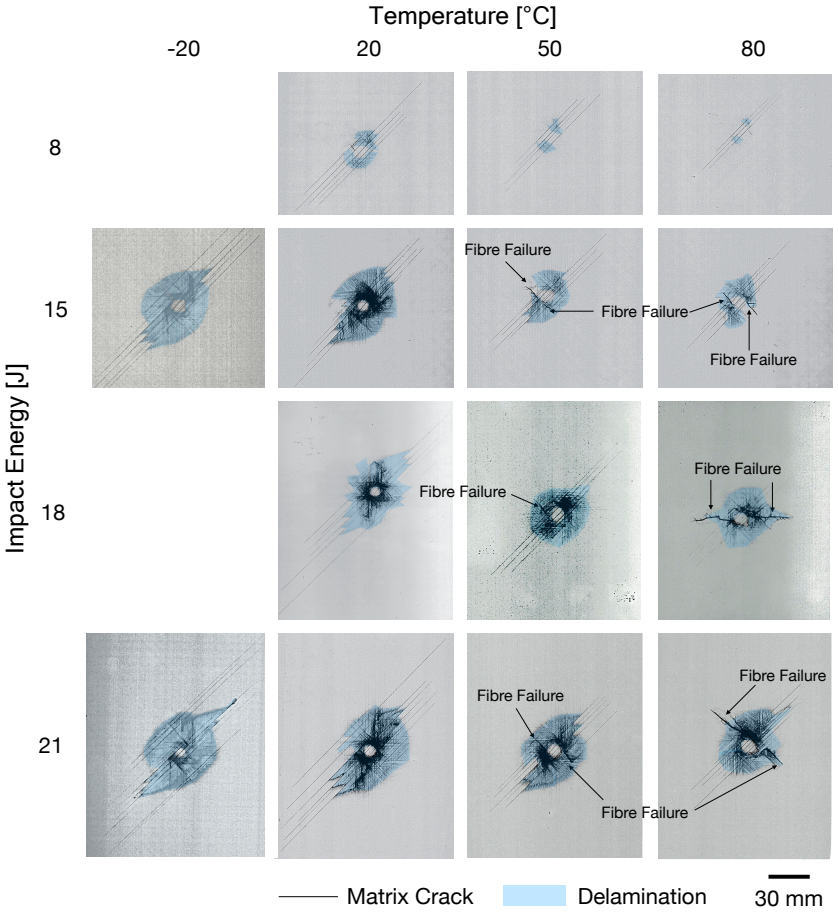

Figure 5.9.: Representative, inverted radiographs of the impact parameters studied

The micro-sections (see Figure 5.10) reveal that the matrix damage at −20 and 20 °C exhibits the classic cone shape, whereas the matrix damage distribution at 80 °C is more or less cylindrical. The blue line is a reference line to highlight the permanent indentation depth visually. The change in the matrix failure distribution, neglecting the delamination failure, reflects the region over which the permanent deformation forms. With the temperature rise from −20 to 80 °C, the span over which the permanent deformation is formed is reduced. The compressive fibre failure is visible at 80 °C on the top side of the specimen. Additionally, a change in delamination behaviour in dependence of the temperature is also visible. Generally, the largest delaminations form above the 90° plies in cutting direction. The delamination distribution also forms a cone shape, which means the spread in delamination increases from the impact side to the non-impacted side. With the increasing temperature, the overall delamination spread reduces. At 80 °C, the delamination above the upper 90° ply vanishes for 15 and 21 J impact energy.

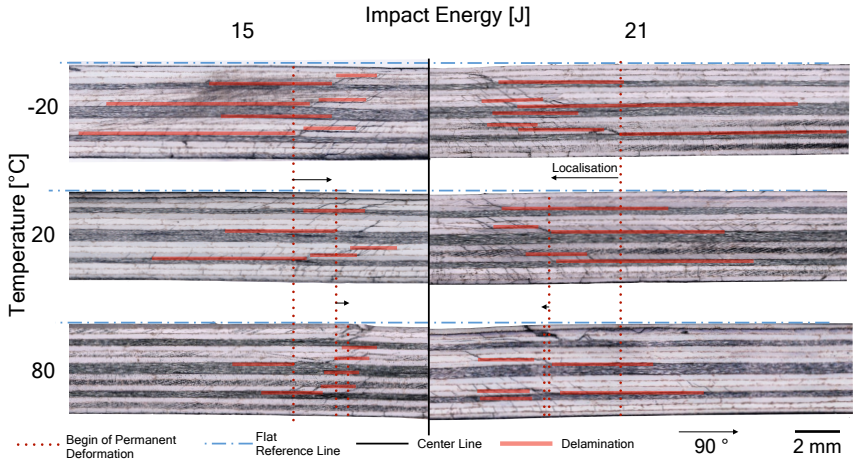

Figure 5.10.: Micro-section through the short side of the impacted specimen at −20 °C, 20 °C and 80 °C

The reasons why fibre failure forms are manifold. Due to matrix softening with increasing temperature and the resulting lower shear modulus and strength of the composite, the occurring matrix damage localises, as visible in the micro-sections (see Figure 5.10), which also leads to a deeper permanent indentation depth.

The top ply exhibits fibre failure due to the highest compressive loads caused by bending during impact. Fibre breakage initiates at the edge of the contact region with the impactor, where high local compressive loads act resulting from bending. Due to the decreasing shear modulus and shear yield point of the matrix, the composite's compressive strength declines, and fibre breakage occurs at lower load levels due to out-of-plane fibre-microbuckling [28, 30]. The higher the temperature, the more the fibre fracture expands from the impact point (see Figure 5.7).

As discussed in the introduction, the structural design strongly influences the damage tolerance. Therefore, it should be pointed out that the clamping strongly influences the resulting stress state in the laminate and the occurring damage modes during impact. The fixture used in this study is, as mentioned, basically simply supported. It allows for relatively unconstrained bending during the impact. A fixture where the specimen is fully constraint at the edges could lead to different kind of failure. Many interrelated effects lead to the reduction of the projected delamination area. With increasing temperature, the interlaminar stresses caused by the mismatch of the plies' thermal expansions coefficients decline and lead to a higher apparent interlaminar strength. Additionally, the more localised matrix failure at elevated temperature leads to reduced delamination initiation at matrix cracks. Consequently, the delamination area lessens. Also, the occurring fibre fractures absorb a considerate amount of energy [168], which means that less energy is available for other failure types. The reduction in maximum force in the force-time curves, observable in Figure 5.3 for the 15 J/50 °C, impact cannot be explained from the resulting damage data.

Figure 5.11 displays the residual compressive strength after impacts at different temperatures determined at 20 °C ambient temperature. All specimens impacted with 8 J failed on the specimen's upper or lower side due to delamination failure at the load introduction rather than at the impact damage. All other specimens impacted with higher energies failed at the damage resulting from the impact. At 15 J, the residual strength increases with the impact temperature. However, all specimens impacted with 18 J energy exhibit a similar residual strength, regardless of the impact temperature. The same is the case for the impacts with 21 J energy, for impact temperatures $\geq$ 20 °C. Only impacts with at 15 and 21 J impact energy at -20 °C result in a significantly reduced residual strength.

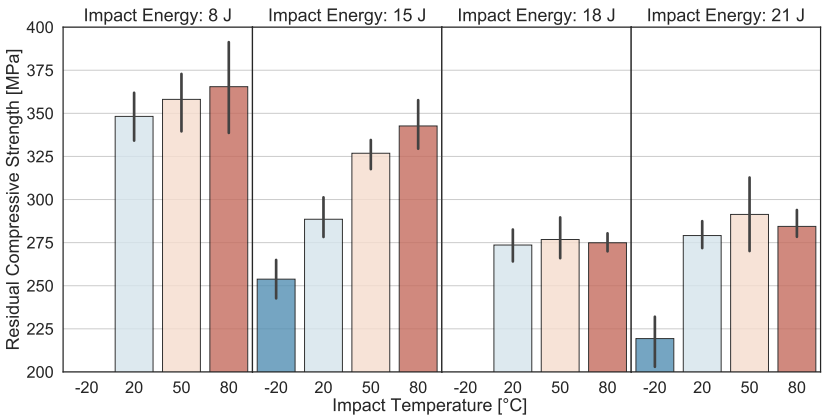

Figure 5.11.: Residual compressive strength at an ambient temperature of 20 °C after impact at different temperatures and impact energies

The reduction of the delamination area with increasing temperature seems to be a positive development in regard to the residual compressive strength, especially when looking at Figure 5.12.

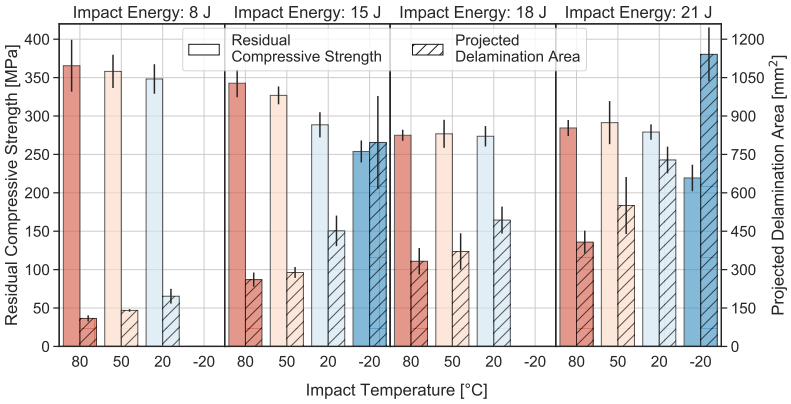

Figure 5.12.: Comparison between delamination area and residual compressive strength at 20 °C

Here the projected delamination area and the residual compressive strength determined at 20 °C are shown. At an impact energy of 15 J a smaller delamination area is corresponding to a higher residual compressive strength, which is similar to the findings of Survana et al. [159], who found a correlation of delamination area to residual bending strength. However, for projected delamination areas greater than 332 mm^2 and smaller than 450 mm^2, a change in the delamination area does not lead to a significant change in the residual compressive strength. This behaviour can be explained by the fixture used in the compression test. The projected size of the delamination area for the occuring determination distribution is already critical to initiate early failure. Therefore, a change in projected delamination area shows no significant change concerning the compressive residual strength. This behaviour could probably be counteracted with a larger specimen and test fixture size. The further drop in residual strength for the specimens impacted at −20 °C can be attributed to the change in delamination distribution over the thickness, visible in the micro-sections (see Figure 5.10), where the delaminations are closer to the mid-plane of the laminate [129].

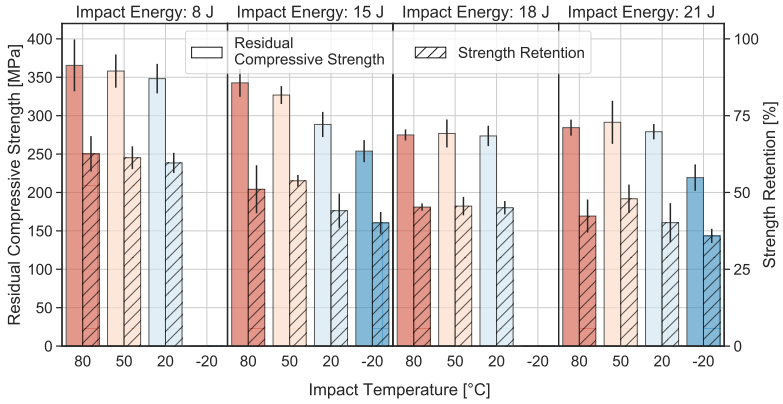

Figure 5.13.: Comparison between the compressive strength retention and the residual compressive strength at 20 °C

Concluding from the residual strength (see Figure 5.12 and Figure 5.13) a larger delamination area leads to earlier material instability and thus lower compressive residual strength, resulting in the lowest tested impact temperature being the most critical - in numerous ways.

Due to the change in failure modes, it becomes clear that visual inspection is not sufficient to assess the damage severity of impact damage. A frequently used characteristic value for assessing impact damage is the indentation depth, which is often associated with impact energy [169]. However, when comparing Figure 5.8 and 5.11 it becomes apparent that the residual strength cannot be judged by the indentation depth, e. g. impacts at 15 J/80 °C and 21 J/50 °C have the same indentation depths and the lowest residual strength results at the lowest indentation depth. The optical detectability of impact damage increases when fibre fractures occur on the impacted side, but no conclusions can be drawn about the residual compressive strength. Rather the opposite is the case: Damage caused by the same impact energy at an elevated temperature that exhibits fibre failure has a higher residual compressive strength. Without considering the temperature, the impact energy is not a reliable parameter to relate the delamination area and residual strength to since different temperature/energy combinations can result in the same residual strength. The encountered fibre failure could influence other residual strengths, e.g. for laminates under shear or tensile loading.

Figure 5.14 displays the residual compressive strength strength of 15 and 21 J impacts, tested at 20 °C and 80 °C ambient temperature during compression. For 15 J impacts the elevated temperature compression tests decrease the strength considerably and result in a narrow spread in residual compressive strength across all 15 J impacts, despite different impact temperatures. With 21 J impact energy the results are similar, and the residual compressive strengths at 80° ambient temperature for all impact temperatures are as low as the minimum strength at 20 °C ambient temperature.

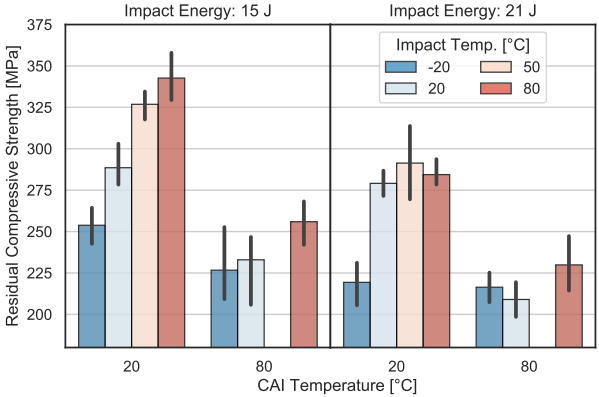

Figure 5.14.: Residual compressive strength at an ambient temperature of 20 °C and 80 °C after impact at different temperatures and impact energies

The severe influence of the temperature on the residual compressive strength becomes apparent (see Figure 5.14) for higher test temperatures. The spread of the residual strength resulting from the different impact parameters becomes narrower. At 15 J the spread at 20 °C is from 342.67±18.19 MPa to 253.83±14.35 MPa and at 80 °C from 255.85±13.20 MPa to 226.68±23.00 MPa. This means, that besides the lower strength also the spread is reduced from 88.84 MPa at 20 °C to just 29.17 MPa at 80 °C. That indicates that the influence of the different impact damages, particularly the delamination damage, decreases because the changing material properties define the stability limit, resulting in the fact, that a higher ambient temperature during compression leads to earlier failure.

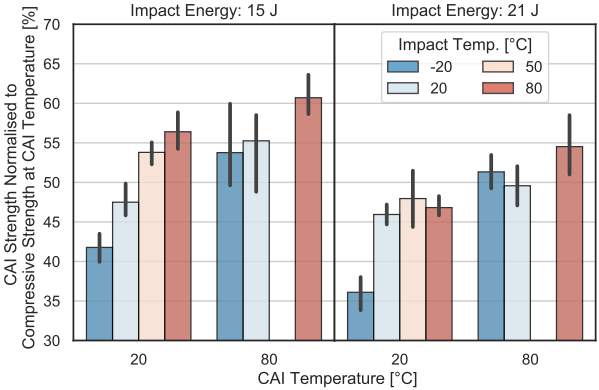

Figure 5.15.: Compressive strength retention after impact normalised to the compressive strength at CAI temperature

The strength retention factor, which denotes the residual strength normalised to the undamaged strength, is an essential parameter for designing structures. Figure 5.15 presents the retention factors, which are normalised to the corresponding CAI temperatures undamaged strength, e.g. the CAI strength determined at 80 °C was normalised to the undamaged strength at 80 °C. At both impact energies, the retention factors are higher at 80 °C. The figure shows that an elevated temperature during compression after impact does not seem to be critical, as the retention factors are higher at elevated temperatures. The decrease in compressive strength compensates for the nominal differences in residual strength, because the undamaged compressive strength of the laminate decreases from 607±36.45 MPa at 20 °C to 421±16 MPa at 80 °C. As mentioned above, the range of residual strengths is narrower at 80 °C, which indicates that the influence of the delamination size decreases. This could be due to an improved load diversion around the impact damage based on the lower modulus of the matrix at increased temperatures, resulting in a lower composite stiffness.

However, the investigation of the strength under temperature influence is not common practise. Therefore, Figure 5.16 shows the retention factor where the residual strength is normalised with the undamaged compressive strength at 20 °C. In this case, it shows that the residual strength is not only determined by the impact damage and the impact parameters but mainly by the temperature at which the residual strength is determined.

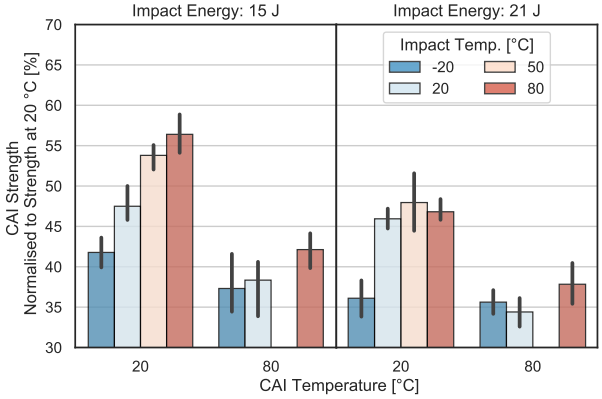

Figure 5.16.: Compressive strength retention of specimens compression tested at 20 °C and 80 °C after impacts normalised to the compressive strength at 20 °C

The importance of ambient temperature when evaluating the residual strength is particularly evident in Figure 5.17. The figure presents the resulting cloud of all tested impact parameters' residual strengths in the relationship of impact and compression temperature. Figure 5.17 highlights the ambient temperature's influence on the resulting compressive strength, as it becomes clear that the temperature during the compression test has a decisive effect on strength.

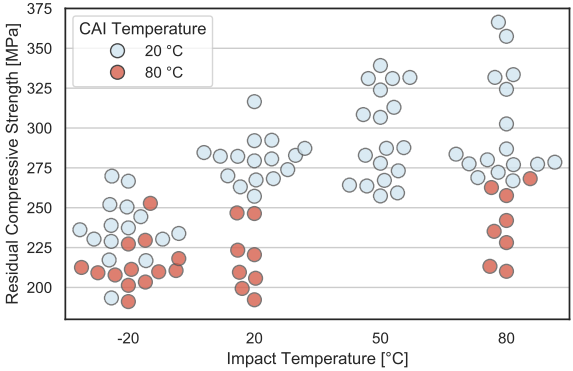

Figure 5.17.: Residual compressive strength of specimens impacted at 15, 18 and 21 J in comparison to impact temperature and CAI temperature (no specimens at 50 °C impact and 80 °C CAI temperature were tested)

The material's requirement sheet of the utilised material for the use in primary aircraft structures [147] states that the average compressive residual strength must not be less than 215 MPa and that the minimal strength must be 195 MPa with 25 J impact energy and hot/wet testing conditions at 70 °C. Despite the lower impact energy, very limited visual detectability of the damage and the dry specimen condition, the tested parameters' residual strengths are in this range and therefore highlight the importance of considering the effect of ambient temperature on damage tolerance.

5.3.2. LVI and Tensile Residual Strength

Because the LVIs in Section 5.3.1 resulted in severe fibre failure in CFRP specimens at elevated temperature, this section investigates the influence of elevated temperatures on LVI and the resulting residual tensile strength at 20 °C. Figure 5.18 summarises the used methods and the order in which the results are discussed. The following section presents the results using graphs for a better overview and comparability. The respective quantitative data is summarised in Appendix B in Section B.2.

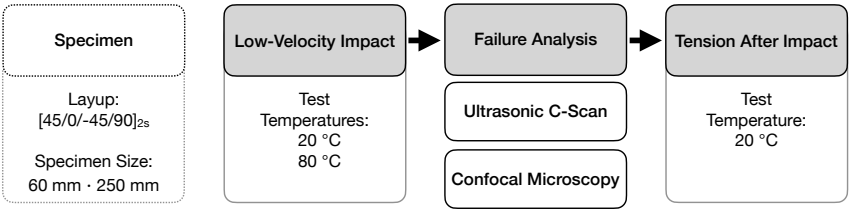

Figure 5.18.: Schematic representation of the test procedure and the analysis methods used to determine the damage after low-velocity impact and the residual tensile strength after impact

The permanent indentation depth (see Figure 5.19) increases with temperature and exhibits a similar behaviour and values as the impact damage of the compressive specimens. When the temperature is increased to 80 °C, the indentation depth is growing by 36 %. The permanent indentation is below the visibility limit of 0.5 mm for all impact parameters tested [124, 167].

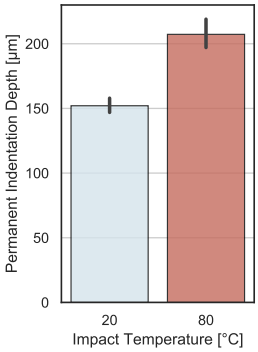

Figure 5.19.: Permanent indentation depth for 25 J impacts on tensile specimens at 20 and 80 °C

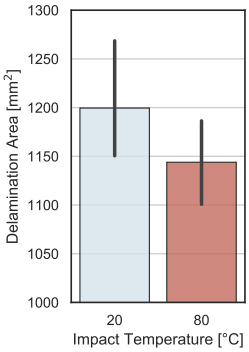

Figure 5.20.: Projected delamination area of tensile specimens for impacts with 25 J at 20 and 80 °C

Figure 5.21 displays confocal microscope pictures of the resulting damage on the specimen's surface from different impact parameters. At 20 °C, the area around the impact only exhibits few matrix cracks and a visible permanent indentation. With increased temperature, fibre failure occurs because the fibres kink under compression during impact. However, the extent of fibre failure shows some scatter, and three out of five specimens exhibited extensive fibre failure at elevated temperature. The occurrence of fibre breakage on the upper side of the sample, despite significantly altered clamping fixture dimensions, affirms that the effect of the occurring fibre failure is partially independent of the utilised fixture.

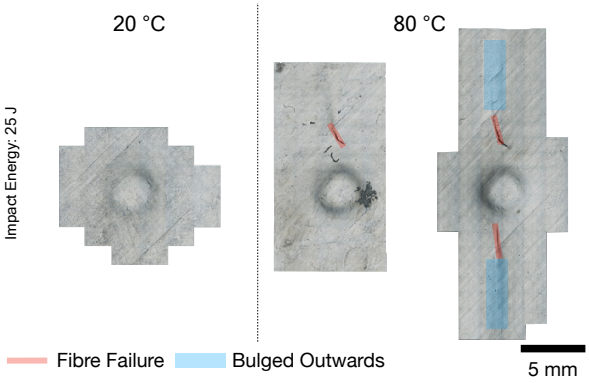

Figure 5.21.: Impact damage on the impacted side of tensile specimens at 20 and 80 °C

Figure 5.20 displays the resulting projected delamination area. It decreases with a temperature rise from 20 to 80 °C. Figure 5.22 displays the C-scan defect echo depth for impacts at 20 and 80 °C in comparison to the sample and fixture size. It is visible that the delamination damage is developing almost over the whole width of the support frame distance, which is often the case for small specimens [159, 165], leading to reduced sensitivity and a higher scatter of the delamination area, as observable in Figure 5.20.

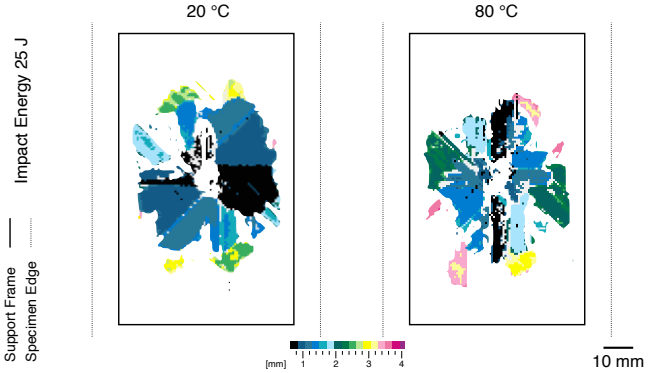

Figure 5.22.: C-scan of the delamination damage after impact

Figure 5.23 displays the resulting residual tensile strength. The strength declines considerably due to the impact damage, but the decrease is not as substantial as LVI's effect on the residual compressive strength (compare with Figure 5.13). The strength is reduced by 11 % from impacts at 20 °C and by 19 % for impacts at 80 °C compared to the undamaged strength.

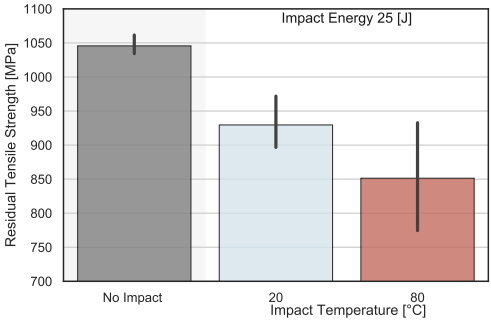

Figure 5.23.: Tensile strength at 20 °C of unimpacted and impacted tensile specimens at 20 and 80 °C impact temperature

Figure 5.24 presents the resulting tensile strength of every tensile test. The strength of the undamaged specimens is exhibiting low scatter. When impacted at 20 °C the scatter increases, which can be explained by the scatter in impact damage size (see Figure 5.20). With increasing temperature, the scatter of the residual strength increases further, ranging from 740 to 950 MPa. This higher variation in residual strength can be accounted for by the change in failure mechanisms and different fibre failure severities (see Figure 5.21). When just taking the lower three specimens into account, which all exhibit extensive fibre failure, the residual strength is reduced by 25 %.

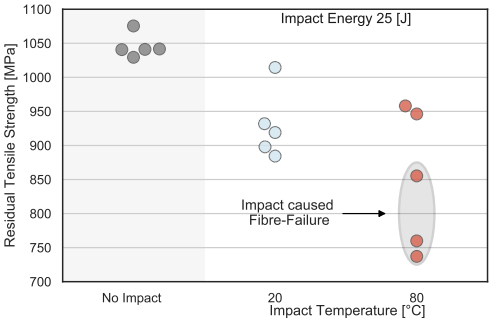

Figure 5.24.: Tensile and residual tensile strength after impact for different impact temperatures

Figure 5.25 presents representative stress-strain curves obtained by DIC measurements during tensile tests. All specimens exhibit a similar stiffness at the beginning of the test. The undamaged and 20 °C impact specimens exhibit linear behaviour until fracture. The sample impacted at 80 °C, which exhibited extensive fibre failure, displays slight nonlinear behaviour, which can be accounted to the fibre failure because the fibre failure facilitates the transverse contraction.

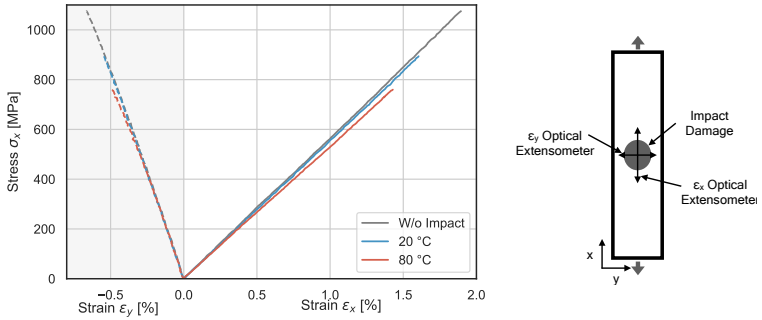

Figure 5.25.: Exemplary tensile stress-strain curves of the tensile tests after impact

5.4. Conclusion

The results illustrate that ambient temperature is a crucial external influencing factor to consider for composite structures, especially for LVI loaded structures and therefore confirm the working hypothesis:

The matrix's mechanical performance decreases with increasing environmental temperature and negatively influences the damage tolerance of the composite.

The presented results show significant sensitivity of the composite's mechanical properties to the ambient temperature. With increasing temperature, the changing matrix properties lead to a change of occurring damage modes resulting from the LVI. The delamination size decreases, while the permanent indentation depth increases and fibre failure occurs on the impacted side. As a result of the changing damage modes, the detectability of the impact damage increases. The change of the occurring damage modes also affects the resulting residual strength of the composite. The fibre failure, resulting from LVIs at elevated ambient temperature, leads to a significant reduction in tensile strength and should be included in damage tolerance consideration.

Concerning the residual compressive strength, the conclusion is not as straight forward. The delamination area and distribution resulting from LVI mainly determine the residual compressive strength. Hence, more severe delamination failure leads to a lower residual compressive strength. This leads to the conclusion that the LVI damage's visual detectability is generally inverse to the severity concerning the residual compressive strength when considering the temperature. For structures impacted at elevated temperatures and compression loaded at room temperature, it could therefore be concluded that the consideration of elevated ambient temperature during LVI is not critical. However, this conclusion shows limited applicability for the operation of composite structures. As a structure is prone to impact loading at elevated temperature, the in-service temperatures are likely to be similar. Thus the residual compressive strength limit could also be reached at elevated temperature. The presented results highlight that this compressive strength limit significantly declines with rising temperature, and therefore, temperature is a critical factor in the residual compressive strength. Especially when considering that, the range of residual compressive strengths resulting from different impact parameters significantly

declines. This means, that the temperature during compressive loading can affect the residual strength more considerably than the impact energy of the LVI and therefore the resulting LVI damage. Also, it must be mentioned here that the temperatures considered are not extreme cases but can occur during normal operation of CFRP structure. Therefore, temperature should be taken into account with regard to damage tolerance, as the present results have shown a significant influence.

Further studies would be of interest here: It would be appealing to investigate the combination of lower temperatures during the impaction and the determination of the residual compressive strength at elevated temperatures. This could be a critical load case based on the given findings. An investigation of other internal and external factors, e.g. the layup, the laminate thickness or specimen size would be of interest. This could lead to an accurate determination of the necessary allowances for damage tolerances and could further contribute to exploit the lightweight potential of composite structures.

6. Simulation of Failure at Elevated Temperatures

The results presented in the previous Chapter 5 attest that the temperature has a decisive influence on impact damage and the resulting residual strength. However, the structural and laminate design determines the damage tolerance to a large extent. As a result, it is hard to generalise the results obtained from coupon level tests. Therefore, a more comprehensive approach is needed to evaluate the influence of temperature on the failure process without applying expensive and time-consuming experimental campaigns. The rise in computers' availability and power over the last decades has been enormous, leading to a significant advancement in science's and engineering's numerical methods, resulting in considerate research activity on the numerical modelling of composites' failure. This chapter aims to utilise a state of the art model for the computational modelling of progressive failure of composite laminates and extend it to incorporate the influence of an elevated operating temperature.

6.1. State of the Art

To design CFRP structures efficiently, safely and to understand the influence of temperature, the numerical simulation of the progressive failure behaviour is necessary. Meso-scale continuum damage based models to describe the progressive failure of CFRP have been a major research focus in the last decades [170–172] and led to high-fidelity simulations of LVI impact damage [173, 174] and CAI load cases [174–176]. It seems evident that the mechanical properties such as stiffness, strength, fracture toughness and interfacial strength depend on the ambient temperature. However, this fact is only partially considered in the literature on continuum damage models. And thus, simulations on a meso-level that take the temperature into account are sparse. Allix [27] published the first study in this field, in which he identified the tensile material behaviour at different temperatures and proposed a temperature-dependent damage and plasticity growth

law. Liu et al. [177] implemented a multi-scale approach to model OHC failure, utilising the modified micro-mechanics-based failure approach. The results were very close to the experimental OHC results. However, in OHC fibre-parallel compressive behaviour mainly determines the strength, the interlaminar properties only have a minor influence in this case, which is in contrast to CAI load cases [119]. To the author's knowledge, the only work which has investigated the temperature dependency of impact damage has been published by Chen [176]. In his work, the failure initiation for longitudinal fibre tensile and compressive loading is handled by the max-strain criterion and the Hashin criterion controls the matrix failure initiation. Damage degradation is handled with strain-based stiffness reduction. Shear non-linearity is modelled with damage and plasticity and the delamination using cohesive elements, with quadratic initiation and energy-based power-law for degradation without temperature-dependency. The material characterisation was performed at 20 °C and only the transverse tensile properties as shear modulus, fibre direction compressive strength and mode I and mode II interlaminar ERR material parameters were determined at 80 °C. He performed impact simulations at 20 °C and 80 °C with hydrothermal aged parameters. The model nicely represents the experimental impact response. However, the result significantly overestimate the delamination area at 80 °C. The residual strength was not investigated.

A comprehensive approach to incorporate the temperature influence on the mechanical properties into CompDam [32], a modern mesoscale CDM model, is presented. The model is then utilised in LVI and CAI simulations and the results are compared to the experimental outcomings from Chapter 5.

6.2. Material Characterisation under Temperature Influence

6.2.1. Materials and Experimental Setup

Temperature-dependent material parameters of Hexply M21/35%/268/T800S (Hexcel, USA) were determined at temperatures between 20 °C and 100 °C. The tests, shown in Table 6.1, are chosen to determine the parameters needed to describe the ply's behaviour within CompDam and the delamination behaviour between the plies.

In composites, temperature-induced stresses are almost inevitable. To determine the temperature at which the thermally induced stresses are minimal, an asymmetric laminate test, as suggested by Cox et al. [156], was utilised. CFRP samples with an asymmetric 0°/90° layup and size of $250 \cdot 250\,\mathrm{mm}^2$ were heated in an oven, and the temperature of the specimens was monitored with thermocouples. To determine the temperature at which no further deformation change occurs, the sample was filmed during this process. This temperature was chosen as the stress-free temperature for the simulation.

Table 6.1.: Summary of the tests performed for simulation input data and the number of specimens per configuration

Test	Longitudinal Tension	Transverse Tension	Longitudinal Compression	Transverse Compression	In-Plane Shear
Layup	$[0]_4$	$[90]_8$	$[0]_8$	$[90]_8$	$[\pm 45]_{2s}$
Specimen thickness [mm]	1	2	2	2	2
Temperature [°C] (No. Specimens)	20 (5)	20(5), 40(5) 60(5), 80(5)	20(4), 50(5) 70(2), 90(2)	20(4), 50(5) 70(5), 90(4) 100(5)	20(4), 40(4) 60(4), 80(4) 100(4)

6.2.2. Experimental Results

Table 6.2 summarises the results from the tensile and compressive tests. The mechanical properties decline considerably, even at relatively moderate temperature increments. E.g. the compressive strength in the fibre direction decreases by 27 % and in transverse direction by 26 % when subjected to temperature increase from 20 to 90 °C.

Table 6.2.: Results of the tensile and compressive tests in a temperature range of 20 °C to 100 °C

			Temperature [°C]							
Description	Name	Unit	20	40	50	60	70	80	90	100
Longitudinal Young's modulus	E_1	GPa	145.89 ±2.94	-	-	-	-	-	-	-
Tensile Strength	X_T	MPa	3136.78 ±59.15	-	-	-	-	-	-	-
Transverse Young's modulus	E_2	GPa	8429.45 ±213.09	7841.74 ±161.78	-	7349.62 ±222.66	-	6921.27 ±314.45	-	-
Transverse Tensile strength	Y_T	MPa	72.84 ±4.53	64.36 ±2.13	-	55.88 ±5.84	-	52.32 ±6.36	-	-
Shear modulus	G_{12}	GPa	4436.90 ±107.66	4207.74 ±197.80	-	3671.28 ±141.16	-	3365.5 ±121.15	-	3280.11 ±103.04
Shear strength	S_L	MPa	62.84 ±1.65	58.11 ±0.57	-	54.34 ±1.675	-	52.17 ±1.94	-	-
Transverse Compressive Strength	Y_C	MPa	189.35 ±7.25	-	172.55 ±2.85	-	152.21 ±4.65	-	140.51 ±1.45	-
Longitudinal Compressive Strength	X_C	MPa	1394.37 ±54.72	-	1270.4 ±25.68	-	1179.55 ±72.35	-	1013.50 ±50.44	-

Figure 6.1 summarises the change of mechanical properties against the reference temperature 20 °C. This graphic illustrates how different and non-linear the parameters change. For example, E_2 shows a reduction of $-13\,\%$ at 60 °C, whereas the strength is already $-23\,\%$ lower. The decrease in properties depends on the loading scenario, which is expected as the matrix's influence proportion varies.

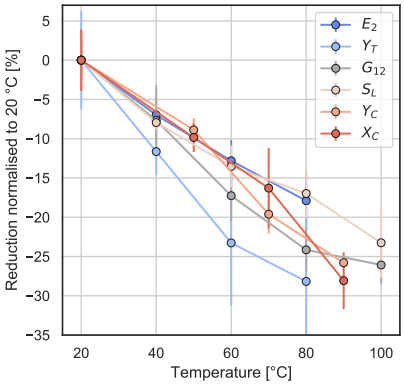

Figure 6.1.: Change of the mechanical properties at different temperature normalised to 20 °C

A change of the delamination behaviour is often accounted to a temperature-induced change of the interlaminar ERR [158, 159]. However, from coupon tests designed to obtain the interlaminar ERR under mode I and mode II loading, no generally applicable conclusion on how temperature influences the ERR can be drawn. Kim et al.[29] and Zhao et al.[154] found that under mode I loading the initiation fracture ERR is slightly reduced with increasing temperature, but the propagation ERR increases. Lee [178] identified the influencing factors for the temperature dependency of the mode I ERR analytically. The resin ERR is defined by the interply thickness, the matrix ERR G_{IC}^{M}, matrix modulus E, yield strength σ_y and the residual thermal stresses. Depending on the resin and fibres used, the interlaminar ERR's temperature dependence under mode I can range from significant to insignificant [29, 154, 179].

Cowley [28] and Russel [155] found that under mode II the ERR rates only decrease slightly with increasing temperature. Hojo et al. [180] found a similar temperature insensitivity for cryogenic temperatures, as only a small difference between ERR at room temperature and −196.15 °C was found. Lee [112, 181] explains the possible inertness of mode II ERR against temperature with the presences of opposing effects. The laminates mode II ERR is determined by the shear strength and the mode I ERR G_{IC} of the resin. With increasing temperature, the shear strength decreases and the G_{IC} of the resin increases. Depending on the resin properties, this can result in a temperature insensitive

interlaminar mode II ERR. The mode II ERR has a more decisive impact on the resulting impact damage and the residual strength than the mode I ERR. [119]. Thus, the more decisive interlaminar ERR exhibits a lower temperature sensitivity.

Chen [176] determined the mode I and mode II ERR for M21/T800s at 20 °C and 80 °C. Neither for mode I initiation ERR nor for the mode II ERR a change was found. Therefore it seems to be a valid assumption that the ERRs are approximately constant for the temperature range and material utilised in this thesis. Table 6.3 shows the critical values for the mode I ERR and the value for mode II ERR.
The determined stress-free temperature from the unbalanced laminates is 171 °C, which is very similar to Giddings et al. [182] who determined the stress-free temperature to 169.9 °C, for M21/T800s with a lower FAW weight.

Table 6.3.: Experimental results for G_{IC} and G_{IIC}

	G_{IC} [J/m^2]		G_{IIC} [J/m^2]
Mode I Fracture Toughness	215.34 ±5.74	Mode II Fracture Toughness	2198.76 ±95.31

6.3. Modelling Approach

This chapter presents an approach to model the temperature-dependent, progressive damage of high-performance composites using a computational CDM model. To achieve this, CompDam [32] was used as a basis. CompDam is a CDM material model implemented as a user-material for the commercial FE programm Abaqus/Explicit. It is a state of the art model for the accurate representation of the mesoscale damage modes in FRP composite materials. It features the deformation gradient decomposition (DGD) proposed by Leone [183], which offers an accurate kinematic representation of matrix cracks and prevents the prediction of spurious secondary failure modes.
The CompDam subroutine is extended by the addition of a module, which integrates the temperature-dependent material behaviour. This means that every integration point's material properties update to the current temperature at the start of each increment. As a result, the model could also be used in a multiphysics simulation where the temperature distribution is not isothermal. The

following section presents the modelling approach and integration of the temperature dependency into equations describing the material behaviour.

6.3.1. Elastic Ply Behaviour

The starting point for the temperature-dependent constitutive model is the elastic behaviour of a single ply. The elastic behaviour is defined by Hooke's law:

$$\bar{\boldsymbol{\sigma}} = \bar{\boldsymbol{D}}^e \bar{\boldsymbol{\varepsilon}} \tag{6.1}$$

where $\bar{\boldsymbol{\sigma}}$ is the material stress vector, $\bar{\boldsymbol{\varepsilon}}$ the material engineering strain vector and $\bar{\boldsymbol{D}}^e$ is the materials elastic stiffness matrix specified below in the compliance formulation for transverse isotropy:

$$\left[\bar{\boldsymbol{D}}^e\right]^{-1} = \begin{bmatrix} \frac{1}{E_1} & -\frac{\nu_{21}}{E_2(T)} & \frac{\nu_{21}}{E_2(T)} & 0 & 0 & 0 \\ -\frac{\nu_{21}}{E_2(T)} & \frac{\nu_{23}}{E_2(T)} & \frac{1}{E_2(T)} & 0 & 0 & 0 \\ -\frac{\nu_{21}}{E_2(T)} & -\frac{\nu_{23}}{E_2(T)} & \frac{1}{G_{23}} & 0 & 0 & 0 \\ 0 & 0 & 0 & \frac{1}{G_{23}} & 0 & 0 \\ 0 & 0 & 0 & 0 & \frac{1}{G_{12}(T)} & 0 \\ 0 & 0 & 0 & 0 & 0 & \frac{1}{G_{12}(T)} \end{bmatrix} \tag{6.2}$$

The temperature is introduced in the ply's matrix dominated properties, namely the transverse modulus E_2 and the in-plane shear modulus G_{12}. The Poisson's ratios are assumed to be constant over the considered temperature range [182]. Transverse isotropy is assumed, therefore G_{23} is indirectly temperature-dependent:

$$G_{23} = \frac{E_2(T)}{2(1+\nu_{23})} \tag{6.3}$$

An interpolation function for each temperature-dependent elastic property controls the temperature dependency. An exponential approach is chosen because the representation is sufficiently accurate.

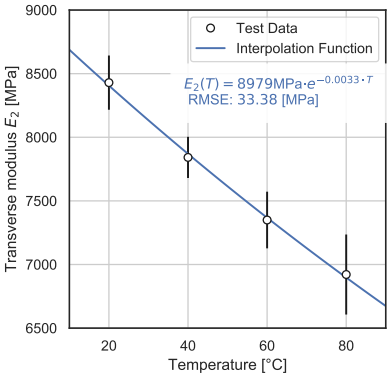

Figure 6.2.: Interpolation function of the transverse modulus E_2 in comparison with test results

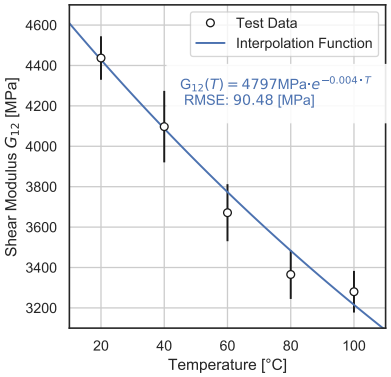

Figure 6.3.: Interpolation function of the shear modulus G_{12} in comparison with test results

The function is steadily decreasing with increasing temperature so that even if temperatures just outside the definition range are chosen, the model is stable. The parameters of the exponential function are fitted to the experimental data using the least squares regression algorithm For the transverse tensile modulus $E_2(T)$ this approach yields into:

$$E_2(T) = 8979\text{MPa} \cdot e^{-0.0033 \cdot T} \tag{6.4}$$

Figure 6.2 shows the interpolated modulus together with the test data and reveals a Root Mean Squared Error (RMSE) of 33.38 MPa compared to the mean data from test results. The RMSE is thereby significantly lower than the standard deviation of the mechanical tests, see Table 6.2. The shear modulus G_{12} is represented with the same base-function:

$$G_{12}(T) = 4797\text{MPa} \cdot e^{-0.004 \cdot T} \tag{6.5}$$

Figure 6.3 shows the corresponding graph and the according RMSE of the function, which is 90.48 MPa.

An essential aspect of the laminate analysis is the consideration of residual stress due to curing at elevated temperatures. The difference in thermal properties of fibre and matrix causes the thermal expansion behaviour of the ply to be orthotropic. When the laminate is cooled, the plies will shrink in the transverse

direction, but this contraction is constrained since they are connected. The transverse tensile stress caused by the mismatch in thermal properties can be significant concerning the transverse tensile strength or the interlaminar shear strength, thus influencing delamination behaviour. Only the in-plane thermal stresses are considered; hence, the linear elastic constitutive law after a temperature change is:

$$\bar{\boldsymbol{\sigma}} = \bar{\boldsymbol{D}}^{\mathrm{e}} \bar{\boldsymbol{\varepsilon}}^{\mathrm{mech}} \tag{6.6}$$

By decomposing the strain total strain $\bar{\boldsymbol{\varepsilon}}$ into a mechanical and a thermal part:

$$\bar{\boldsymbol{\varepsilon}}^{\mathrm{mech}} = \bar{\boldsymbol{\varepsilon}} - \bar{\boldsymbol{\varepsilon}}^{\mathrm{th}} \tag{6.7}$$

the thermal strains are calculated with:

$$\varepsilon^{th} = \begin{bmatrix} \alpha_1 \Delta T & \alpha_2 \Delta T & \alpha_2 \Delta T & 0 & 0 & 0 \end{bmatrix}^T \tag{6.8}$$

where ΔT is the magnitude of the temperature change compared to the stress-free temperature and α_1 and α_2 are the coefficients of thermal expansion in fibre and transverse direction, respectively. The coefficient of thermal expansion can be approximated to be constant in the investigated temperature range [182].

6.3.2. Damage Behaviour

The following section introduces the utilised failure criteria, degradation laws, and the according temperature implementations for the different failure modes.

Fibre Failure

For tensile fibre failure initiation, the non-interacting max-stress criterion is utilised:

$$FI_{\mathrm{F}} = \frac{\sigma_{11}}{X_{\mathrm{T}}} \leq 1 \qquad for \qquad \sigma_{11} > 0 \tag{6.9}$$

The CDM model to represent the tensile fibre damage evolution is based on Maimí et al. [184]. After the initiation of failure, fracture energy based bi-linear softening implemented in CompDam is utilised, which is based on Davila et al. [185]. The compressive damage initiation uses the same model as in tension, but damage initiation is temperature-dependent, which yields in:

$$FI_{\mathrm{C}} = \frac{|\sigma_{11}|}{X_{\mathrm{C}}(T)} \leq 1 \qquad for \qquad \sigma_{11} < 0 \tag{6.10}$$

where the temperature-dependent compressive strength X_C is interpolated by:

$$X_C(T) = 1570.70\text{MPa} \cdot e^{-0.005 \cdot T} \tag{6.11}$$

Figure 6.4 displays the according interpolation function with the associated support points. The longitudinal compression fracture toughness is assumed to be constant. Although the matrix strongly influences failure under compression, the fibres mainly determine the ERR during fracture.

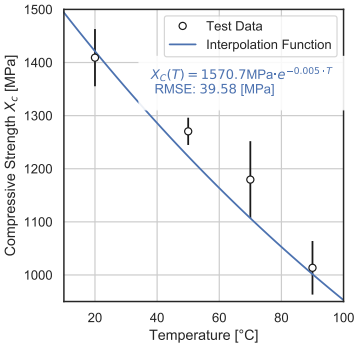

Figure 6.4.: Test results and exponential interpolation function of the compressive strength X_C

Matrix Failure

CompDam [32] utilises the deformation gradient decomposition method proposed by Leone [183]. For tensile and compressive loading, matrix damage is modelled by additive decomposition of the deformation gradient into an undamaged matrix part and a cohesive crack part. Other CDMs, which decompose the strain into a damaged and non-damaged part, exhibit the drawback that the micro-mechanical causes for crack growth in fibre direction are not visible after the material's homogenisation. In this case, failure propagation is governed by stress concentration, thus contradicting the actual material behaviour where matrix cracks are determined by the fibre direction [186].

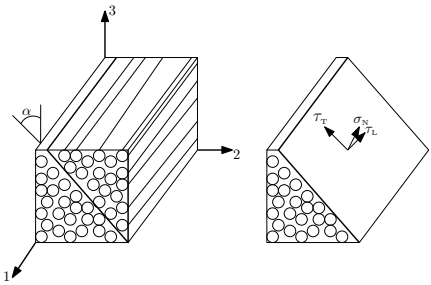

Figure 6.5.: Resulting stresses on the matrix crack plane dependent on the fracture angle

The matrix cracks' normal directions can have any orientation in the 2-3 plane (see Figure 6.5). The crack plane with the highest stress is solved iteratively. Bi-linear cohesive laws are utilised, and the mixed-mode behaviour of matrix damage initiation and evolution is defined according to the Benzeggagh-Kenane law [187]. The implementation of the cohesive-laws in CompDam is similar to Turon et al. [188] and described in detail in that study or in the CompDam code itself [32]. In the following, the changes made to the damage initiation depending on the temperature are shown. The penalty stiffness in the normal direction is calculated by:

$$K_{\mathrm{N}} = m\frac{E_2(T)}{l_0} \tag{6.12}$$

where m is the penalty stiffness multiplier, $E_2(T)$ the temperature dependent transverse modulus (see Equation 6.4) and l_0 the element thickness. The penalty stiffness in longitudinal K_{L} and tangential K_{T} shear direction are defined according to Turon et al. [188]:

$$K_{\mathrm{L}} = K_{\mathrm{N}}\frac{G_{\mathrm{IC}}}{G_{\mathrm{IIC}}}\left(\frac{S_{\mathrm{L}}(T)}{Y_{\mathrm{T}}(T)}\right)^2 \qquad \text{and} \qquad K_{\mathrm{T}} = K_{\mathrm{N}}\frac{G_{\mathrm{IC}}}{G_{\mathrm{IIC}}}\left(\frac{S_{\mathrm{T}}(T)}{Y_{\mathrm{T}}(T)}\right)^2 \tag{6.13}$$

where G_{IC} is the mode I ERR, G_{IIC} the mode II ERR, $S_{\mathrm{L}}(T)$ the temperature-dependent shear strength, $S_{\mathrm{T}}(T)$ the temperature-dependent tangential shear strength and $Y_{\mathrm{T}}(T)$ the temperature-dependent transverse strength.
The displacement jumps in longitudinal Δ_{L} and tangential Δ_{T} direction are combined into a resulting shear displacement jump Δ_{S}:

$$\Delta_{\mathrm{S}} = \sqrt{\Delta_{\mathrm{T}}^2 + \Delta_{\mathrm{L}}^2} \tag{6.14}$$

The combined in-plane shear penalty stiffness is:

$$K_{\mathrm{S}} = \frac{\sqrt{(K_{\mathrm{L}}\Delta_{\mathrm{L}})^2 + (K_{\mathrm{T}}\Delta_{\mathrm{T}})^2}}{\Delta_{\mathrm{s}}} \tag{6.15}$$

The in-plane strengths τ_{L}^0 account for friction on the potential crack surface as proposed in LaRC04 [189]:

$$\tau_{\mathrm{L}}^0 = S_{\mathrm{L}}(T) - \eta_{\mathrm{L}} K_{\mathrm{L}} min(0, \Delta_n) \tag{6.16}$$

where τ_{L}^0 is the resulting strength, η_L the friction coefficient and Δ_n the displacement jump in normal direction. The same equation is used for the tangential strength τ_{T}^0:

$$\tau_{\mathrm{T}}^0 = S_{\mathrm{T}}(T) - \eta_{\mathrm{T}} K_{\mathrm{T}} min(0, \Delta_n) \tag{6.17}$$

The resulting mixed shear strengths are:

$$\tau_{\mathrm{s}}^0 = \frac{K_{\mathrm{S}}}{\sqrt{(K_{\mathrm{L}}\frac{\Delta_{\mathrm{L}}}{\tau_{\mathrm{T}}^0})^2 + (K_{\mathrm{T}}\frac{\Delta_{\mathrm{T}}}{\tau_0^2})^2}} \tag{6.18}$$

The displacement jump $\Delta_{0\mathrm{N}}$ at which in pure mode I failure initiation is determined by:

$$\Delta_{0\mathrm{N}} = \frac{Y_{\mathrm{T}}(T)}{K_{\mathrm{N}}} \tag{6.19}$$

For pure mode II/III the damage initiation displacement jump $\Delta_{0\mathrm{S}}$ is:

$$\Delta_{0\mathrm{S}} = \frac{\tau_{\mathrm{s}}^0}{K_{\mathrm{S}}} \tag{6.20}$$

The mixed-mode damage initiation and propagation are defined according to the Benzeggagh-Kenane law [187], the implementation is shown in CompDam [32]. The above mentioned temperature-dependent parameters are the transverse tensile strength $Y_{\mathrm{T}}(T)$, the longitudinal shear strength $S_{\mathrm{L}}(T)$ and the transverse shear strength $S_{\mathrm{T}}(T)$. The transverse tensile strength Y_{T} is interpolated with:

$$Y_{\mathrm{T}}(T) = 81.28\mathrm{MPa} \cdot e^{-0.0058T} \tag{6.21}$$

and Figure 6.6 shows the interpolation function and the corresponding experimental results. The interpolation function for the shear strength S_{L} is:

$$S_{\mathrm{L}}(T) = 66.393\mathrm{MPa} \cdot e^{-0.003T} \tag{6.22}$$

Figure 6.7 shows the interpolation function together with the experimental results.

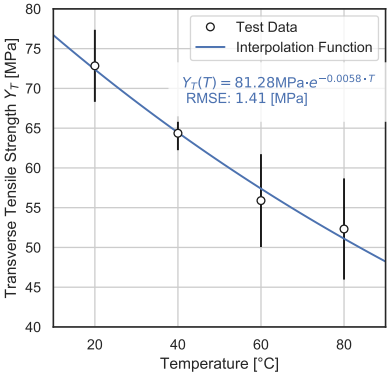

Figure 6.6.: Test results and exponential interpolation function of the transverse tensile strength Y_{T}

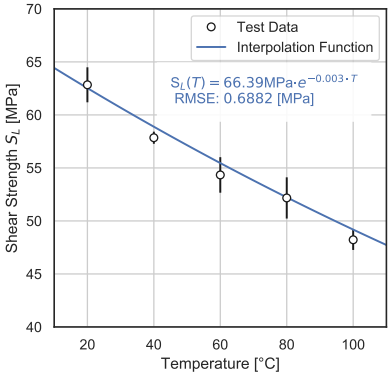

Figure 6.7.: Test results and exponential interpolation function of the in-plane shear strength S_{L}

The shear strength $S_{\mathrm{T}}(T)$ is calculated from the transverse compressive strength $Y_C(T)$ in dependence of α_0, which is the resulting matrix failure angle under pure transverse compression:

$$S_{\mathrm{T}}(T) = Y_{\mathrm{C}}(T) \left(cos(\alpha_0) + \frac{cos(\alpha_0)}{tan(2\alpha_0)} \right) \tag{6.23}$$

$Y_{\mathrm{C}}(T)$ was determined in mechanical testing and is interpolated with:

$$Y_{\mathrm{C}}(T) = 212\text{MPa} \cdot e^{-0.005T} \tag{6.24}$$

Figure 6.8 shows the graphical representation of the interpolation function together with the experimental results.

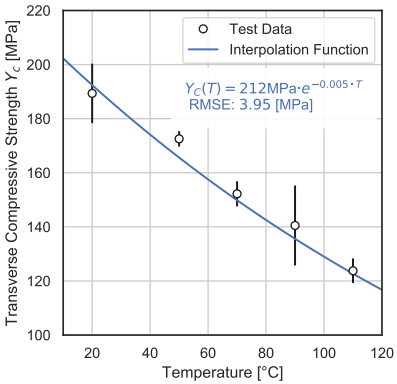

Figure 6.8.: Interpolation function of the transverse compressive strength Y_C in comparison with test results

6.3.3. Non-Linear Shear Behaviour

The non-linear shear behaviour in the 1-2 and 2-3 plane is represented by the Ramberg-Osgood (RO) equation [190]:

$$\gamma_{12} = \frac{\tau_{12} + \alpha_{\text{PL}} sign(\tau_{12}) |\tau_{12}|^{n_{\text{PL}}}}{G_{12}} \tag{6.25}$$

where γ_{12} is the in-plane shear strain, τ_{12} the according shear stress, α_{PL} and n_{PL} are the RO-parameter and fully define the non-linear shear behaviour. Before the initiation of matrix damage, the non-linear shear response is plastic. The parameters α_{PL} and n_{PL} are material and therefore temperature-dependent, because the shear properties are highly temperature-dependent, see Table 6.2. All experimental stress-strain curves obtained at one temperature were combined into a single master curve. The Ramberg-Osgood parameters were then fitted using the corresponding master curve at each temperature. Figure 6.9 and Figure 6.10 display the resulting parameters as well as the support points.

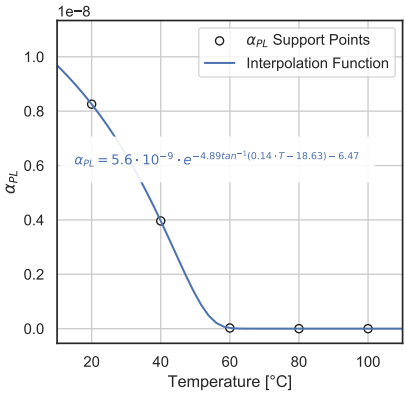

Figure 6.9.: Interpolation function for the temperature dependent RO parameter α_{PL}

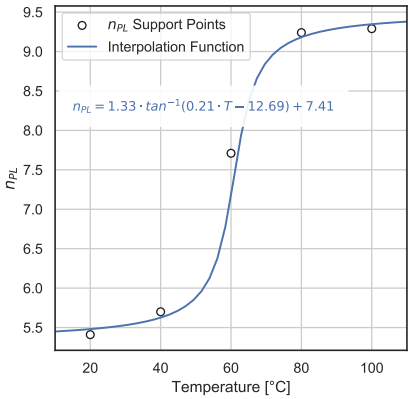

Figure 6.10.: Interpolation function for the temperature-dependent RO parameter n_{PL}

The shape of α_{PL} and n_{PL} can be represented by arctan and arccotangent functions, respectively. These interpolation functions were fitted to the support points and the resulting function for $\alpha_{\mathrm{PL}}(T)$ is:

$$\alpha_{\mathrm{PL}}(T) = 5.6 \cdot 10^{-9} \cdot e^{-4.89 \cdot tan^{-1}(0.14 \cdot T - 18.63) - 6.47} \tag{6.26}$$

and is shown in Figure 6.9. The resulting arccotangent function for $n_{\mathrm{PL}}(T)$ is:

$$n_{\mathrm{PL}}(T) = 1.33 \cdot tan^{-1}(0.21 \cdot T - 12.69) + 7.41 \tag{6.27}$$

and displayed in Figure 6.10. The resulting temperature-dependent representation of the RO-equation is:

$$\gamma_{12} = \frac{\tau_{12} + \alpha_{\mathrm{PL}(T)} sign(\tau_{12}) |\tau_{12}|^{n_{\mathrm{PL}}(T)}}{G_{12}(T)} \tag{6.28}$$

The resulting temperature-dependent shear-stress τ_{12} against shear-strain γ_{12} curves in comparison with the master curves resulting from the mechanical tests are shown in Figure 6.11 and display a good agreement.

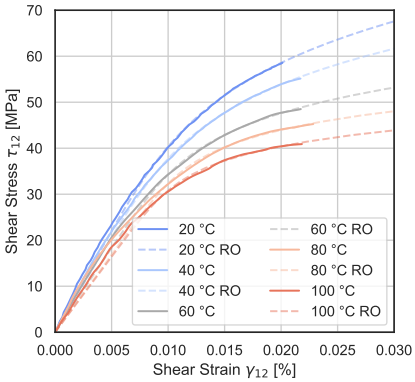

Figure 6.11.: Comparison between the experimental and by temperature-dependent Ramberg-Osgood parameters represented shear curves

6.3.4. Delamination Behaviour

Accurate failure simulation of composite laminates requires not only the prediction of intralaminar damage but also the prediction of delamination onset and propagation. The most common approaches are the use of cohesive elements or contacts with cohesive behaviour. Interlaminar delamination behaviour is modelled using the cohesive contact implemented in Abaqus/Explicit with a temperature-dependent quadratic stress initiation criterion and temperature-independent energy-based degradation. Damage initiates if:

$$\left(\frac{\langle t_\mathrm{n}\rangle}{t_\mathrm{n}^0(T)}\right)^2 + \left(\frac{t_\mathrm{l}}{t_\mathrm{l}^0(T)}\right)^2 + \left(\frac{t_\mathrm{t}}{t_\mathrm{t}^0(T)}\right)^2 \geq 1 \tag{6.29}$$

where t_n is the traction in normal direction, $t_\mathrm{n}^0(T)$ the normal (mode I) interface strength, t_l the traction and t_l^0 the interface strength under mode II, t_t the traction and t_t^0 the interface strength under mode III . However, $t_\mathrm{l}^0 = t_\mathrm{t}^0$ is assumed. The experimental results for 20 °C are used to adapt the interfacial strength for the cohesive damage initiation which results in an interface strength t_n of 25 MPa for mode I and for t_t of 35 MPa in mode II, for the used mesh size. In order to introduce temperature dependency the mode I initiation stress was coupled to the relative temperature dependency of the transverse tensile

strength (see Equation 6.21). This coupling results in the following interpolation function:

$$t_{\mathrm{n}^0}(T) = 28.1\mathrm{MPa} \cdot e^{-0.0058T} \tag{6.30}$$

This coupling is based on the fact that the damage initiation is directly related to the corresponding matrix dominated strength. The mode II/III strength was scaled accordingly with the relative temperature dependency of the shear strength S_t, which results in the following interpolation function:

$$t_{\mathrm{s}^0}(T) = 38.7\mathrm{MPa} \cdot e^{-0.005T} \tag{6.31}$$

The resulting delamination initiation in comparison to the temperature are shown in Figure 6.12. The temperature independent degradation is handled by the Benzeggagh-Kenane Law [187], as implemented in Abaqus/explicit.

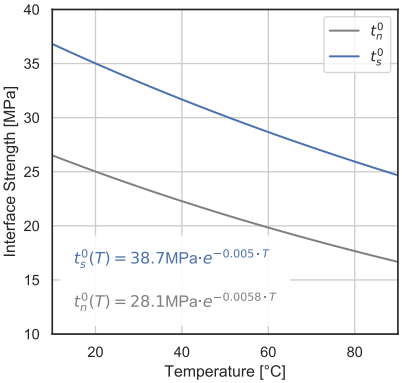

Figure 6.12.: Mode I interface strength t_{n}^0 and mode II/III t_{s}^0 interface strengths over temperature

6.3.5. Temperature Independent Parameters

Table 6.4 summarises parameters chosen to be temperature independent. The data is either from own testing, from literature, or approximated from other material characterisations.

Table 6.4.: Temperature independent material parameters used for the numerical simulations

Symbol	Name	Parameter	Unit	Source
E_1	Longitudinal young's modulus	145888.85	MPa	-
ν_{12}	Major poisson's ratio	0.32	-	[191]
ν_{23}	Minor poisson's ratio	0.48	-	[191]
G_{IC}	Mode I fracture toughness	0.25	N/mm	-
G_{IIC}	Mode II fracture toughness	2.2	N/mm	-
η	Benzeggagh-Kenane exponent	1.63	-	[32]
α_0	Fracture plane angle for pure trans. comp.	0.925	Rad	-
α_{11}	Coefficient of long. thermal expansion	$-0.9e^{-7}$	K^{-1}	[182]
α_{22}	Coefficient of trans. thermal expansion	$2.65e^{-5}$	K^{-1}	[182]
f_{XT}	Long. tensile strength ratio	0.4	-	[191]
G_{XT}	Long. tensile fracture toughness	230	N/mm	[168]
f_{GXT}	Long. tensile fracture toughness ratio	0.5	-	[32]
f_{XTC}	Long. compression strength ratio	0.6	-	[191]
G_{XC}	Long. compression fracture toughness	47.5	N/mm	[168]
f_{GXC}	Long. compression fracture toughness ratio	0.375	-	[32]
μ	Coefficient of friction	0.3	-	-

6.4. Failure Initiation Prediction

Temperature-dependent failure envelopes were created using the presented model. Single element simulations in the temperature range of 20 °C to 85 °C with different load ratios were performed. Figure 6.13 shows the failure initiation in the σ_{11} and σ_{22} stress plane. Every dot presents a damage-initiation under the indicated stress state, obtained from a single-element simulation. The lines indicate the failure body, which results from the failure criteria. The figure shows, that with increasing temperature, the possible design space in which no damage initiates decreases significantly. For transverse loading in the σ_{22} direction, the absolute strength change is more severe for compressive loads than for tensile loading. The predicted failure stresses initiated under pure σ_{11} and σ_{22} loading comply with the test data presented in Table 6.2.

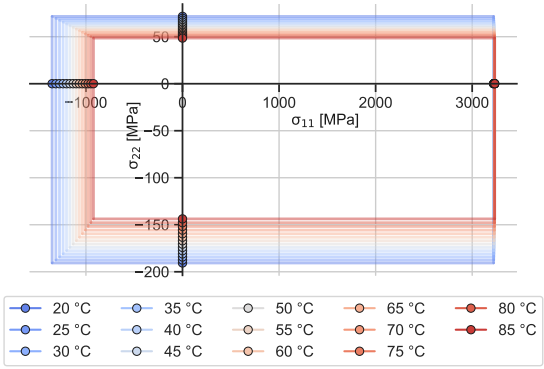

Figure 6.13.: Failure initiation curve in the σ_{11}/σ_{22} plane

Figure 6.14 displays failure initiation in the σ_{22} and τ_{12} stress plane. A strong temperature dependency for all loading ratios is visible. However, the initiation in τ_{12} direction is less affected by temperature, and thus, the most critical decrease in strength is present when the loading ratio is dominated by σ_{22}. Also here, the predicted failure stresses initiated at single σ_{12} and σ_{22} loading comply with the test data presented in Table 6.2. Overall, the results form a consistent failure envelopes over the observed temperatures.

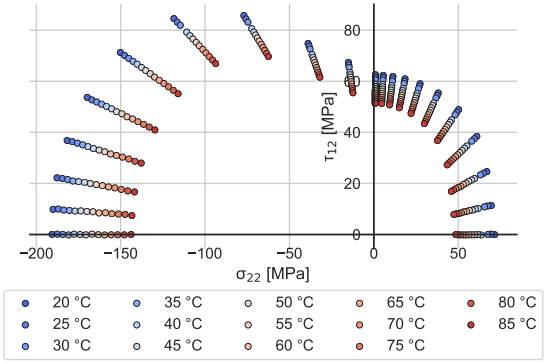

Figure 6.14.: Failure initiation curve in the τ_{12}/σ_{22} plane

6.4.1. LVI and CAI Simulation Setup

Figure 6.15 shows the simulation model setup used for the LVI and CAI simulations. The LVI setup is modelled following the setup used for the experiments (see Section 2.1.4 and Section 2.1.4). The layup is $[45/90/-45/0]_{2s}$ and the individual ply thickness is 0.265 mm. Every ply is meshed with reduced-integration C3D8R elements with an edge length of 1 mm in the in-plane direction. Between every ply, except the middle ply, cohesive contacts, as described above, are utilised. The hemispherical impactor has a diameter of 20 mm and is meshed with rigid elements (R3D4 and R3D3) with a maximum element length of 0.5 mm. The degrees of freedom in x- and y-direction are fixed. The weight and an initial velocity in the z-direction are assigned to the impactor. The values are chosen according to the experimental values used in Chapter 5 (compare Table 5.1 and Table 6.5). The support frame has a rectangular 125 mm by 75 mm cutout and is meshed with R3D3 and R3D4 rigid elements with a maximum element size of 1 mm, all degrees of freedom are fixed. Four clamps restrain the specimen during the impact. The clamps are circle-shaped with a diameter of 14 mm and meshed with R3D3 and R3D4 rigid elements. They are constrained in x- and y-direction and loaded with a constant force of 250 N each in the z-direction. Contact is modelled using the general contact algorithm from Abaqus/Explicit. Any possible new contact throughout the simulation is taken into account. Friction is considered between all the contacting surfaces using the Abaqus/Explicit built-in Coulomb friction model. During impact, mass-scaling was kept below 2 %.

The compression after impact test is based on the fixture used in the experiments (see Section 2.1.4). During compression, the specimen is fully fixed on the lower side, while a displacement is prescribed on the top side of the specimen. The support-knives are meshed with R3D3 and R3D4 rigid elements with a edge length of 1 mm and are fully fixed. For the compression test, mass-scaling was kept below 4 %.

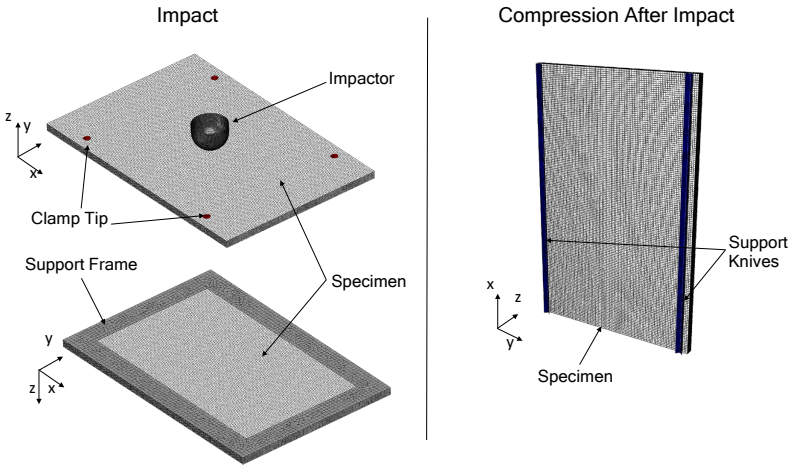

Figure 6.15.: Set-up of the FE models for the low-velocity impact and compression after impact simulations

Table 6.5.: Impaction parameters for the LVI

Impact Energy [J]	Impactor Mass [kg]	Drop Height [mm]	Impact Velocity [mm/s]	Impactor Diameter [mm]
15	4.45	340	2600	20
21	5.47	390	2770	20

6.5. Results and Discussion

6.5.1. Low-Velocity Impact

In the following section, the results of the FE simulation are presented and discussed. The experimental results used for comparison are taken from Chapter 5. Figure 6.16 and 6.17 display the contact force vs. time curve of the impact compared to exemplary experimental results. The higher smoothness of the experimental curves can be attributed to additional post-processing by the drop-tower software. The simulation predicts the impactor contact time accurately for all temperatures at 15 J impaction energy. At 20 °C and 80 °C the maximum force is corresponding to the experimental results.

The simulation results at 50 °C fit appropriately between the results from 20 °C and 80 °C, as the maximum force is right between the other temperatures, which is to be expected with a reduction in bending stiffness due to the temperature increase. However, the experimental results are not met for these parameters.

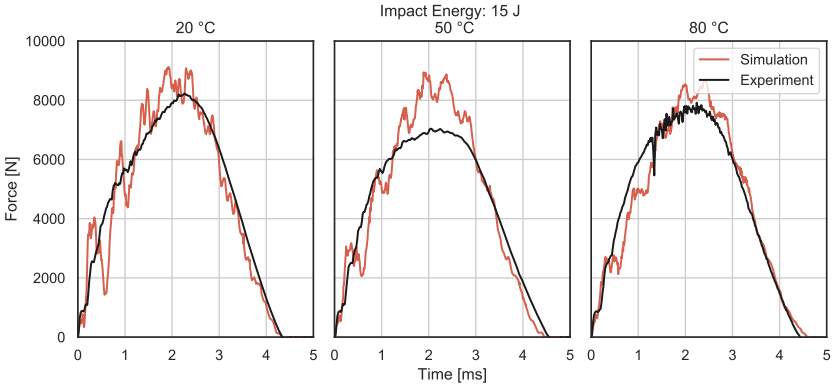

Figure 6.16.: Comparison between the force-time curves of representative test results and the simulations with 15 J at 20 °C, 50 °C and 80 °C

At 21 J impact energy, the impact response resembles the experimental results adequately for all impact temperatures. The initial slope of the curve is well represented, indicating that the obtained stiffness parameters fit well.

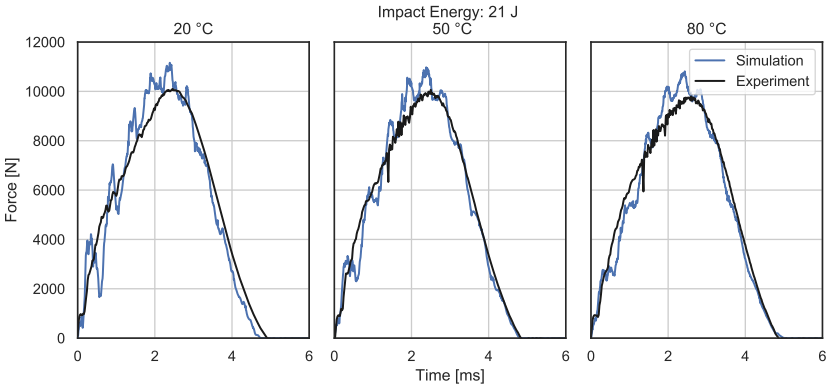

Figure 6.17.: Comparison between the force-time curves of representative test results and the simulations with 21 J at 20 °C, 50 °C and 80 °C

The most recognisable change in damage modes with increasing temperature in the experiments is fibre compression failure on the top ply of the specimen. Figure 6.18 displays the fibre-failure compression failure variable F_{IC} of the upper 45° ply of a 15 J and 80 °C impact during the impact. Fibre failure initiates at a contact time of 1.54 ms and then propagates further until the maximum force, and correspondingly deflection is reached at 2.1 ms.

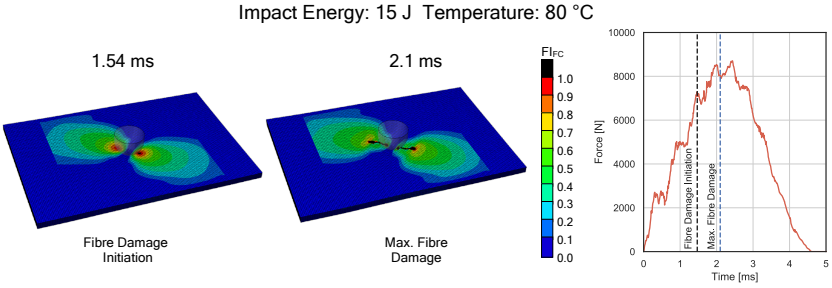

Figure 6.18.: Contour plot of the fibre compression failure variable F_{IC} at fibre damage initiation and when full fibre damage is reached

An explanation is the change of the structural response with increasing temperature. Figure 6.19 displays the deflection of the top ply along the specimen's

short side through the impact point. The figure compares the deformation of simulations with 15 J impact energies at 20 °C and 80 °C. Before fibre failure initiation, at 0.7 ms the maximum z-displacement is almost equal between the two temperatures. Still, the deformation behaviour at 80 °C is more localised. At the sample edges, the 20 °C specimen exhibits more displacement and a non-linear deformation up to where contact of the impactor deforms the laminate, whereas at 80 °C, the specimen's surface is straight up to the area at or near the impactor. The reduced transverse and shear stiffness cause this behaviour (see Figure 6.2 and 6.3). At 1.54 ms the fibre failure is initiated at 80 °C (see Figure 6.18), which leads to an unsymmetrical deformation compared to 20 °C. The maximum z-displacement is larger at 80 °C. At 2.1 ms the fibre failure reaches its saturation. The deflection of the impact at elevated temperature is considerably higher and the shape of the displacement path reflects the more symmetric fibre damage.

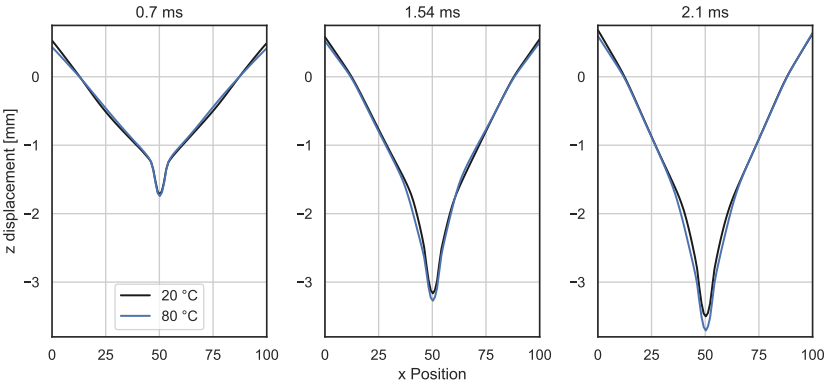

Figure 6.19.: Comparison of the z-displacement of a surface path through the middle of the specimen

Figure 6.20 displays the fibre-compressive degradation parameter $D_{1C} > 0.99$ after the impact compared to microscopy pictures of representative specimens. At 15 J impaction energy fibre failure only occurs at 80 °C. The fact that the compressive fibre damage visible in the experiment does not initiate in the simulation at 50 °C can be accounted to different reasons. One could be that the max-stress initiation criterion is overestimating the compressive strength, as it

is not taking into account the actual occurring failure mode. Nevertheless, the accuracy of size and location of the fibre failure resembles the experimental results sufficiently. At 21 J the model does not predict minor fibre failure at 20 °C, but matches the experimental results at 50 °C and 80 °C.

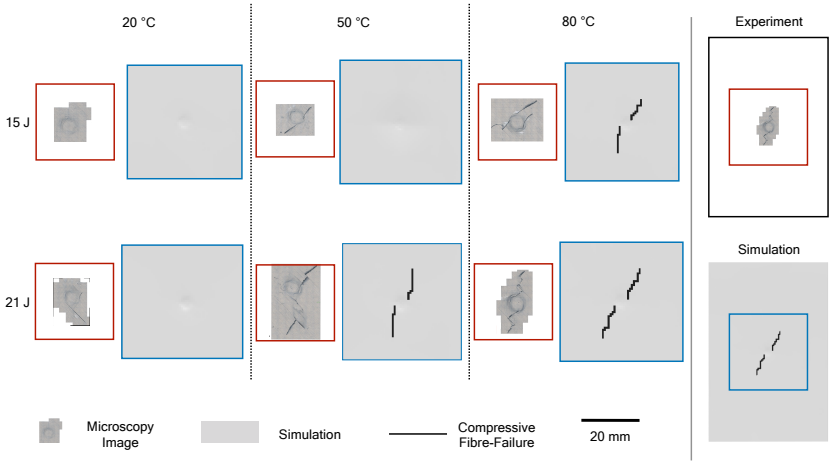

Figure 6.20.: Comparison of the resulting LVI fibre failure on the impact side between a representative sample and simulation

Table 6.6 presents the resulting permanent indentation depth after impact resulting from the experiments and the simulations. The deviation between numerical and experimental results ranges from −9 to 7 %. The simulation results reflect the findings from the experimental campaign. The implementation of temperature leads to an ambiguous mapping between impaction energy and impact depth, which is complicating damage assessment. It must be remarked that the permanent indentation depth is well below the visibility limit of 0.5 mm [124, 167].

Table 6.6.: Permanent indentation depth resulting from the LVI damage

Impact Energy [J]	Impact Temperature [°C]	Permanent Indentation Depth [μm] (Experiment)	Permanent Indentation Depth [μm] (Simulation)	Deviation Simulation/ Experiment [%]
15	20	108.60 ± 8.72	111.00	-2
15	50	103.99 ± 6.13	112.96	-9
15	80	130.29 ± 5.70	138.44	-6
21	20	134.28 ± 7.85	139.00	-4
21	50	151.20 ± 8.13	140.42	7
21	80	171.57 ± 3.92	162.40	5

Figure 6.21 presents the delamination damage derived from the cohesive contact interface. The picture shows all interface damage with a damage variable $D_{\mathrm{COH}} > 0.95$ combined with the experimental delamination outline derived from C-scans. In general, the simulation is predicting the delamination area well and follows the patterns observed in the experiments. Two major effects are visible: The delamination damage reduces in the specimen's upper interfaces with increasing temperature and the projected delamination area decreases. However, at elevated temperatures, the delamination area in interface seven, located below the middle ply, is over-predicted for all temperatures.

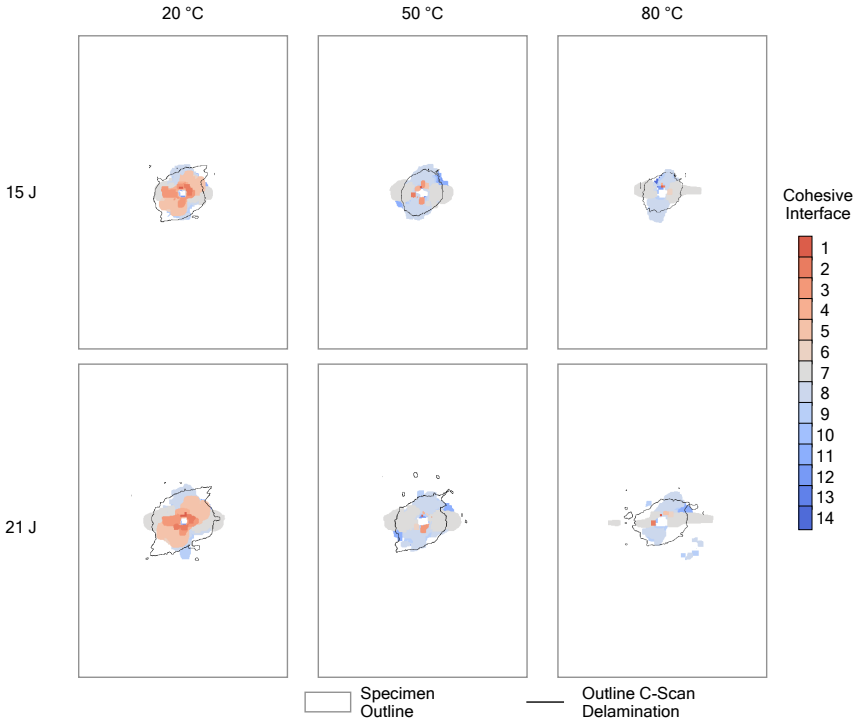

Figure 6.21.: Delamination damage in the individual interfaces resulting from the simulation compared to the projected delamination area of a representative specimen

Table 6.7 summarises the delamination area in comparison to the experimental results. The data confirms the good agreement and temperature-dependent changes observed in Figure 6.21. At elevated temperatures and 15 J the delamination area is slightly over-predicted. This over-prediction is mainly caused by the over-estimation of the delamination in interface seven.

Table 6.7.: Comparison between the projected delamination area from experiment and simulation

Impact Energy [J]	Impact Temperature [°C]	Delamination Area [mm^2] (Experiment)	Delamination Area [mm^2] (Simulation)	Deviation Simulation/ Experiment [%]
15	20	475.73 ± 39.78	441.01	-7
15	50	286.02 ± 18.45	370.24	29
15	80	263.33 ± 26.73	323.71	23
21	20	707.21 ± 48.82	647.48	-8
21	50	567.14 ± 98.40	556.81	-2
21	80	432.56 ± 27.49	409.86	-5

Figure 6.22 displays the matrix damage variable $D_{\mathbf{Matrix}} > 0.99$ on a cut through the middle of the laminat, compared to micro-sections of specimens at the same position. An increase in impaction energy from 15 J to 21 J at 20 °C leads to more matrix damage in the plies above the middle plies and the lowest 0° and 45° plies. Generally, the damage distribution between simulation and experiments is in good agreement. A temperature increase to 80 °C at 15 J leads to a more localised matrix damage, which corresponds to the likewise more localised deformation observed in Figure 6.18.
Additionally, the delamination damage is marked in the micro-sections in Figure 6.22. Here the change observed in Figure 6.7 is visible, too. With increasing temperature the delamination distribution in the specimens follows the changes observed in the simulation. Due to the more localised deformation and damage around the impactor, the interlaminar stresses are not sufficient enough to further progress the delamination in the upper half of the laminate. The same is the case for 21 J, here the amount of matrix damage increases considerably at 80 °C.

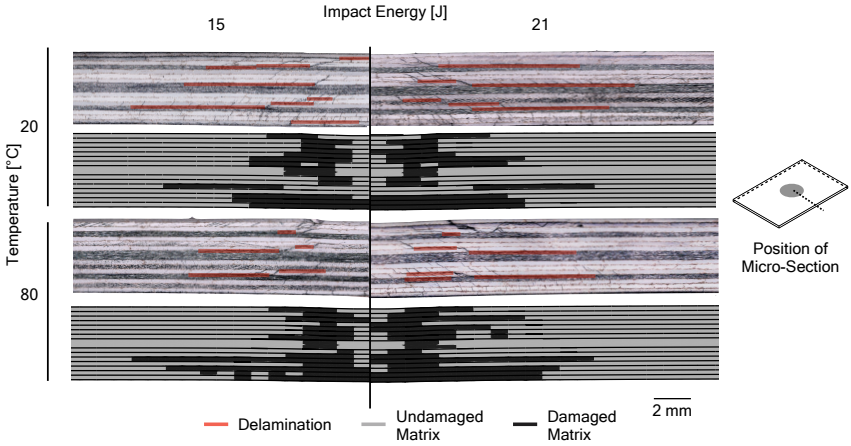

Figure 6.22.: Matrix damage variable $D_{\mathbf{Matrix}} > 0.99$ and micro-section of experimental specimen after low-velocity impact

The presented results display how the failure behaviour and occurring failure modes change with increasing temperature. At higher temperatures, the deformation is initially more concentrated around the impactor. The reason is the reduced stiffness in E_2 and G_{12} direction. The localised deformation in combination with lower strengths of matrix dominated properties (see Figure 6.14), leads to a significantly more localised matrix damage. As a result, the localised damage is preventing a more extensive delamination spread, despite the reduced delamination initiation stresses. Additionally, the localised deformation and the strongly reduced fibre compressive failure leads to severe fibre failure on the impact side. The assumption that the interlaminar ERR remains constant in mode I and mode II seems to be a suitable assumption for the used materials. Also the neglect of visco-elastic effects, which are intensified with increasing temperature [157], seems to be permissible for LVI in the observed parameter range.

6.5.2. Compression After Impact

The challenges in modelling the residual strength after impact are numerous, due to the multitude of influencing factors. Not only the material models and the FE model set-up of the CAI simulation are essential, but also the representation of the impact damage is crucial. The permanent deformation and in

particular, the delamination size and distribution througout the laminate have a dominant influence on the residual strength [129]. Additionally, CAI strength tests are sensitive to deviations in clamping and alignment, which is challenging to represent in the FE model.

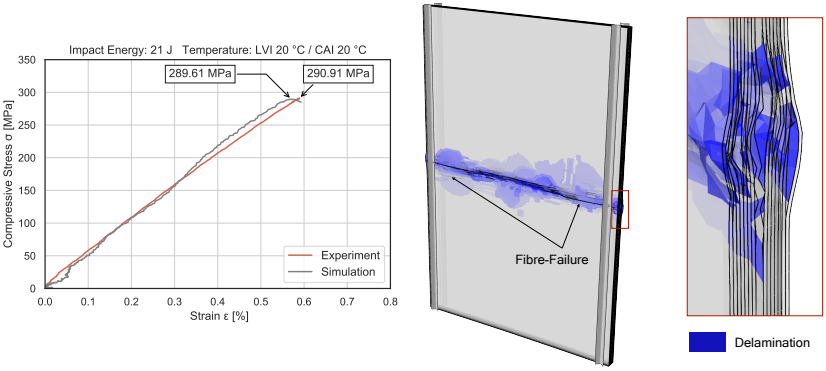

Figure 6.23.: Comparison between the stress-strain curve derived from an exemplary experimental compression test and simulation results

Figure 6.23 displays a representative stress-strain curve of a CAI experiment and the simulation performed. The figure compares an 80 mm long optical extensometer, derived from DIC data to the strain calculated from the displacement of two nodes with a similar distance. The FE simulation displays a very similar strength and stiffness. Also shown is the final failure of the laminate. The occurring damage modes and the delaminations show realistic behaviour.

Table 6.8 summarises the CAI simulations results compared to the experimental results. In general, the simulation shows a good agreement with the experiments and can predict the temperature-dependent ultimate failure stress. However, the strength is overestimated or underestimated at different temperature/energy combinations due to the complex interaction of the influencing parameters. The major influencing parameters are the impact damage prediction, the material parameters and the damage models used. These influencing parameters can add up or balance each other out, as this happens in a non-linear way, the strength can be under-/or overestimated.

For further discussion, the following notation is used: 20/80 °C. The first number denotes the temperature during impact, and the second the temperature during compression. The simulation results at 20/20 °C for 15 and 21 J show

only a slight difference to the experimental results of 7 and 4 % respectively, which is within the standard deviation of the experimental results. The residual strength of impact with 15 J at 50/20 °C and 80/20 °C underestimate the strength. The main reason is the slightly exaggerated delamination area, see Table 6.7 and Figure 6.21. At 21 J and 50/20 °C the prediction is in good agreement as the deviation is included inside the standard deviation of the experimental results. At 80/20 °C the strength is underestimated which can be explained by the over-predicted delamination size in the x-direction, see Figure 6.21. When the temperature during compression testing increases, the strength is generally overestimated.

Table 6.8.: Results of the CAI strength simulation in comparison to experimental results

Impact Energy [J]	Impact Temperature [°C]	CAI Temperature [°C]	CAI Strength [MPa] (Experiment)	CAI Strength [MPa] (Simulation)	Deviation Simulation/ Experiment [%]
15	20	20	288.56 ± 14.64	309.49	7
15	20	80	232.97 ± 19.23	244.49	5
15	50	20	326.84 ± 10.41	299.53	-9
15	80	80	255.95 ± 10.77	269.99	5
15	80	20	326.84 ± 10.41	299.53	-11
21	20	20	279.11 ± 8.96	289.61	4
21	20	80	209.05 ± 11.94	235.69	11
21	50	20	285.38 ± 10.41	285.38	-2
21	80	80	229.87 ± 18.83	236.28	3
21	80	20	284.41 ± 9.32	262.44	-8

Figure 6.24 highlights the importance of temperature during compressive loading. Here the results from Table 6.8 and Table 6.7 are summarised in dependence of the temperature during the compressive loading. When just taking the residual strength at 20 °C into account, the CAI strength decreases with increasing delamination area. The difference in residual strength at similar projected delamination areas are due to scattering and changing delamination distribution, as explained above. The numerical model is representing the experimental results nicely.

Nevertheless, the CAI strength decreases heavily with the increase of temperature to 80 °C. The lowest projected delamination area at 80 °C leads to a similar residual strength as the most extensive area at 20 °C. The simulation is covering the substantial decrease in residual strength, which highlights the capability of

the proposed model.

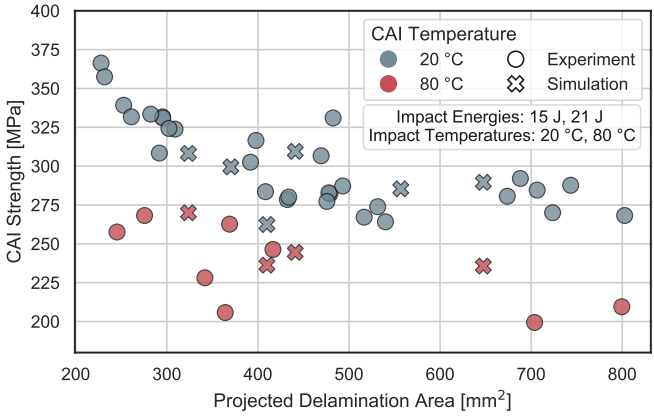

Figure 6.24.: CAI strength and the projected delamination of all experimental and simulation results in dependence of temperature, neglecting the impaction parameters

6.6. Conclusion

When the presented model and the obtained result from the simulation is considered in the context of the working hypothesis:

The matrix's mechanical performance decreases with increasing environmental temperature and negatively influences the damage tolerance of the composite.

The same as in Chapter 5 holds true, because the simulation covers the same effects. However, the model offers insight on how the changed mechanical properties influence the occurring damage.

The characterisation of the mechanical properties of M21/T800s at different temperatures reveals and quantifies the mechanical properties' temperature dependency. Using the obtained material parameter, the CDM model showed that it could predict the occurring damage with the obtained material parameters. The LVI simulation results agree with the experimental results, as the simulation predicts the resulting failure modes and their change due to a temperature

increase, as observed in the experiments. The results show that the interlaminar fracture toughness is not or only very slightly influenced by temperature for this material. In contrast, the initiation of cohesive failure initiation depends on temperature. Thus, the change in structural response and intralaminar damage is causing the smaller delamination at elevated temperature and not an increase in interlaminar ERR.

The CAI simulation covers the dominant influence of temperature on the residual strength. The proposed model proves that it is suitable to investigate and optimise other CFRP structures' elevated temperature behaviour. An extension of the model could further increase its capabilities. For example, the material characterisation, and thus the CDM, could be extended to include low temperatures. With this addition, the potentially most critical load cases concerning could be evaluated: LVI at low temperature and CAI at elevated temperature. Additionally, DCB and ENF tests at different temperature could be performed to validate the assumption that damage initiation decreases with temperature and is linked to matrix strength. The same applies to ERRs for fibre-parallel tension and compression. Also, the adaptation of the model to a more powerful compressive strength criterion could further improve the model's properties.

7. Summary and Conclusion

The presented results contribute to the improvement and further understanding of the damage tolerance of high-performance composites. Based on the results obtained the research hypothesis is confirmed:

Understanding and adapting the matrix's damage behaviour is fundamental to improve the damage tolerance of high-performance composites.

The results clearly highlight the importance of the matrix's damage behaviour concerning the composite's damage tolerance performance. The thesis covers two different aspects, as stated in the hypothesis. The first part focuses on different approaches to influence the matrix's damage behaviour to improve high-performance composites' damage tolerance. The second part investigates the damage tolerance of composites under the influence of temperature, as the matrix's mechanical properties are strongly temperature-dependent.

The first approach to adapt the matrix's damage behaviour investigated the ply thickness's influence combined with a matrix modification with FLG on the occurring matrix damage and CFRP's resulting failure behaviour. The presented results confirm the research hypothesis that the adaption of the matrix failure strongly affects and can increase the damage tolerance of composites. The results point out that FLGs are an effective filler material and increase the interlaminar fracture toughness significantly by adding additional damage modes at low filler content levels. The reduction of ply thickness suppresses matrix damage and thereby decreases the notched specimen's strength. However, the matrix damage initiation stress increases. Hence, thin-ply laminates can still achieve higher allowable stress levels without matrix damage than notched thick-ply laminates. The FLG matrix modification increases the matrix damage initiation stress for all ply thicknesses and, thereby, significantly raises the damage

tolerance of notched laminates. For ultra-thin laminates, the FLG matrix modification reduces stress concentration by initiating micro-cracks in the particles before ultimate failure, leading to a higher ultimate notched strength. Based on the results, the FLG matrix modification for all ply thicknesses is beneficial for the notched samples' performance. The compressive strength of QI-laminates significantly increases by reducing the ply thickness and by adding the FLGs to the matrix. The FLG matrix modification leads to a reduction of matrix damage. This is beneficial for thick-ply laminates, because the delamination area is significantly reduced, leading to a significant increase in residual strength. For the other ply thicknesses, the change in matrix damage does not affect the residual strength or cause a decline due to more significant resulting delamination caused by the suppression of matrix cracking.

The second approach to adapt the matrix's failure behaviour was to design the composite's layup so that undesired failure modes, namely delaminations, become energetically unfavourable. The investigated helicoidal thin-ply layups demonstrated this behaviour. The results show that thin-ply helicoidal layups effectively prevent delamination and only subcritical helicoidal shaped matrix cracking occurs before fibre failure. Consequently, LVI only causes helicoidal, subcritical matrix damage, which results in an outstanding residual compressive strength that significantly exceeds that of 45°-QI laminates. Additionally, the damage does not reduce the compressive stiffness of the specimen. Under tensile loading of unnotched specimens, helicoidal laminates exhibit early matrix crack damage initiation and, due to the limited portion of plies oriented in the loading direction, a low tensile strength. However, notched specimens' layer structure shows almost no notch sensitivity because subcritical matrix damage relieves stress concentrations. As a result, the specimens achieve a similar strength to 45°-QI specimens, despite a significant lower amount of fibres oriented in load direction.

The different approaches to adapt the matrix's behaviour consitute a beneficial effect on the damage tolerance of CFRPs. However, it is also evident that a conflict of objectives concerning the matrix damage properties for undamaged laminates, laminates with stress concentrations under tensile load and the residual strength after impact exists. Consequently, there is no generally applicable way to increase the performance for all load cases with the matrix damage's adaption. The layup design and matrix modification that leads to the most beneficial matrix damage occurrence must be chosen according to the predominant, da-

mage tolerance determining load case. In this case, the presented approaches can significantly increase the damage tolerance. Also, combinations of the proposed methods promise a significant increase in CFRP structures' damage resistance and should be investigated in the future.

The second focus investigated, is the influence of temperature on the damage tolerance of high-performance composites. The significant temperature dependency of the matrix properties leads to high-temperature sensitivity of the damage resulting from the CFRP specimens' impaction. Impacts at elevated temperatures lead to fibre breakage on the specimen's impacted side and a reduced delamination area. The reduced delamination area positively influences the residual compressive strength at room temperature but decreases tensile strength considerably. Impacts at low temperatures lead to an increase in the delamination area and reduces the residual compressive strength. Residual compressive strength tests at elevated temperature reveal that the ambient temperature has a more decisive influence than the impaction energy and temperature during impact. A CDM for FEM simulations is proposed, which includes the temperature dependence of the matrix dominated properties to understand the influence of temperature on the composite's failure behaviour in more detail. The results of the LVI simulation are in good agreement with the experimental results. The simulation can predict the resulting failure modes from LVI and their change due to temperature influence. The subsequent CAI simulation covers the dominant influence of temperature on the residual strength. The results prove that the modified CDM is suitable to investigate the temperature behaviour of CFRP structures.

The outcomings of this thesis highlight that further investigation of the influence of the matrix behaviour on the damage tolerance can identify critical influencing factors on the damage tolerance. These influencing factors need to be included in damage tolerance considerations to design safe and lightweight, high-performance composite structures. The proposed FE model has shown that it could assist in optimising the damage tolerance of composite structures.

However, the results underline that adaptation and knowledge of matrix failure behaviour need to be addressed mutually to further increase the damage tolerance of composite structures. The more knowledge is available about the influencing factors, the better the materials and the laminate design can be

adapted to the environmental conditions and the load cases, thus enabling an optimised design of high-performance composite structures.

Bibliography

[1] EASA. *General Acceptable Means of Compliance for Airworthiness of Products, Parts and Appliances (AMC-20), AMC 20-29: Annex II - AMC 20-29 to ED Decision 2010/003/R*. 2010.

[2] Y. Aoki, H. I. Suemasu, and T. Ishikawa. "Damage propagation in CFRP laminates subjected to low velocity impact and static indentation". In: *Advanced Composite Materials* 16.1 (2007), pp. 45–61. DOI: 10.1163/156855107779755318.

[3] J. Chang, V. Goyal, and J. Klug. *Composite structures damage tolerance analysis methodologies. Tech. Rep. NASA/CR-2012-217347*. NASA Langley Research Center, 2012.

[4] H. Reddick and K. Harold. *Safe-life and damage-tolerant design approaches for helicopter structures*. 1983. URL: https://ntrs.nasa.gov/citations/19830025690.

[5] J. Krautkrämer and H. Krautkrämer. *Ultrasonic Testing of Materials*. 4th Fully Revised Edition. Berlin and Heidelberg: Springer, 1990. ISBN: 9783662106822. DOI: 10.1007/978-3-662-10680-8.

[6] S. Z. H. Shah, S. Karuppanan, P. S. M. Megat-Yusoff, and Z. Sajid. "Impact resistance and damage tolerance of fiber reinforced composites: A review". In: *Composite Structures* 217 (2019), pp. 100–121. ISSN: 02638223. DOI: 10.1016/j.compstruct.2019.03.021.

[7] B. G. Green, M. R. Wisnom, and S. R. Hallett. "An experimental investigation into the tensile strength scaling of notched composites". In: *Composites Part A: Applied Science and Manufacturing* 38.3 (2007), pp. 867–878. DOI: 10.1016/j.compositesa.2006.07.008.

[8] M. R. Wisnom, B. Khan, and S. R. Hallett. "Size effects in unnotched tensile strength of unidirectional and quasi-isotropic carbon/epoxy composites". In: *Composite Structures* 84.1 (2008), pp. 21–28. DOI: 10.1016/j.compstruct.2007.06.002.

[9] B. Y. Chen, T. E. Tay, P. M. Baiz, and S. T. Pinho. "Numerical analysis of size effects on open-hole tensile composite laminates". In: *Composites Part A: Applied Science and Manufacturing* 47 (2013), pp. 52–62. ISSN: 1359835X. DOI: 10.1016/j.compositesa.2012.12.001.

[10] M. McElroy, W. Jackson, R. Olsson, P. Hellström, S. Tsampas, and M. Pankow. "Interaction of delaminations and matrix cracks in a CFRP plate, Part I: A test method for model validation". In: *Composites Part A: Applied Science and Manufacturing* 103 (2017), pp. 314–326. ISSN: 1359835X. DOI: 10.1016/j.compositesa.2017.09.011.

[11] S. R. Hallett, W. Jiang, B. Khan, and M. R. Wisnom. "Modelling the interaction between matrix cracks and delamination damage in scaled quasi-isotropic specimens". In: *Composites Science and Technology* 68.1 (2008), pp. 80–89. ISSN: 0266-3538. DOI: https://doi.org/10.1016/j.compscitech.2007.05.038.

[12] M. R. Wisnom. "Size effects in the testing of fibre-composite materials". In: *Composites Science and Technology* 59.13 (1999), pp. 1937–1957. DOI: 10.1016/S0266-3538(99)00053-6.

[13] S. Sihn, R. Kim, K. Kawabe, and S. Tsai. "Experimental studies of thin-ply laminated composites". In: *Composites Science and Technology* 67.6 (2007), pp. 996–1008. DOI: 10.1016/j.compscitech.2006.06.008.

[14] M. R. Wisnom and S. R. Hallett. "The role of delamination in strength, failure mechanism and hole size effect in open hole tensile tests on quasi-isotropic laminates". In: *Composites Part A: Applied Science and Manufacturing* 40.4 (2009), pp. 335–342. DOI: 10.1016/j.compositesa.2008.12.013.

[15] S. R. Hallett, B. G. Green, W. G. Jiang, and M. R. Wisnom. "An experimental and numerical investigation into the damage mechanisms in notched composites". In: *Composites Part A: Applied Science and Manufacturing* 40.5 (2009), pp. 613–624. DOI: 10.1016/j.compositesa.2009.02.021.

[16] K. Croft, L. Lessard, D. Pasini, M. Hojjati, J. Chen, and A. Yousefpour. "Experimental study of the effect of automated fiber placement induced defects on performance of composite laminates". In: *Composites Part A: Applied Science and Manufacturing* 42.5 (2011), pp. 484–491. ISSN: 1359-835X. DOI: https://doi.org/10.1016/j.compositesa.2011.01.007.

[17] US Department of Defence. *Composite Materials Handbook-MIL 17, Volume III: Guidelines for Characterization of Structural Materials*. SAE International, 2012. ISBN: 9781566768269.

[18] R. Amacher, J. Cugnoni, J. Botsis, L. Sorensen, W. Smith, and C. Dransfeld. "Thin ply composites: Experimental characterization and modeling of size-effects". In: *Composites Science and Technology* 101 (2014), pp. 121–132. DOI: 10.1016/j.compscitech.2014.06.027.

[19] H. Saito, M. Morita, K. Kawabe, M. Kanesaki, H. Takeuchi, M. Tanaka, and I. Kimpara. "Effect of ply-thickness on impact damage morphology in CFRP laminates". In: *Journal of Reinforced Plastics and Composites* 30.13 (2011), pp. 1097–1106. DOI: 10.1177/0731684411416532.

[20] S. Chandrasekaran, N. Sato, F. Tölle, R. Mülhaupt, B. Fiedler, and K. Schulte. "Fracture toughness and failure mechanism of graphene based epoxy composites". In: *Composites Science and Technology* 97 (2014), pp. 90–99. DOI: 10.1016/j.compscitech.2014.03.014.

[21] I. Greenfeld and H. D. Wagner. "Nanocomposite toughness, strength and stiffness: role of filler geometry". In: *Nanocomposites* 1.1 (2015), pp. 3–17. DOI: 10.1179/2055033214Y.0000000002.

[22] Y. Bouligand. "Twisted fibrous arrangements in biological materials and cholesteric mesophases". In: *Tissue and Cell* 4.2 (1972), pp. 189–217. DOI: 10.1016/S0040-8166(72)80042-9.

[23] J. C. Weaver, G. W. Milliron, Al. Miserez, K. Evans-Lutterodt, S. Herrera, I. Gallana, W. J. Mershon, B. Swanson, P. Zavattieri, E. DiMasi, and D. Kisailus. "The stomatopod dactyl club: a formidable damage-tolerant biological hammer". In: *Science (New York, N.Y.)* 336.6086 (2012), pp. 1275–1280. DOI: 10.1126/science.1218764.

[24] M.O.W. Richardson and M. J. Wisheart. "Review of low-velocity impact properties of composite materials". In: *Composites Part A: Applied Science and Manufacturing* 27.12 (1996), pp. 1123–1131. DOI: 10.1016/1359-835X(96)00074-7.

[25] S. Abrate. "Impact on Laminated Composite Materials". In: *Applied Mechanics Reviews* 44.4 (1991), pp. 155–190. DOI: 10.1115/1.3119500.

[26] B. Fiedler, T. Hobbiebrunken, M. Hojo, and K. Schulte. “Influence of stress state and temperature on the strength of epoxy resins”. In: *11th International Conference on Fracture 2005, ICF11* Vol 3 (2005), pp. 2271–2275.

[27] O. Allix. “Modelling and identification of temperature-dependent mechanical behaviour of the elementary ply in carbon/epoxy laminates”. In: *Composites Science and Technology* 56.7 (1996), pp. 883–888. DOI: 10.1016/0266-3538(96)00036-X.

[28] K. D. Cowley and P. W. R. Beaumont. “The interlaminar and intralaminar fracture toughness of carbon-fibre/polymer composites: The effect of temperature”. In: *Composites Science and Technology* 57.11 (1997), pp. 1433–1444. DOI: 10.1016/S0266-3538(97)00047-X.

[29] H. S. Kim, W. X. Wang, and Y. Takao. “Effects of Temperature and Stacking Sequence on the Mode I Interlaminar Fracture Behavior of Composite Laminates”. In: *Key Engineering Materials* 183-187 (2000), pp. 815–820. DOI: 10.4028/www.scientific.net/KEM.183-187.815.

[30] C. Soutis and D. Turkmen. “Moisture and Temperature Effects of the Compressive Failure of CFRP Unidirectional Laminates”. In: *Journal of Composite Materials* 31 (1997). DOI: 10.1177/002199839703100805.

[31] A. Nettles. *Hot/Wet Open Hole Compression Strength of Carbon/Epoxy Laminates for Launch Vehicle Applications: NASA/TM—2009–215900*. NASA Marshall Space Flight Center, 2009.

[32] F. A. Leone, A. C. Bergan, and C. G Dávila. *CompDam - Deformation Gradient Decomposition (DGD), v2.5.0*. 2019.

[33] H. Meeuw, J. Körbelin, D. von Bernstorff, T. Augustin, W. V. Liebig, and B. Fiedler. “Smart dispersion: Validation of OCT and impedance spectroscopy as solutions for in-situ dispersion analysis of CNP/EP - composites”. In: *Materialia* (2018). DOI: 10.1016/j.mtla.2018.06.002.

[34] DIN EN 2564:2019-08. *Bestimmung der Faser-, Harz- und Porenanteile*. 2019. DOI: 10.31030/3064174.

[35] ASTM D4065- 20. *Standard Practice for Plastics: Dynamic Mechanical Properties: Determination and Report of Procedures*. ASTM, 2020. DOI: 10.1520/D4065-20.

[36] ASTM D7028 - 07. *Standard Test Method for Glass Transition Temperature (DMA Tg) of Polymer Matrix Composites by Dynamic Mechanical Analysis (DMA)*. ASTM, 2015. DOI: 10.1520/D7028-07R15.

[37] ASTM D5045-14. *Test Methods for Plane-Strain Fracture Toughness and Strain Energy Release Rate of Plastic Materials*. ASTM, 2014. DOI: 10.1520/D5045-14.

[38] T. Fett. "Stress intensity factors for edge crack subjected to mixed mode four-point bending". In: *Theoretical and Applied Fracture Mechanics* 15.1 (1991), pp. 99–104. DOI: 10.1016/0167-8442(91)90008-8.

[39] ASTM D3039 / D3039M-17. *Test Method for Tensile Properties of Polymer Matrix Composite Materials*. ASTM, 2017. DOI: 10.1520/D3039_D3039M-14.

[40] ASTM D3518 / D3518M-18. *Test Method for In-Plane Shear Response of Polymer Matrix Composite Materials by Tensile Test of a 45 Laminate*. ASTM, 2018. DOI: 10.1520/D3518_D3518M-18.

[41] ASTM D5766 / D5766M-11. *Standard Test Method for Open-Hole Tensile Strength of Polymer Matrix Composite Laminates*. ASTM, 2018. DOI: 10.1520/D5766_D5766M-11.

[42] ASTM D6641 / D6641M-16e1. *Test Method for Compressive Properties of Polymer Matrix Composite Materials Using a Combined Loading Compression (CLC) Test Fixture*. ASTM, 2016. DOI: 10.1520/D6641_D6641M-16E01.

[43] ASTM D7136 / D7136M-20. *Test Method for Measuring the Damage Resistance of a Fiber-Reinforced Polymer Matrix Composite to a Drop-Weight Impact Event*. ASTM, 2013. DOI: 10.1520/D7136_D7136M-15.

[44] ASTM D7137 / D7137M-17. *Standard Test Method for Compressive Residual Strength Properties of Damaged Polymer Matrix Composite Plates*. ASTM, 2017. DOI: 10.1520/D7137_D7137M-17.

[45] ASTM D5528-13. *Standard Test Method for Mode I Interlaminar Fracture Toughness of Unidirectional Fiber- Reinforced Polymer Matrix Composites*. ASTM, 2013. DOI: 10.1520/D5528-13.

[46] ASTM D7905 / D7905M-19e1. *Test Method for Determination of the Mode II Interlaminar Fracture Toughness of Unidirectional Fiber-Reinforced Polymer Matrix Composites*. ASTM. DOI: 10.1520/D7905_D7905M-19E01.

[47] DIN EN ISO 178:2019-08. *Kunststoffe - Bestimmung der Biegeeigenschaften*. 2019. DOI: 10.31030/3030985.

[48] L. Lagunegrand, T. Lorriot, R. Harry, H. Wargnier, and J. M. Quenisset. "Initiation of free-edge delamination in composite laminates". In: *Composites Science and Technology* 66.10 (2006), pp. 1315–1327. DOI: 10.1016/j.compscitech.2005.10.010.

[49] A. Parvizi. "Constrained cracking in glass fibre reinforced epoxy cross-ply laminates". In: *Composites* 9.4 (1978), p. 286. DOI: 10.1016/0010-4361(78)90215-X.

[50] D. L. Flaggs and M. H. Kural. "Experimental Determination of the In Situ Transverse Lamina Strength in Graphite/Epoxy Laminates". In: *Journal of Composite Materials* 16.2 (1982), pp. 103–116. DOI: 10.1177/002199838201600203.

[51] G. J. Dvorak and N. Laws. "Analysis of Progressive Matrix Cracking In Composite Laminates II. First Ply Failure". In: *Journal of Composite Materials* 21.4 (1987), pp. 309–329. DOI: 10.1177/002199838702100402.

[52] P. P. Camanho, M. A. Bessa, G. Catalanotti, M. Vogler, and R. Rolfes. "Modeling the inelastic deformation and fracture of polymer composites – Part II: Smeared crack model". In: *Mechanics of Materials* 59 (2013), pp. 36–49. DOI: 10.1016/j.mechmat.2012.12.001.

[53] T. A. Sebaey, J. Costa, P. Maimí, Y. Batista, N. Blanco, and J. A. Mayugo. "Measurement of the in situ transverse tensile strength of composite plies by means of the real time monitoring of microcracking". In: *Composites Part B: Engineering* 65 (2014), pp. 40–46. DOI: 10.1016/j.compositesb.2014.02.001.

[54] E. Adolfsson and P. Gudmundson. "Matrix crack initiation and progression in compositelaminatessubjected to bending and extension". In: *International Journal of Solids and Structures* 36.21 (1999), pp. 3131–3169. DOI: 10.1016/S0020-7683(98)00142-5.

[55] A. Arteiro, G. Catalanotti, A. R. Melro, P. Linde, and P. P. Camanho. "Micro-mechanical analysis of the in situ effect in polymer composite laminates". In: *Composite Structures* 116 (2014), pp. 827–840. DOI: 10.1016/j.compstruct.2014.06.014.

[56] K. Kawabe, T. Matszo, and Z. Maekawa. "New Technology for Opening Various Reinforcing Fiber Tows". In: *Journal of the Society of Materials Science, Japan* 47.7 (1998), pp. 727–734. DOI: 10.2472/jsms.47.727.

[57] A. Arteiro, G. Catalanotti, J. Xavier, P. Linde, and P. P. Camanho. "Effect of tow thickness on the structural response of aerospace-grade spread-tow fabrics". In: *Composite Structures* 179 (2017), pp. 208–223. DOI: 10.1016/j.compstruct.2017.06.047.

[58] G. Guillamet, A. Turon, J. Costa, J. Renart, P. Linde, and J. A. Mayugo. "Damage occurrence at edges of non-crimp-fabric thin-ply laminates under off-axis uniaxial loading". In: *Composites Science and Technology* 98 (2014), pp. 44–50. DOI: 10.1016/j.compscitech.2014.04.014.

[59] M. Hajikazemi and W. van Paepegem. "Variational analysis of free-edge stress and displacement fields in general un-symmetric and thin-ply laminates under in-plane, bending and thermal loading". In: *Composites Part A: Applied Science and Manufacturing* 113 (2018), pp. 220–232. DOI: 10.1016/j.compositesa.2018.07.030.

[60] J. Cugnoni, R. Amacher, S. Kohler, J. Brunner, E. Kramer, C. Dransfeld, W. Smith, K. Scobbie, L. Sorensen, and J. Botsis. "Towards aerospace grade thin-ply composites: Effect of ply thickness, fibre, matrix and interlayer toughening on strength and damage tolerance". In: *Composites Science and Technology* 168 (2018), pp. 467–477. DOI: 10.1016/j.compscitech.2018.08.037.

[61] E. V. González, P. Maimí, P. P. Camanho, C. S. Lopes, and N. Blanco. "Effects of ply clustering in laminated composite plates under low-velocity impact loading". In: *Composites Science and Technology* 71.6 (2011), pp. 805–817. DOI: 10.1016/j.compscitech.2010.12.018.

[62] T. A. Sebaey, E. V. González, C. S. Lopes, N. Blanco, and J. Costa. "Damage resistance and damage tolerance of dispersed CFRP laminates: Effect of ply clustering". In: *Composite Structures* 106 (2013), pp. 96–103. DOI: 10.1016/j.compstruct.2013.05.052.

[63] Aldobenedetto Zotti, Simona Zuppolini, Mauro Zarrelli, and Anna Borriello. "Fracture Toughening Mechanisms in Epoxy Adhesives". In: *Adhesives*. Ed. by Anna Rudawska. Rijeka: IntechOpen, 2016. Chap. 10. DOI: 10.5772/65250.

[64] Y. Nakamura, M. Yamaguchi, M. Okubo, and T. Matsumoto. “Effect of particle size on mechanical properties of epoxy resin filled with angular-shaped silica”. In: *Journal of Applied Polymer Science* 44.1 (1992), pp. 151–158. DOI: 10.1002/app.1992.070440116.

[65] J. Lee and A.F. Yee. “Fracture of glass bead/epoxy composites: on micro-mechanical deformations”. English. In: *Polymer* 41.23 (2000), pp. 8363–8373.

[66] A. J. Kinloch and A. C. Taylor. In: *Journal of Materials Science* 37.3 (2002), pp. 433–460. ISSN: 0022-2461. DOI: 10.1023/A:1013735103120.

[67] R. A. Pearson and A. F. Yee. “Toughening mechanisms in elastomer-modified epoxies”. In: *Journal of Materials Science* 24.7 (1989), pp. 2571–2580. DOI: 10.1007/BF01174528.

[68] Liu H.-Y., Wang G.-T., Mai Y.-W., and Zeng Y. “On fracture toughness of nano-particle modified epoxy”. In: *Composites Part B: Engineering* 42.8 (2011). Special Issue on Preparation, Properties and Applications of Nanocomposites, pp. 2170–2175. DOI: https://doi.org/10.1016/j.compositesb.2011.05.014.

[69] T.H. Hsieh, A.J. Kinloch, K. Masania, A.C. Taylor, and S. Sprenger. “The mechanisms and mechanics of the toughening of epoxy polymers modified with silica nanoparticles”. In: *Polymer* 51.26 (2010), pp. 6284–6294. DOI: https://doi.org/10.1016/j.polymer.2010.10.048.

[70] R. P. Singh, M. Zhang, and D. Chan. “Toughening of a brittle thermosetting polymer: Effects of reinforcement particle size and volume fraction”. In: *Journal of Materials Science* 37.4 (2002), pp. 781–788. DOI: 10.1023/A:1013844015493.

[71] T. Liu, W. C. Tjiu, Y. Tong, C. He, S. S. Goh, and T.-S. Chung. “Morphology and fracture behavior of intercalated epoxy/clay nanocomposites”. In: *Journal of Applied Polymer Science* 94.3 (2004), pp. 1236–1244. DOI: https://doi.org/10.1002/app.21033.

[72] M. Zappalorto, M. Salviato, and M. Quaresimin. “Mixed mode (I+II) fracture toughness of polymer nanoclay nanocomposites”. In: *Engineering Fracture Mechanics* 111 (2013), pp. 50–64. ISSN: 0013-7944. DOI: https://doi.org/10.1016/j.engfracmech.2013.09.006.

[73] H. Meeuw, V. K. Wisniewski, U. Köpke, A. S. Nia, A. R. Vázquez, M. R. Lohe, X. Feng, and B. Fiedler. "In-line monitoring of carbon nanoparticle epoxy dispersion processes". In: *Production Engineering* 51.4 (2019), p. 585. DOI: 10.1007/s11740-019-00884-5.

[74] M. Quaresimin, K. Schulte, M. Zappalorto, and S. Chandrasekaran. "Toughening mechanisms in polymer nanocomposites: From experiments to modelling". In: *Composites Science and Technology* 123 (2016), pp. 187–204. DOI: 10.1016/j.compscitech.2015.11.027.

[75] A. K. Geim and K. S. Novoselov. "The rise of graphene". In: *Nature Materials* 6.3 (2007), pp. 183–191. DOI: 10.1038/nmat1849.

[76] K. S. Novoselov, A. K. Geim, S. V. Morozov, D. Jiang, Y. Zhang, S. V. Dubonos, I. V. Grigorieva, and A. A. Firsov. "Electric Field Effect in Atomically Thin Carbon Films". In: *Science* 306.5696 (2004), pp. 666–669. DOI: 10.1126/science.1102896.

[77] H. Meeuw, J. Körbelin, V. K. Wisniewski, A.S. Nia, A. R. Vázquez, M. R. Lohe, X. Feng, and B. Fiedler. "Carbon Nanoparticles' Impact on Processability and Physical Properties of Epoxy Resins-A Comprehensive Study Covering Rheological, Electrical, Thermo-Mechanical, and Fracture Properties (Mode I and II)". In: *Polymers* 11.2 (2019). DOI: 10.3390/polym11020231.

[78] N. Lachman and H. D. Wagner. "Correlation between interfacial molecular structure and mechanics in CNT/epoxy nano-composites". In: *Composites Part A: Applied Science and Manufacturing* 41.9 (2010). Special Issue on 10th Deformation and Fracture of Composites Conference: Interfacial interactions in composites and other applications, pp. 1093–1098. DOI: 0.1016/j.compositesa.2009.08.023.

[79] M. Shtein, R. Nadiv, N. Lachman, H. D. Wagner, and O. Regev. "Fracture behavior of nanotube-polymer composites: Insights on surface roughness and failure mechanism". In: *Composites Science and Technology* 87 (2013), pp. 157–163. DOI: https://doi.org/10.1016/j.compscitech.2013.07.016.

[80] S. Chandrasekaran, C. Seidel, and K. Schulte. "Preparation and characterization of graphite nano-platelet (GNP)/epoxy nano-composite: Mechanical, electrical and thermal properties". In: *European Polymer Jour-*

nal 49.12 (2013), pp. 3878–3888. DOI: 10.1016/j.eurpolymj.2013.10.008.

[81] F. H. Gojny, M. H. G. Wichmann, U. Köpke, B. Fiedler, and K. Schulte. "Carbon nanotube-reinforced epoxy-composites: enhanced stiffness and fracture toughness at low nanotube content". In: *Composites Science and Technology* 64.15 (2004), pp. 2363–2371. DOI: 10.1016/j.compscitech.2004.04.002.

[82] F. F. Lange. "The interaction of a crack front with a second-phase dispersion". In: *Philosophical Magazine* 22.179 (1970), pp. 0983–0992. DOI: 10.1080/14786437008221068.

[83] K. Wang, L. Chen, J. Wu, M. L. Toh, C. He, and A. F. Yee. "Epoxy Nanocomposites with Highly Exfoliated Clay: Mechanical Properties and Fracture Mechanisms". In: *Macromolecules* 38.3 (2005), pp. 788–800. DOI: 10.1021/ma048465n.

[84] B. T. Marouf, Y. Mai, R. Bagheri, and R. A. Pearson. "Toughening of Epoxy Nanocomposites: Nano and Hybrid Effects". In: *Polymer Reviews* 56.1 (2016), pp. 70–112. DOI: 10.1080/15583724.2015.1086368.

[85] C. Kostagiannakopoulou, T. H. Loutas, G. Sotiriadis, A. Markou, and V. Kostopoulos. "On the interlaminar fracture toughness of carbon fiber composites enhanced with graphene nano-species". In: *Composites Science and Technology* 118 (2015), pp. 217–225. DOI: 10.1016/j.compscitech.2015.08.017.

[86] H. Ning, J. Li, N. Hu, C. Yan, Y. Liu, L. Wu, F. Liu, and J. Zhang. "Interlaminar mechanical properties of carbon fiber reinforced plastic laminates modified with graphene oxide interleaf". In: *Carbon* 91 (2015), pp. 224–233. DOI: 10.1016/j.carbon.2015.04.054.

[87] B. Ahmadi-Moghadam and F. Taheri. "Fracture and toughening mechanisms of GNP-based nanocomposites in modes I and II fracture". In: *Engineering Fracture Mechanics* 131 (2014), pp. 329–339. DOI: 10.1016/j.engfracmech.2014.08.008.

[88] L. Liu, L. Li, Y. Gao, L. Tang, and Z. Zhang. "Single carbon fiber fracture embedded in an epoxy matrix modified by nanoparticles". In: *Composites Science and Technology* 77 (2013), pp. 101–109. DOI: 10.1016/j.compscitech.2012.12.015.

[89] J. Zhang, S. Deng, Y. Wang, L. Ye, L. Zhou, and Z. Zhang. "Effect of nanoparticles on interfacial properties of carbon fibre–epoxy composites". In: *Composites Part A: Applied Science and Manufacturing* 55 (2013), pp. 35–44. DOI: 10.1016/j.compositesa.2013.08.005.

[90] Y. Tian, H. Zhang, and Z. Zhang. "Influence of nanoparticles on the interfacial properties of fiber-reinforced-epoxy composites". In: *Composites Part A: Applied Science and Manufacturing* 98 (2017), pp. 1–8. DOI: 10.1016/j.compositesa.2017.03.007.

[91] J. B. Knoll, B. T. Riecken, N. Kosmann, S. Chandrasekaran, K. Schulte, and B. Fiedler. "The effect of carbon nanoparticles on the fatigue performance of carbon fibre reinforced epoxy". In: *Composites Part A: Applied Science and Manufacturing* 67 (2014), pp. 233–240. DOI: 10.1016/j.compositesa.2014.08.022.

[92] C. Leopold, G. Just, I. Koch, A. Schetle, J. B. Kosmann, M. Gude, and B. Fiedler. "Damage mechanisms of tailored few-layer graphene modified CFRP cross-ply laminates". In: *Composites Part A: Applied Science and Manufacturing* 117 (2019), pp. 332–344. DOI: 10.1016/j.compositesa.2018.12.005.

[93] V. Kostopoulos, A. Baltopoulos, P. Karapappas, A. Vavouliotis, and A. Paipetis. "Impact and after-impact properties of carbon fibre reinforced composites enhanced with multi-wall carbon nanotubes". In: *Composites Science and Technology* 70.4 (2010), pp. 553–563. DOI: 10.1016/j.compscitech.2009.11.023.

[94] E. Mannov, H. Schmutzler, S. Chandrasekaran, C. Viets, S. Buschhorn, F. Tölle, R. Mülhaupt, and K. Schulte. "Improvement of compressive strength after impact in fibre reinforced polymer composites by matrix modification with thermally reduced graphene oxide". In: *Composites Science and Technology* 87 (2013), pp. 36–41. DOI: 10.1016/j.compscitech.2013.07.019.

[95] J. Moon, M. Kim, C. Kim, and S. Bhowmik. "Improvement of tensile properties of CFRP composites under LEO space environment by applying MWNTs and thin-ply". In: *Composites Part A: Applied Science and Manufacturing* 42.6 (2011), pp. 694–701. DOI: 10.1016/j.compositesa.2011.02.011.

[96] Avanzare. *avan2: Technical Datasheet*. 2017.

[97] Global Graphene Group. *N002-PDE: Technical Datasheet*. 2018.

[98] Global Graphene Group. *N002-PDR: Technical Datasheet*. 2018.

[99] Global Graphene Group. *N006-P: Technical Datasheet*. 2018.

[100] OCSiAl. *TUBALL 75: Technical Datasheet*. 2018.

[101] North Thin Ply Technology. *ThinPreg 402 data sheet: Technical datasheet*. 2017.

[102] B. Kötter, J. Karsten, J. Körbelin, and B. Fiedler. "CFRP Thin-Ply Fibre Metal Laminates: Influences of Ply Thickness and Metal Layers on Open Hole Tension and Compression Properties". In: *Materials (Basel, Switzerland)* 13.4 (2020). DOI: 10.3390/ma13040910.

[103] P. O. Sjoblom, J. T. Hartness, and T. M. Cordel. "On Low-Velocity Impact Testing of Composite Materials". In: *Journal of Composite Materials* 22.1 (1988). DOI: 10.1177/002199838802200103.

[104] H. Meeuw, C. Viets, W. V. Liebig, K. Schulte, and B. Fiedler. "Morphological influence of carbon nanofillers on the piezoresistive response of carbon nanoparticle/epoxy composites under mechanical load". In: *European Polymer Journal* 85 (2016), pp. 198–210. DOI: 10.1016/j.eurpolymj.2016.10.027.

[105] Y. Tang, L. Ye, Z. Zhang, and K. Friedrich. "Interlaminar fracture toughness and CAI strength of fibre-reinforced composites with nanoparticles – A review". In: *Composites Science and Technology* 86 (2013), pp. 26–37. DOI: 10.1016/j.compscitech.2013.06.021.

[106] T. H. Hsieh, A. J. Kinloch, A. C. Taylor, and I. A. Kinloch. "The effect of carbon nanotubes on the fracture toughness and fatigue performance of a thermosetting epoxy polymer". In: *Journal of Materials Science* 46.23 (2011), pp. 7525–7535. DOI: 10.1007/s10853-011-5724-0.

[107] C. Leopold, T. Augustin, T. Schwebler, J. Lehmann, W. V. Liebig, and B. Fiedler. "Influence of carbon nanoparticle modification on the mechanical and electrical properties of epoxy in small volumes". In: *Journal of colloid and interface science* 506 (2017), pp. 620–632. DOI: 10.1016/j.jcis.2017.07.085.

[108] C. Leopold, W. V. Liebig, H. Wittich, and B. Fiedler. "Size effect of graphene nanoparticle modified epoxy matrix". In: *Composites Science and Technology* 134 (2016), pp. 217–225. DOI: 10.1016/j.compscitech.2016.08.022.

[109] C. Monteserín, M. Blanco, E. Aranzabe, A. Aranzabe, J. M. Laza, A. Larrañaga-Varga, and J. L. Vilas. "Effects of Graphene Oxide and Chemically-Reduced Graphene Oxide on the Dynamic Mechanical Properties of Epoxy Amine Composites". In: *Polymers* 9.9 (2017). DOI: 10.3390/polym9090449.

[110] A. Carpinteri, S. Valente, G. Ferrara, and G. Melchiorrl. "Is mode II fracture energy a real material property?" In: *Computers & Structures* 48.3 (1993), pp. 397–413. DOI: 10.1016/0045-7949(93)90316-6.

[111] F. Ramsteiner. "An approach towards understanding model II failure of poly(methyl methacrylate)". In: *Polymer* 34.2 (1993), pp. 312–317. DOI: 10.1016/0032-3861(93)90082-L.

[112] S. M. Lee. "Mode II Interlaminar Crack Growth Process in Polymer Matrix Composites". In: *Journal of Reinforced Plastics and Composites* 18.13 (1999), pp. 1254–1266. DOI: 10.1177/073168449901801308.

[113] M. E. J. Dekkers and D. Heikens. "Crazing and shear deformation in glass bead-filled glassy polymers". In: *Journal of Materials Science* 20.11 (1985), pp. 3873–3880. DOI: 10.1007/BF00552375.

[114] A. J. Kinloch and R. J. Young. *Fracture Behaviour of Polymers*. Dordrecht: Springer Netherlands, 2013. ISBN: 978-94-017-1596-6.

[115] J. Chu, R. J. Young, T J.A. Slater, T L. Burnett, B Coburn, L Chichignoud, A Vuilleumier, and Z Li. "Realizing the theoretical stiffness of graphene in composites through confinement between carbon fibers". In: *Composites Part A: Applied Science and Manufacturing* 113 (2018), pp. 311–317. DOI: 10.1016/j.compositesa.2018.07.032.

[116] B. Ahmadi-Moghadam and F. Taheri. "Influence of graphene nanoplatelets on modes I, II and III interlaminar fracture toughness of fiber-reinforced polymer composites". In: *Engineering Fracture Mechanics* 143 (2015), pp. 97–107. DOI: 10.1016/j.engfracmech.2015.06.026.

[117] T. O'Brien. "Composite interlaminar shear fracture toughness, GIIC: shear measurement or sheer myth?" In: *ASTM STP 1330* (1998), pp. 3–18.

[118] J. Pascoe, S. Pimenta, and S. T. Pinho. "Interlocking thin-ply reinforcement concept for improved fracture toughness and damage tolerance". In: *Composites Science and Technology* 181 (2019), p. 107681. DOI: 10.1016/j.compscitech.2019.107681.

[119] A. Nettles and L. Scharber. "The Influence of G I and G II on the compression after impact strength of carbon fiber/epoxy laminates". In: *Journal of Composite Materials* 52.8 (2018), pp. 991–1003. DOI: 10.1177/0021998317719567.

[120] Toray Composite Materials. *T700S Datasheet*. 2018.

[121] T. Yokozeki, Y. Aoki, and T. Ogasawara. "Experimental characterization of strength and damage resistance properties of thin-ply carbon fiber/toughened epoxy laminates". In: *Composite Structures* 82.3 (2008), pp. 382–389. DOI: 10.1016/j.compstruct.2007.01.015.

[122] J. Cho, J. Y. Chen, and I. M. Daniel. "Mechanical enhancement of carbon fiber/epoxy composites by graphite nanoplatelet reinforcement". In: *Scripta Materialia* 56.8 (2007), pp. 685–688. DOI: 10.1016/j.scriptamat.2006.12.038.

[123] M. F. Uddin and C. T. Sun. "Strength of unidirectional glass/epoxy composite with silica nanoparticle-enhanced matrix". In: *Composites Science and Technology* 68.7-8 (2008), pp. 1637–1643. DOI: 10.1016/j.compscitech.2008.02.026.

[124] M. Gower, R. Shaw, and G. Sims. *Evaluation of the repeatability under static loading of a compression-after-impact test method proposed for ISO standardisation: DEPC-MN 036*. UK, 2005.

[125] M. J. Pavier and W. T. Chester. "Compression failure of carbon fibre-reinforced coupons containing central delaminations". In: *Composites* 21 (1990), pp. 23–31. DOI: 10.1016/0010-4361(90)90095-E.

[126] S. O. Peck and G. S. Springer. "The Behavior of Delaminations in Composite Plates—Analytical and Experimental Results". In: *Journal of Composite Materials* 25 (1991), pp. 907–929.

[127] Y. M. L. Cahain, J. Noden, and S. R. Hallett. "Effect of insert material on artificial delamination performance in composite laminates". In: *Journal of Composite Materials* 49.21 (2015), pp. 2589–2597. DOI: 10.1177/0021998314550428.

[128] M. Khammassi, R. Wali, A. Al-Mutory, A. Yousaf, S. Sassi, and M. Gharib. "A simplified modal-based method to quantify delamination in carbon fibre-reinforced plastic beam". In: *Nondestructive Testing and Evaluation* 34.3 (2019), pp. 283–298. DOI: 10.1080/10589759.2019.1590828.

[129] G. J. Short, F. J. Guild, and M. J. Pavier. "The effect of delamination geometry on the compressive failure of composite laminates". In: *Composites Science and Technology* 2001.61 (2001), pp. 2075–2086. DOI: 10.1016/S0266-3538(01)00134-8.

[130] R. M. Jones. *Mechanics of composite materials*. 2nd ed. Philadelphia PA: Taylor & Francis, 1999.

[131] J. N. Reddy. *Mechanics of Laminated Composite Plates and Shells Theory and An*. 2nd ed. Boca Raton: Chapman and Hall/CRC, 2004. ISBN: 0849315921.

[132] M. F. Pernice, N. V. de Carvalho, J. G. Ratcliffe, and S. R. Hallett. "Experimental study on delamination migration in composite laminates". In: *Composites Part A: Applied Science and Manufacturing* 73.4 (2015), pp. 20–34. DOI: 10.1016/j.compositesa.2015.02.018.

[133] L. Mencattelli and S. T. Pinho. "Realising bio-inspired impact damage-tolerant thin-ply CFRP Bouligand structures via promoting diffused sub-critical helicoidal damage". In: *Composites Science and Technology* 182 (2019), p. 107684. DOI: 10.1016/j.compscitech.2019.107684.

[134] G. Christian. *Spooky: Smashing Mantis Shrimp / Odontodactylus latirostris*. 2015. URL: https://www.flickr.com/photos/christian_gloor/17210859318/.

[135] S. N. Patek and R. L. Caldwell. "Extreme impact and cavitation forces of a biological hammer: strike forces of the peacock mantis shrimp Odontodactylus scyllarus". In: 208.19 (2005), pp. 3655–3664. DOI: 10.1242/jeb.01831.

[136] G. Milliron. "Lightweight Impact-Resistant Composite Materials: Lessons from Mantis Shrimp". Disseration. Riversite: University of California, 2012. URL: https://escholarship.org/uc/item/5zc2x10s.

[137] L. K. Grunenfelder, N. Suksangpanya, C. Salinas, G. Milliron, N. Yaraghi, S. Herrera, K. Evans-Lutterodt, S. R. Nutt, P. Zavattieri, and D. Kisailus. "Bio-inspired impact-resistant composites". In: *Acta biomaterialia* 10.9 (2014), pp. 3997–4008. DOI: 10.1016/j.actbio.2014.03.022.

[138] H. Jiang, Y. Ren, Z. Liu, S. Zhang, and Z. Lin. "Low-velocity impact resistance behaviors of bio-inspired helicoidal composite laminates with non-linear rotation angle based layups". In: *Composite Structures* 214 (2019), pp. 463–475. DOI: 10.1016/j.compstruct.2019.02.034.

[139] J. L. Liu, H. P. Lee, and V. B. C. Tan. "Failure mechanisms in bioinspired helicoidal laminates". In: *Composites Science and Technology* 157 (2018), pp. 99–106. DOI: 10.1016/j.compscitech.2018.01.033.

[140] F. Pinto, O. Iervolino, G. Scarselli, D. Ginzburg, and M. Meo. "Bioinspired twisted composites based on Bouligand structures". In: *Bioinspiration, Biomimetics, and Bioreplication 2016*. Ed. by Raúl J. Martín-Palma, Akhlesh Lakhtakia, and Mato Knez. SPIE Proceedings. SPIE, 2016, 97970E. DOI: 10.1117/12.2219088.

[141] X. Wu, J. D. Fuller, M. L. Longana, and M. R. Wisnom. "Reduced notch sensitivity in pseudo-ductile CFRP thin ply angle-ply laminates with central 0° plies". In: *Composites Part A: Applied Science and Manufacturing* 111 (2018), pp. 62–72. DOI: 10.1016/j.compositesa.2018.05.011.

[142] T. Apichattrabrut and K. Ravi-Chandar. "Helicoidal Composites". In: *Mechanics of Advanced Materials and Structures* 13.1 (2006), pp. 61–76. DOI: 10.1080/15376490500343808.

[143] L. Cheng, A. Thomas, J. L. Glancey, and A. M. Karlsson. "Mechanical behavior of bio-inspired laminated composites". In: *Composites Part A: Applied Science and Manufacturing* 42.2 (2011), pp. 211–220. DOI: 10.1016/j.compositesa.2010.11.009.

[144] J. Berthelot. "Transverse cracking and delamination in cross-ply glass-fiber and carbon-fiber reinforced plastic laminates: Static and fatigue loading". In: *Applied Mechanics Reviews* 56.1 (2003), pp. 111–147. DOI: 10.1115/1.1519557.

[145] J. Berthe and M. Ragonet. "Passive infrared thermography measurement of transverse cracking evolution in cross-ply laminates". In: *Strain* 54.6 (2018), e12293. DOI: 10.1111/str.12293.

[146] J. D. Fuller and M. R. Wisnom. "Pseudo-ductility and damage suppression in thin ply CFRP angle-ply laminates". In: *Composites Part A: Applied Science and Manufacturing* 69 (2015), pp. 64–71. DOI: 10.1016/j.compositesa.2014.11.004.

[147] AIMS05-01-002. *Carbon Fibre Reinforced Epoxy Prepreg Unidirectional Tape/180C- curing class. Intermediate modulus fibre Structural material.* Airbus Material Specification, 2008.

[148] DIN EN 443:2008. *Feuerwehrhelme für die Brandbekämpfung in Gebäuden und anderen baulichen Anlagen.* 2008. DOI: 10.31030/1381708.

[149] DIN EN 12245. "Ortsbewegliche Gasflaschen – Vollumwickelte Flaschen aus Verbundwerkstoffen; Deutsche und Englische Fassung". In: (2020). DOI: 10.31030/1864915.

[150] D. Petersen, R. Rolfes, and R. Zimmermann. "Thermo-mechanical design aspects for primary composite structures of large transport aircraft". In: *Aerospace Science and Technology* 5.2 (2001), pp. 135–146. DOI: 10.1016/S1270-9638(00)01089-0.

[151] H. A. Nasrallah, E. Nieplova, and E. Ramadan. "Warm season extreme temperature events in Kuwait". In: *Journal of Arid Environments* 56.2 (2004), pp. 357–371. DOI: 10.1016/S0140-1963(03)00007-7.

[152] P. J. Callus. *France-Australia Technical Arrangement TA 1/99 – Work Package 1: Study of the Equivalence of Hot/Dry and Hot/Wet Testing.* Ed. by DSTO Defence Science and Technology Organisation. 2005.

[153] B. Fiedler, A. Gagel, T. Hobbiebrunken, K. Schulte, M. Hojo, and S. Ochiai. "Modelling of the transverse strength of fibre reinforced epoxy composite at low and high temperature". In: *Composite Interfaces* 12.3-4 (2005), pp. 379–394. DOI: 10.1163/1568554053971560.

[154] W. Zhao. "Mode I Delamination Fracture Characterization of Polymeric Composites under Elevated Temperature". Dissertation. Syracuse University, 2011.

[155] A. J. Russell and K. N. Street. "Moisture and Temperature Effects on the Mode I and Mode II Interlaminar Fracture of Graphite/Epoxy Composites". In: *Key Engineering Materials* 37 (1989), pp. 199–208. DOI: 10.4028/www.scientific.net/KEM.37.199.

[156] S. B. Cox, L. Tate, S. E. Danley, J. W. Sampson, B. J. Taylor, J. K. Sutter, and Sandi G. Miller. "Stress Free Temperature Testing and Calculations on Out-of-Autoclave Composites". PhD thesis. NASA Kennedy Space Center, 2013. URL: https://ntrs.nasa.gov/citations/20130011525%202019-04-15T13:08:55%2000:00Z.

[157] J. Berthe, M. Brieu, and E. Deletombe. "Thermo-viscoelastic modelling of organic matrix composite behaviour – Application to T700GC/M21". In: *Mechanics of Materials* 81 (2015), pp. 18–24. DOI: 10.1016/j.mechmat.2014.10.005.

[158] T. Gomez-del Rio, R. Zaera, E. Barbero, and C. Navarro. "Damage in CFRPs due to low velocity impact at low temperature". In: *Composites Part B: Engineering* 36.1 (2005), pp. 41–50. DOI: 10.1016/j.compositesb.2004.04.003.

[159] R. Suvarna, V. Arumugam, D. J. Bull, A. R. Chambers, and C. Santulli. "Effect of temperature on low velocity impact damage and post-impact flexural strength of CFRP assessed using ultrasonic C-scan and micro-focus computed tomography". In: *Composites Part B: Engineering* 66 (2014), pp. 58–64. DOI: 10.1016/j.compositesb.2014.04.028.

[160] K.E. Im, C. Cha, S. Kim, and I. Yang. "Effects of temperature on impact damages in CFRP composite laminates". In: *Composites Part B: Engineering* 32.8 (2001), pp. 669–682. DOI: 10.1016/S1359-8368(01)00046-4.

[161] M. Aktaş, R. Karakuzu, and Y. Arman. "Compression-after impact behavior of laminated composite plates subjected to low velocity impact in high temperatures". In: *Composite Structures* 89.1 (2009), pp. 77–82. DOI: 10.1016/j.compstruct.2008.07.002.

[162] M. Aktaş, R. Karakuzu, and B. Icten. "Impact Behavior of Glass/Epoxy Laminated Composite Plates at High Temperatures". In: *Journal of Composite Materials* 44.19 (2010), pp. 2289–2299. DOI: 10.1177/0021998310369576.

[163] S. Sánchez-Sáez, E. Barbero, and C. Navarro. "Compressive residual strength at low temperatures of composite laminates subjected to low-velocity impacts". In: *Composite Structures* 85.3 (2008), pp. 226–232. DOI: 10.1016/j.compstruct.2007.10.026.

[164] W. J. Cantwell and J. Morton. "Comparison of the low and high velocity impact response of cfrp". In: *Composites* 20.6 (1989), pp. 545–551. DOI: 10.1016/0010-4361(89)90913-0.

[165] J. Zhou, B. Liao, Y. Shi, Y. Zuo, H. Tuo, and L. Jia. "Low-velocity impact behavior and residual tensile strength of CFRP laminates". In: *Composites Part B: Engineering* 161 (2019), pp. 300–313. DOI: 10.1016/j.compositesb.2018.10.090.

[166] Hexcel. *HeyPly M21: Epoxy Matrix (180 °C curing matrix.* Datasheet, 2016.

[167] D. McGowan and D. Ambur. *Compression response of a sandwich fuselage keel panel with and without damage: NASA TM 110302.* 1997.

[168] M. J. Laffan, S. T. Pinho, P. Robinson, L. Iannucci, and A. J. McMillan. "Measurement of the fracture toughness associated with the longitudinal fibre compressive failure mode of laminated composites". In: *Composites Part A: Applied Science and Manufacturing* 43.11 (2012), pp. 1930–1938. DOI: 10.1016/j.compositesa.2012.04.009.

[169] E. Panettieri, D. Fanteria, M. Montemurro, and C. Froustey. "Low-velocity impact tests on carbon/epoxy composite laminates: A benchmark study". In: *Composites Part B: Engineering* 107 (2016), pp. 9–21. DOI: 10.1016/j.compositesb.2016.09.057.

[170] P. Ladaveze and E. Ledantex. "Damage modelling of the elementary ply for laminated composites". In: *Composites Science and Technology* 43.3 (1992), pp. 257–267. DOI: 10.1016/0266-3538(92)90097-M.

[171] S. T. Pinho, R. Darvizeh, P. Robinson, C. Schuecker, and P. P. Camanho. "Material and structural response of polymer-matrix fibre-reinforced composites". In: *Journal of Composite Materials* 46.19-20 (2012), pp. 2313–2341. DOI: 10.1177/0021998312454478.

[172] G. Catalanotti, P. P. Camanho, and A. T. Marques. "Three-dimensional failure criteria for fiber-reinforced laminates". In: *Composite Structures* 95 (2013), pp. 63–79. DOI: 10.1016/j.compstruct.2012.07.016.

[173] C. S. Lopes, S. Sádaba, C. González, J. Llorca, and P. P. Camanho. "Physically-sound simulation of low-velocity impact on fiber reinforced laminates". In: *International Journal of Impact Engineering* 92 (2016), pp. 3–17. DOI: 10.1016/j.ijimpeng.2015.05.014.

[174] S. Rivallant, C. Bouvet, and N. Hongkarnjanakul. “Failure analysis of CFRP laminates subjected to compression after impact: FE simulation using discrete interface elements”. In: *Composites Part A: Applied Science and Manufacturing* 55 (2013), pp. 83–93. DOI: 10.1016/j.compositesa.2013.08.003.

[175] N. Dubary, C. Bouvet, S. Rivallant, and L. Ratsifandrihana. “Damage tolerance of an impacted composite laminate”. In: *Composite Structures* 206 (2018), pp. 261–271. DOI: 10.1016/j.compstruct.2018.08.045.

[176] C. Chen. “Investigation of environmental effects on impact damage tolerance of composite laminates”. PhD thesis. Toulouse: Université Fédérale Toulouse Midi-Pyrénées, 2015.

[177] Z. Liu, Z. Guan, R. Tan, and J. Xu. “Analysis of Open-Hole Compressive CFRP Laminates at Various Temperatures Based on a Multiscale Strategy”. In: *Applied Composite Materials* 26.3 (2019), pp. 923–944. DOI: 10.1007/s10443-019-9759-8.

[178] S. M. Lee. “Fracture of adhesive joints and laminated composites”. In: *Polymer Engineering and Science* 27.1 (1987), pp. 77–81. DOI: 10.1002/pen.760270111.

[179] M. Hojo, S. Matsuda, M. Tanaka, S. Ochiai, and A. Murakami. “Mode I delamination fatigue properties of interlayer-toughened CF/epoxy laminates”. In: *Composites Science and Technology* 66.5 (2006), pp. 665–675. DOI: 10.1016/j.compscitech.2005.07.038.

[180] M. Hojo. “Mode I and II delamination fatigue crack growth behavior of alumina fiber/epoxy laminates in liquid nitrogen”. In: *International Journal of Fatigue* 24.2-4 (2002), pp. 109–118. DOI: 10.1016/S0142-1123(01)00065-2.

[181] S. M. Lee. “Mode II delamination failure mechanisms of polymer matrix composites”. In: *Journal of Materials Science* 32.5 (1997), pp. 1287–1295. DOI: 10.1023/A:1018552506085.

[182] P. F. Giddings, C. R. Bowen, A.I.T. Salo, H. A. Kim, and A. Ive. “Bistable composite laminates: Effects of laminate composition on cured shape and response to thermal load”. In: *Composite Structures* 92.9 (2010), pp. 2220–2225. DOI: 10.1016/j.compstruct.2009.08.043.

[183] F. A. Leone. "Deformation gradient tensor decomposition for representing matrix cracks in fiber-reinforced materials". In: *Composites Part A: Applied Science and Manufacturing* 76 (2015), pp. 334–341. DOI: 10.1016/j.compositesa.2015.06.014.

[184] P. Maimí, P. P. Camanho, J. A. Mayugo, and C. G. Dávila. "A continuum damage model for composite laminates: Part I – Constitutive model". In: *Mechanics of Materials* 39.10 (2007), pp. 897–908. DOI: 10.1016/j.mechmat.2007.03.005.

[185] C. G. Dávila, C. A. Rose, and P. P. Camanho. "A procedure for superposing linear cohesive laws to represent multiple damage mechanisms in the fracture of composites". In: *International Journal of Fracture* 158.2 (2009), pp. 211–223. DOI: 10.1007/s10704-009-9366-z.

[186] F. P. Meer and L. J. Sluys. "A phantom node formulation with mixed mode cohesive law for splitting in laminates". In: *International Journal of Fracture* 158.2 (2009), pp. 107–124. DOI: 10.1007/s10704-009-9344-5.

[187] M. L. Benzeggagh and M. Kenane. "Measurement of mixed-mode delamination fracture toughness of unidirectional glass/epoxy composites with mixed-mode bending apparatus". In: *Composites Science and Technology* 56.4 (1996), pp. 439–449. DOI: 10.1016/0266-3538(96)00005-X.

[188] A. Turon, P. P. Camanho, J. Costa, and J. Renart. "Accurate simulation of delamination growth under mixed-mode loading using cohesive elements: Definition of interlaminar strengths and elastic stiffness". In: *Composite Structures* 92.8 (2010), pp. 1857–1864. DOI: 10.1016/j.compstruct.2010.01.012.

[189] S. T. Pinho, C. G. Dávila, P. Camanho, L. Iannucci, and P. Robinson. *Failure Models and Criteria for FRP Under In-Plane or Three-Dimensional Stress States Including Shear Non-Linearity: NASA/TM-2005-213530*. NASA Langley Research Center, 2005.

[190] W. Ramberg and W. R. Osgood. *Description of stress-strain curves by three parameters*. Vol. 902. Technical note / National Advisory Committee for Aeronautics. Washington D.C.: National Advisory Committee for Aeronautics, 1943.

[191] G. Erçin. "Stress Gradient Effects in Laminated Composites". Dissertation. Portugal: University of Porto, 2013.

A. Appendix to Chapter 3

Table A.1.: Summary of the results of SENB tests from the particle screening

Particle		K_{IC}	K_{IIC}
	wt. %	MPa $\sqrt{m}$	MPa $\sqrt{m}$
Neat	-	0.71 ± 0.02	1.45 ± 0.04
Tuball 75	0.05	0.73 ± 0.02	1.17 ± 0.08
Tuball 75	0.1	0.76 ± 0.03	1.41 ± 0.23
Tuball 90	0.05	0.79 ± 0.03	1.32 ± 0.12
Tuball 90	0.1	0.78 ± 0.04	1.19 ± 0.11
Avan 2	0.05	0.81 ± 0.03	1.39 ± 0.18
Avan 2	0.1	0.72 ± 0.03	1.22 ± 0.12
N002-PDT	0.05	0.77 ± 0.04	1.20 ± 0.06
N002-PDT	0.1	0.81 ± 0.05	1.28 ± 0.15
N002-PDE	0.05	0.77 ± 0.05	1.11 ± 0.10
N002-PDE	0.1	0.82 ± 0.05	1.13 ± 0.05
N006-P	0.05	0.77 ± 0.04	1.21 ± 0.12
N006-P	0.1	0.84 ± 0.01	1.17 ± 0.09

Table A.2.: Summary of the results of the DCB tests

Crack Length [mm]	Neat G_{IC} $[J/m^2]$	Nano G_{IC} $[J/m^2]$
53	111.19 ± 6.70	149.64 ± 14.64
54	122.99 ± 7.05	160.53 ± 16.97
55	134.32 ± 9.77	173.76 ± 17.40
56	150.73 ± 17.54	184.42 ± 14.89
57	164.90 ± 21.51	193.77 ± 17.04
63	217.24 ± 14.27	236.16 ± 15.97
68	234.63 ± 11.67	253.00 ± 17.66
73	243.43 ± 14.33	266.96 ± 24.40
78	251.75 ± 16.40	277.09 ± 28.32

Table A.3.: Summary of the results of the ENF tests

	G_{IIC} $[J/m^2]$
Neat	448.83 ± 30.07
Nano	622.66 ± 46.50

Table A.4.: Summary of the results of the OHT tests

Material		σ_t^{max}	σ_t^{onset}	FVC ϕ	σ_t^{onset}	σ_t^{*max}	σ_{net}^{*max}	k_F
g/m^2	$[MPa]$	$[MPa]$	[%]	$[MPa]$	$[MPa]$	$[MPa]$	$[MPa]$	-
Neat	30	356.92 ± 5.26	391.10 ± 4.92	57.80 ± 0.51	342.66 ± 5.05	375.88 ± 4.73	449.25 ± 5.75	0.40 ± 0.01
Tailored	30	379.02 ± 19.08	412.80 ± 9.67	57.69 ± 0.69	364.63 ± 18.35	397.56 ± 9.31	476.17 ± 10.98	0.42 ± 0.01
Nano	30	391.45 ± 6.13	394.78 ± 3.82	55.04 ± 0.72	385.74 ± 6.13	398.53 ± 3.85	477.11 ± 5.08	0.42 ± 0.00
Neat	60	340.92 ± 13.00	404.22 ± 7.16	58.01 ± 0.07	326.17 ± 12.44	387.14 ± 6.86	462.77 ± 8.14	0.40 ± 0.01
Tailored	60	350.48 ± 16.55	408.54 ± 1.35	57.95 ± 0.21	335.64 ± 15.85	391.66 ± 1.29	468.99 ± 0.55	0.41 ± 0.00
Nano	60	388.30 ± 5.73	400.40 ± 9.19	56.32 ± 0.61	382.64 ± 5.64	394.99 ± 9.07	474.26 ± 10.62	0.41 ± 0.01
Neat	120	299.57 ± 1.93	416.15 ± 13.05	56.06 ± 0.57	296.54 ± 1.91	410.89 ± 12.20	492.86 ± 14.57	0.50 ± 0.01
Tailored	120	330.44 ± 16.74	419.08 ± 7.28	55.96 ± 1.30	327.72 ± 16.61	414.08 ± 7.03	496.50 ± 8.39	0.50 ± 0.01
Nano	120	359.28 ± 7.04	398.89 ± 6.50	54.68 ± 0.26	364.63 ± 7.14	396.50 ± 11.41	473.19 ± 12.45	0.48 ± 0.01
Neat	240	244.76 ± 14.64	427.75 ± 5.87	55.57 ± 0.92	308.99 ± 22.22	427.70 ± 5.87	512.93 ± 7.03	0.58 ± 0.01
Tailored	240	247.03 ± 11.52	440.10 ± 10.79	54.79 ± 0.21	244.47 ± 14.62	46.29 ± 10.94	535.40 ± 13.02	0.61 ± 0.01
Nano	240	295.10 ± 21.22	409.02 ± 8.32	53.01 ± 0.26	250.24 ± 11.67	428.73 ± 8.72	514.69 ± 11.09	0.58 ± 0.01

*normalised to 55.56% FVC UNT strength data to calculate notch sensitivity k_F from Kötter et al. [102]

Table A.5.: Summary of the results of the compression tests

Material		Compressive Strength $\sigma_c^{\max}$	FVC ϕ	Compressive Strength* $\sigma_c^{*\max}$
	g/m^2	$[MPa]$	[%]	$[MPa]$
Neat	30	690.73 ± 22.18	57.81 ± 0.51	663.13 ± 21.29
Nano	30	718.48 ± 32.08	55.04 ± 0.72	724.51 ± 32.35
Neat	60	667.45 ± 24.62	58.01 ± 0.07	638.56 ± 23.55
Nano	60	651.88 ± 15.92	56.32 ± 0.61	642.38 ± 15.69
Neat	120	610.39 ± 15.67	56.07 ± 0.57	604.22 ± 15.51
Nano	120	660.26 ± 19.75	54.68 ± 0.26	670.10 ± 20.04
Neat	240	565.63 ± 12.63	55.57 ± 0.92	564.96 ± 12.61
Nano	240	554.19 ± 18.71	53.01 ± 0.26	580.27 ± 19.59

*normalised to 55.56 % FVC

Table A.6.: Summary of results of the impact and compression after impact tests

Material	g/m^2	CAI Strength σ_c^{max} $[MPa]$	FVC ϕ [%]	CAI Strength* σ_c^{*max} $[MPa]$	Permanent Indentation Depth $[\mu m]$	Permanent Bulge Heigt $[\mu m]$	C-Scan Delamination Area $[mm^2]$	Measured Delamination Area $[mm^2]$
Neat	30	178.80 ± 1.27	57.81 ± 0.51	172.41 ± 1.22	−45.44 ± 14.25	62.27 ± 15.43	5881.35 ± 1415.06	13817
Nano	30	163.72 ± 10.17	55.04 ± 0.72	176.94 ± 10.26	−32.61 ± 5.55	19.59 ± 7.09	5352.04 ± 930.56	8872
Neat	60	169.97 ± 5.59	58.01 ± 0.07	167.64 ± 5.35	−133.60 ± 22.00	116.24 ± 19.88	1950.71 ± 329.72	6908
Nano	60	151.50 ± 8.63	56.32 ± 0.61	159.26 ± 8.50	−70.08 ± 10.92	39.82 ± 6.85	3944.01 ± 1339.30	7017
Neat	120	162.39 ± 5.54	56.07 ± 0.57	168.56 ± 5.48	−142.90 ± 12.23	136.70 ± 9.11	2307.04 ± 916.25	7561
Nano	120	170.73 ± 5.90	54.68 ± 0.26	171.26 ± 5.99	−132.16 ± 9.19	120.44 ± 11.25	1667.67 ± 280.99	5054
Neat	240	144.57 ± 7.12	55.57 ± 0.92	156.47 ± 7.11	−147.97 ± 8.55	183.95 ± 10.29	2461.70 ± 94.79	8764
Nano	240	158.95 ± 6.74	53.01 ± 0.26	174.19 ± 7.06	−138.84 ± 7.31	106.72 ± 12.20	2171.33 ± 250.85	5067

*normalised to 55.56 % FVC

B. Appendix to Chapter 5

B.1. LVI and CAI

Table B.1.: Number of samples tested for each impact temperature, impact energy and compressive test temperature

	Impact Energy [J]															
	8			15				18			21					
Impact Temperature [°C]	20	50	80	-20	20	50	80	20	50	80	-20	-20	20	50	80	
No. Specimens LVI	6	6	6	7	10	6	10	6	6	6	6	7	10	6	10	
No. Specimens CAI 20 °C	5	5	5	3	5	5	5	5	5	5	3	5	5	5	5	
No. Specimens CAI 80 °C				3	3		3				3	3			3	

Table B.2.: Summary of the resulting delamination area and permanent indentation depth from different impact parameters

Impact Temperature [°C]	Impact Energy [J]	C-Scan Delamination Area [mm^2]	Permanent Indentation Depth [μm]
20	8	196.05 ± 28.97	51.47 ± 4.07
50	8	140.65 ± 5.09	50.34 ± 3.23
80	8	109.42 ± 12.15	59.21 ± 6.68
20	15	475.88 ± 48.72	109.65 ± 10.27
50	15	288.80 ± 21.28	103.99 ± 6.85
80	15	261.02 ± 32.12	130.29 ± 6.38
-20	15	796.70 ± 181.57	119.01 ± 5.58
20	15	325.36 ± 78.95	141.57 ± 1.92
20	18	493.51 ± 52.70	138.29 ± 15.11
50	18	370.75 ± 71.02	162.85 ± 21.99
80	18	332.79 ± 51.79	168.09 ± 13.12
20	21	718.95 ± 50.42	134.28 ± 8.77
50	21	550.38 ± 111.43	151.20 ± 9.09
80	21	428.42 ± 31.70	171.57 ± 4.38
-20	21	1140.98 ± 105.19	131.82 ± 11.51
20	21	751.63 ± 67.70	144.57 ± 4.67
80	21	355.35 ± 19.16	187.42 ± 19.54

Table B.3.: Summary of the residual compressive strengths resulting from different impact parameters

Impact Temperature [°C]	Impact Energy $[J]$	CAI Temperature [°C]	CAI Strength $\sigma_c^{\max}$ $[MPa]$
20	8	20	348.21 ± 19.23
50	8	20	358.09 ± 21.67
80	8	20	365.46 ± 33.75
20	15	20	288.55 ± 16.37
50	15	20	326.84 ± 11.64
80	15	20	342.67 ± 18.19
-20	15	20	253.81 ± 14.35
-20	15	80	226.68 ± 23.00
20	15	80	232.96 ± 23.55
80	15	80	255.95 ± 13.20
50	18	20	276.81 ± 13.43
80	18	20	274.91 ± 7.24
20	21	20	279.11 ± 10.01
50	21	20	291.35 ± 28.05
80	21	20	284.41 ± 10.42
-20	21	20	219.34 ± 17.23
-20	21	80	216.41 ± 11.82
20	21	80	209.01 ± 13.35
80	21	80	229.87 ± 21.05

B.2. LVI and TAI

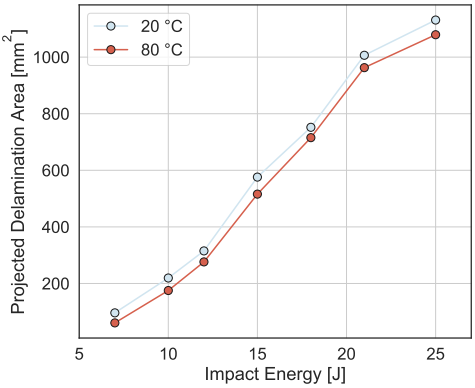

Figure B.1.: Projected delamination area resulting from impacts at different impact energies and temperatures (preliminary testing to determine the impact energy)

Table B.4.: Summary of the results of the impact and tension after impact tests (Impacts were introduced with 25 J impaction energy)

Impact Temperature [°C]	C-Scan Delamination Area $[mm^2]$	Permanent Indentation Depth $[\mu m]$	Tensile Strength σ_t^{max} $[MPa]$	TAI Strength no Fibre Failure σ_t^{max} $[MPa]$	TAI Strength with Fibre Failure σ_t^{max}
-	-	-	1045.66 ± 15.58	-	-
20	1199.54 ± 78.32	152.06 ± 7.44	-	929.56 ± 45.54	–
80	1143.92 ± 60.16	207.28 ± 14.54	-	851.34 ± 91.46	784.12 ± 51.21